IMBALANCE RESPONSE OF A ROTOR SUPPORTED ON INTEGRAL OPEN ENDS SFDs

Oscar De Santiago
Juan Oliveras
Dr. Luis San Andrés

April 1997

TRC-SFD-2-97

Texas A&M University
Mechanical Engineering Department

Imbalance response of a rotor supported on open-ends integral squeeze film dampers

by

Oscar de Santiago
Graduate Research Assistant
Juan Oliveras[*]
Visiting Research Associate
Luis San Andrés
Associate Professor, P.I.
Plank Co. Faculty Fellow

Subject: Squeeze Film Dampers

May 1997

* Professor of Mechanical Engineering at the Universidad Simon Bolívar, Caracas, Venezuela.

TABLE OF CONTENTS

i

NOMENCLATURE

c	ISFD radial clearance, nominal value [230 μm, 0.009 inch]
C_{crit}	Critical damping coefficient for first mode, $2 \cdot (K_{eq} M_{eq})^{1/2}$, [N·s/m (lb.s/in)]
C_V, C_H	*System damping* coefficients for vertical and horizontal motions [N·s/m (lb.s/in)]
C_{dry}	dry or structural system damping coefficient [N.s/m (lb.s/in)]
C_{ISFD}	ISFD direct damping coefficient [N·s/m (lb.s/in)]
C_{seals}	Damping coefficient from lip seals [N·s/m (lb.s/in)].
D	ISFD diameter [96.5 mm (3.8 inch)]
e	Amplitude of rotor motion [μm]
f_{nV}, f_{nH}	First natural frequencies for vertical and horizontal motions [Hz]
f_{nd}	Natural frequency of ISFD [Hz].
g	Gravitiy constant [9.81 m/s² (386.4 in/s²)]
k_s	ISFD elastic lateral support stiffness [35 MN/m (20 klb/in)]
k_B	Bearing support stiffness [N/m (lb/in)]
k_{sD}, k_{sF}	Drive and Free end ISFD stiffness from rap tests [N/m (lb/in)]
K_{Veq}, K_{Heq}	System equivalent stiffness coefficients for vertical and horizontal motions [N/m (lb/in)]
L	ISFD length [23 mm (0.91 inch)]
m	Imbalance mass [gr]
M_{eq}	Equivalent rotor mass for first mode [45.22 kg (99.7 lb)]
M_{Deq}	Damper equivalent mass for its own fundamental vibratory mode (for stiffness determination)
M_c	Coupling mass [0.87 kg (1.93 lb)]
M_d	ISFD mass [2.35 kg kg (5.19lb)]
M_e	Damper mass attached to bearing support [1.33 kg (2.93 lb)]
M_i	Damper mass attached to shaft [1.34 kg (2.96 lb)]
M_r	Rotor mass [41.64 kg (91.8lb)]
P	Pressure [Pa (psi)]
Q	Amplification factor at first critical speed
r	Radius for location of unbalance mass [114.3 mm (4.5 inch)].
u	Imbalance displacement, $m \cdot r / M_{eq}$ [m].
t	Time [sec].
T	Temperature [°C (°F)]
β	Pad arc length [52°]
ε	e/c, Dimensionless ISFD journal center displacement.
θ, z	Circumferential and axial coordinates.
μ	Fluid viscosity [Pa·sec]
ξ	*System* damping ratio, $C/C_{crit} = 1/2Q$.

Subscripts

eq	equivalent for system at first mode
H,V	horizontal and vertical directions
mean	mean and fluctuation values
n	natural value

LIST OF FIGURES

LIST OF TABLES

Imbalance response of a rotor supported on open-ends, integral squeeze film dampers

O. de Santiago, J. Oliveras, L. San Andrés

Texas A&M University

EXECUTIVE SUMMARY

Squeeze film dampers (*SFDs*) are well known to reduce vibration through effective energy dissipation and rotor-structure isolation. Most aircraft gas turbine engines employ at least one squirrel cage supported damper. The major drawback of this design is the excessive cage length (three to four times the bearing length) needed to render a soft centering support. Integral squeeze film dampers (*ISFDs*) are compact mechanical elements with a length no larger than the bearing itself, and comprised of arcuate pads attached to a bearing housing via thin wire-EDM webs. Replacement of squirrel cage *SFDs* by integral dampers on aircraft engines offers distinct advantages such as reduced overall weight and length of the engine structure with less number of parts, accuracy of positioning (centering), and a split segment manufacturing allowing easier assembly, inspection and retrofit than with any other damper configuration.

A test rig for measurement of the imbalance response of a three disk massive rotor supported on integral dampers is described. Experiments to identify the structural stiffness of the *ISFDs* and its range of linearity are fully detailed. Controlled coast-down tests from a top speed of 10 krpm are conducted for various levels of rotor imbalance. The experimental results allow the identification (and analytical validation) of the damping capability of *ISFDs* and aid to determine the applicability of this novel technology to aircraft jet engines.

INTRODUCTION

Squeeze film dampers (*SFDs*) provide viscous damping to rotating structures, allowing for reduction in vibration amplitudes and providing safe isolation from or of other structural components. *SFDs* are customarily used in aircraft jet engines, where rolling element bearings provide little damping to the rotor-bearing system, and in high performance compressors as retrofit elements in series with tilting pad bearings to soften bearing supports, reduce critical speeds, and allow for an extra margin of system stability (Zeidan, et al., 1996). Rotor bearing-*SFD* systems are regarded (in theory) as highly nonlinear, showing jump-phenomena and even chaotic behavior for sufficiently large levels of rotor imbalance. However, few experimental results of practical value have verified the analytical predictions.

Squeeze film dampers derive their behavior from a lubricant being squeezed in the annular space between a non-rotating journal and a bearing housing. The journal, typically mounted on the outer race of rolling element bearings, whirls due to the forces exerted on the rotating shaft. The squeeze film action generates hydrodynamic pressures and damping forces at the film locations where the instantaneous gap is decreasing. In regions where the film thickness locally increases air ingestion is likely to occur, generating a bubbly (air on oil) mixture that resembles a foam.

The performance of squeeze film dampers is not only determined solely by its geometry (length, diameter and radial clearance) and the viscosity of the lubricant used, but by a number of specific design and operating conditions. The level of supply pressure, the feeding and discharge flow mechanisms, the type of end seals, fluid inertia, and dynamic cavitation are but a few of these important factors. *SFDs*, in practice, operate with low levels of external pressurization that generally do not prevent the lubricant in the fluid film lands from liquid vaporization or ingestion of external gaseous media into the film lands. Walton, et al. (1987) found that fluid cavitation onset and extent depends on damper operating parameters such as whirl frequency, journal orbit size and eccentric position, level of supply pressure, and end seal restrictions. Zeidan and Vance (1989a,b,c, 1990) have identified five regimes of cavitation in a *SFD* according to operating conditions. The experiments demonstrated that air ingestion produces gaseous cavitation which under certain conditions determines a nonlinear forced response akin to that of a soft spring. On the other hand, vapor cavitation was shown to lead to a characteristic nonlinear hardening effect. Sun et al. (1992, 1993) discuss the major differences between dynamic *gaseous* and *vapor cavitations* and the likelihood of their existence in a typical practical application.

SQUIRREL CAGE - SFDS VERSUS INTEGRAL SFDS

Squirrel cage supported dampers are the most commonly employed SFD design. Most large aircraft gas turbine engines use at least one, and in many instances, two or three dampers in one engine. A schematic view of this damper is shown in **Figure 1**. The squirrel cage support allows to offset the gravity load and must be soft enough to allow journal motions resulting in an effective damping action. The most distinctive feature of this damper configuration is the relatively large axial space required in comparison to the bearing hydrodynamic length. This is perhaps the major drawback of the design since the squirrel cage often requires three to four times as much space as the damper itself (Zeidan, et al., 1996).

Modern technological advances in metal working have given rise to a novel type of hydrodynamic damper, namely the integral squeeze film damper (ISFD). This ingenious design is made possible by a wire Electrical Discharge Machining (EDM) process. **Figure 2** distinctly notes the features of an ISFD. Integral dampers are compact since they are comprised of arcuate segmented pads attached to the damper housing via thin S-shaped structural webs (cantilevered support ribs) that provide the support stiffness. The thin gap between the sector pads and the outer ring forms the squeeze film lands. The whole assembly may contain any number of pads depending on the load and required stiffness and damping coefficients for the desired application. The pads in the lower half of the damper can be machined with an offset to counter the static deflection due to the rotor weight. Thus, integral dampers require no more axial length than the bearing length and can also be machined as split segments allowing rapid retrofit. Zeidan (1994) discusses successful applications of ISFDs in the petrochemical industry, and Murphy,et al. (1996) also detail high speed experiments of a homopolar compulsator supported on ISFDs.

Replacement of squirrel cage supported SFDs by integral dampers brings the following benefits to an aircraft gas turbine engine:
- reduced overall weight and length of the entire aircraft engine structure, elimination of squirrel cage components thus producing a design with reduced number of parts.
- ability to support axial thrust loads without locking the damper lateral motion.
- accurate positioning (centering) by precise design and construction of the support web stiffness and pad film clearances.
- split configuration which allows easier assembly and inspection than with any other damper designs.

A comprehensive study of the forced performance of integral squeeze film dampers is the main objective of the present investigation.

DESCRIPTION OF TEST RIG AND COMPONENTS

NSF and TRC have funded the construction of an apparatus for measurements of the imbalance responses in a test-rotor supported on squirrel cage SFDs. The objectives of this research are:
(a) to provide reliable imbalance response measurements in a rotor-SFD configuration similar to an aircraft engine,
(b) to develop an empirical model to predict the (measured) forced dynamic performance of SFDs operating with a bubbly air/oil mixture, and
(c) to develop a non-linear SFD-structural model should the test results from (a) evidence deviations from linear behavior.

The first objective, fully completed to this date, comprised the construction of the test apparatus and measurements of the test rotor supported on squirrel-cage SFDs (San Andrés and Lubell, 1997). The rotor-bearing system shows rigid body cylindrical and conical critical speeds below a top operating speed of 10,000 rpm. Over a hundred test measurements have shown the experimental rotor-SFD response to be linear even for large imbalance levels and off-centered damper journal operation. These results have made the third objective irrelevant. Experiments conducted in a controlled orbit SFD rig have shown the profound influence of air ingestion in SFD performance (Díaz and San Andrés, 1997). The empirical model for performance prediction of SFDs with bubbly mixtures is currently under development.

Figure 3 shows a schematic view of the test rig with the rotor supported on conventional SFDs. The rig rests on a base plate bolted to a heavy work table and provided with an elastomeric vibration absorbing pad.

A 10 HP (7.5 kW) DC power supply and DC motor drive the test rotor through a flexible coupling. The motor also bolted to the work table rests on elastomeric pads for added vibration damping. A *drawn cup* roller clutch in the coupling allows the motor to bring the rotor to a top speed of 10,000 rpm, and then be shut off without applying a torque to the freely rotating shaft. This feature of the coupling ensures free coast down tests of the test rig, as the motor friction drag does not affect the rotor deceleration rate.

The rotor consists of a shaft, 26.5 in (673 mm) long and main diameter 3 inches (76.2 mm), and three 1 inch (25.4 mm) thick disks shrunk fitted at evenly spaced intervals of 2.5 inches (63.5 mm). Two of the disks are 11 inches (279.4 mm) in diameter, and the third disk has a diameter of 9 inches (228.6 mm). Each disk has twelve 10-32 threaded holes, evenly spaced 30° apart on radii equal to 4.5 inches (large disks) and 3.75 inches (small disk). At these locations, calibrated imbalance masses are inserted. The rotor, shaft and disks together, weighing 92 pounds (41.7 kg), is supported on two pairs of high precision ball bearings which are themselves mounted inside each damper journal. A thin spacer ring separates the ball bearing pairs, and a nut and collar allows the application of specified preloads in the conventional SFDs.

The bearing span is of 16 inches (406 mm) with the middle disk located half-way between the two supports. The bearing support housings are split elements with a 1.42 inch wide (36 mm) groove at mid-length of their inner bore. This groove is the seat for the damper housings, and upon installation of each damper bearing, it becomes a circumferential chamber that allows lubricant feeding to the damper film lands. The lubricant feed port is located on the side (horizontal plane) of each bearing housing support, and ports at the bottom collect the oil discharge from the ball bearings and squeeze film dampers. Eddy current displacement sensors (proximity probes) are mounted on the inner side of the support housings.

A lubrication system delivers oil to the bearing housings and ball bearings from a 40 gallon (151 liter) reservoir through a variable speed gear pump. The oil temperature in the reservoir is controlled using a 1.5 kW electrical heater. The lubricant discharged from the bearing supports flows through a forced air convection cooler with a thermostat control, and then it is pumped back to the main reservoir. A turbine flow meter monitors the flow rate supplied to the bearing supports and pressure gauges indicate the static supply pressure to each damper. Three pairs of non-contact eddy-current displacement sensors measure the rotor displacement directly at locations next to the damper on the motor drive end, the middle disk, and the damper at the rotor free end (see **Figure 4**). The displacement sensors are mounted in the horizontal and vertical directions, at every plane. Several piezoelectric accelerometers are magnetically attached to the bearing support housings. An optical keyphasor facing the drive motor coupling detects the rotor speed. Temperature measurements are performed with type-K thermocouples at the pump discharge and return oil lines, on the drive motor, and for room temperature. Other thermocouples attached to the side faces of the damper housing provide direct measurements of the operating temperature at the discharge sections of the damper squeeze film lands.

A *Bentley-Nevada* Data Acquisition Interface Unit (DAIU) and the *Adre for Windows*© software installed on a PC Pentium computer record the rotor speed and the vibration signals from six displacement sensors and two accelerometers. The data processing software includes real time slow-roll subtraction, order-tracking and synchronous response filtering. An instrumentation console contains digital displays of the operating rotor speed, flow rate, supply pressures and inlet/exit damper temperatures. The console includes the controls for operation of the lubrication pumps and the oil cooling and heating elements. Three oscilloscopes display the rotor orbits at the monitored locations. A fourth oscilloscope shows the bearing support housing accelerations, and a frequency analyzer depicts the FFT of selected vibration signals.

RESULTS OF RESEARCH WITH SQUIRREL CAGE SUPPORTED SFDS
Most rotor-bearing systems incorporating squeeze film dampers require soft elastic supports (squirrel cage) to render the dampers effective while traversing rigid body critical speeds. Measurements of the imbalance response of the test-rotor supported on squirrel-cage, open-ended *SFD*s have been completed. The test damper depicted in **Figure 5** has dimensions of diameter (*D*) and length (*L*) equal to 3.72 inches (95 mm) and 0.91 inches (23.0 mm), respectively, and radial film clearance (*c*) equal to 0.009 inches (0.229 mm). The journal is attached to the bearing support with four steel bars structure designed for a nominal radial stiffness of 20,000 lb/in (3.5 MN/m). The dampers tested, as per recommendation of the TAMU

Turbomachinery Consortium members, follow specifications similar to those of commercial aircraft engines. An ISO VG-10 lubricant was employed in the experiments.

Over a hundred controlled experiments with imbalance weights exciting the cylindrical and conical modes of vibration for centered and off-centered damper journals have been performed (San Andrés and Lubell, 1997). Tests included damper operation at increasing lubricant temperatures from 70° to 110° F (reduced fluid viscosity) and supply pressures to 30 psig (2 bars). Typical Bode plots of the peak-to-peak amplitudes of motion measured at the rotor middle position are shown in **Figure 6** for increasing imbalance displacements. The synchronous rotor responses show the rotor-*SFD* system to be well damped with amplification factors ranging from 1.6 to 2.1 while traversing cylindrical and conical (rigid body mode) critical speeds. The rotor amplitudes of motion were found to be *proportional* to the imbalances for the first mode of vibration, and the damping coefficients extracted compare reasonably well to predictions based on the **full-film** open-ends *SFD* model. Tight lip (elastomeric) seals contributed greatly to the overall damping of the test rig. Measured dynamic pressures at the squeeze film lands were well above ambient values with no indication of lubricant dynamic cavitation as simple theoretical models dictate. The measurements demonstrate an absence of non-linear behavior of the rotor-*SFD* apparatus for the range of imbalances tested. (San Andrés and Lubell, 1997)

THE TEST INTEGRAL SQUEEZE FILM DAMPERS

KMC, Inc., donated a pair of integral *SFD*s for testing in the rotor-*SFD* rig. The integral damper shown in **Figure 7** consists of four, 55° arcuate squeeze film pads and S-shape thin webs providing a *design* radial stiffness of 20,000 lb/in (3.5 MN/m). The squeeze film lands are machined at a diameter (*D*) of 3.8 inch (96.52 mm) with an axial length (*L*) equal to 0.91 inch (23.0 mm). The nominal film clearance in operation should be close to 0.009 inch (0.230 mm). The top and bottom pads have been machined to –0.007 inches (0.178 mm) and –0.012 inches (0.305 mm), respectively, so that under the static deflection due to the rotor weight they increase (decrease) to the desired nominal clearance. Each squeeze film pad is fed directly from the supply groove through a 1/16 inch (1.6 mm) hole located at the middle plane of each pad. The *ISFD* housing includes threaded holes for the insertion of end seals to increase its damping capability if needed. These end seals, in the form of split circumferential plates and whose clearance is adjusted with thin laminates (shim stacks), provide a controlled discharge restriction.

Figure 8 depicts a view of the test rotor supported on the integral dampers. Note the significant differences in the bearing support and damper axial lengths when compared to the rotor supported on the conventional dampers (as shown in **Figure 3**). In addition, the rotor-*ISFD* rig has less number of parts which simplifies considerably its assembly and alignment.

The analysis and design of *ISFD*s must couple the structural and hydrodynamic models for evaluation of the elastic forces in the structural webs and the fluid film forces developed from each squeeze film pad. The dynamic force response of the *ISFD* depends on the way the ball bearing outer race fits within the damper journal. A very tight fit makes both elements to move as a unit, although it causes excessive interference loads on the rolling bearings if material compatibility for even thermal growth is not accounted for. On the other hand, a looser fit with less contact area may enhance dry friction force, which could cause stick-slip at certain frequencies of operation.

A finite element program has been developed to predict the viscous forces arising from the integral squeeze film damper. The flow model considers an isoviscous, incompressible fluid and laminar, inertialess flows rendering the Reynolds equation for pure squeeze film journal motions. The computational model predicts damper forces given the journal position and velocity, and force coefficients for circular centered motions at a prescribed whirl frequency. Details of the analysis are given in **Appendix A**.

EXPERIMENTS AND PROCEDURES

Controlled experiments have been conducted to identify the fundamental rotor-bearing system parameters, to measure the imbalance response of the test rotor supported on *ISFD*s, and to extract the equivalent damping coefficients of the *ISFD*s. **Figure 9** shows the test rotor dimensions and distances to the locations for the damper supports and displacement sensors.

Identification of Rotor Free-Free Modal Frequencies

The rotor (shaft and press fitted disks) is hung with nylon ropes for identification of its elastic unconstrained modal frequencies. A piezoelectric accelerometer (26.1 gr) is installed through a magnetic base at different locations along the rotor, and subsequently the rotor is excited in the horizontal direction with a calibrated impulse hammer. The measured rotor and coupling weights are equal to 91.8 lbs and 1.933 lbs, respectively. **Table 1** presents a summary of the test natural frequencies along with computed predictions based on a 38 station - transfer matrix model using *XLrotor*[TM] (Murphy, 1995).

Table 1. Measured free-free natural frequencies for test rotor and rotor & coupling. Comparisons with computed predictions.

Frequencies		f_1(Hz)	f_2(Hz)	f_3(Hz)	f_4(Hz)
Rotor	test	620	930	1120	1410
	prediction	619.6	968	1295	--
Rotor and coupling	test	250	920	1110	1410
	prediction	231.3	950	1184	1365

Uncertainty in measurements: +/- 10 Hz

Note the sharp reduction of the first natural frequency once the coupling is installed on the rotor. This is due to the coupling being located at an anti-node for the first elastic mode of vibration. The computed predictions are satisfactory and the elasto-massic model represents well the test rotor and coupling.

Measurement of integral damper radial stiffness.

Precise knowledge of the dampers' lateral stiffness is needed for accurate determination of the rotor-bearing critical speeds. The design value for the damper stiffness (k_s) is equal to 20,000 lb/in (35 MN/m), a magnitude similar to the squirrel cage *SFD* tested earlier. An ad-hoc fixture to support the integral dampers was built to measure the damper structural stiffness. **Figure 10** shows an schematic view of the experimental set up. The fixture consists of a short length steel cylinder resting on (nearly rigid) bushing supports. The shaft is inserted into a damper and held in place on the bushings. Static loads are applied with a crane to the damper outer rim.

Deflections of the shaft (damper inner rim) and damper outer rim are recorded with a displacement sensor (proximity probes) attached to ground so that deformation of the supporting structure could be accounted for and extracted from the overall damper deflection. The applied load is measured with a calibrated strain-gage load cell in series with the cable transmitting the force. The damper stiffness is extracted as the slope from curves of applied load vs. displacement between the outer and inner rims. Measurements are conducted at 45° intervals, for load directed towards a damper pad or in-between pads, with regions of linear and non-linear stiffness identified. A noticeable hardening of the damper denotes progressive solid contact between damper inner lands. **Figure 11** shows the applied load vs. measured damper deflections for the two integral dampers designated as #1 (drive end side) and #2 (free end side of the test rotor). The plots depict results from the tests along the vertical (⇓ gravity, 0° and 180°) and horizontal directions (90° and 270°). The measurements clearly show the regions of linearity for the elastic stiffness from the damper structural webs. Note that the displacements in the negative direction (vertical) are for applied loads directed towards the damper pad with the largest clearance (~ 12 mils), and henceforth explain the larger linear range in this direction.

Table 2 contains a summary of the extracted damper stiffness magnitudes from the load vs. deflection curves. Experimental stiffness values agree well with the design target of k_s=20,000 lb/in. The tests demonstrate that the EDM technique does provide reliable values of structural stiffness. Tests to check for hysteresis of the whole experimental set-up confirm this to be minimal, within ±0.1 mil for loads up to 200 lb.

Table 2. Measured stiffness for integral dampers. Load vs. deflection method.
Design value k_s=20,000 lb/in (35 MN/m)

ISFD Stiffness	SFD #1-Drive End (lb/in)	SFD#2 - Free End (lb/in)
0° (↓)	19,432	18,665
45°	19,484	18,196
90° (←)	20,110	18,707
135°	21,036	19,647
180° (↑)	19,971	19,271
225°	20,059	19,106
270° (→)	19,823	18,418
315°	19,784	18,492
360°	19,816	18,105
Average	19,963	18,813
Vertical	20,085	19,950
Horizontal	20,120	21,660

standard error: 850 lb/in for 95% certainty. Arrows indicate the direction of load relative to inner rim.
Stiffness in Vertical and Horizontal directions account for load deflection data at (0°,180°) and (90°,270°),respectively

The measured stiffness values are verified by independent measurements of the dampers' fundamental natural frequency in the free-free lateral mode and estimation of their equivalent masses from CAD drawings. The weight of each damper (M_d) equals 5.19 lbs, and is composed of two parts, (M_r) the damper outer rim weighing 2.93 lbs and to be firmly attached to a bearing support, and (M_i) the damper inner rim (includes flexural pads and ball bearings) weighing 2.96 lbs and to be coupled to the test rotor. The dampers rest on a layer of soft packing material while being excited by a hard impact in the horizontal direction (see **Figure 12** for a view of the experiment set up). A damper time response to the impact is then recorded by a miniature accelerometer attached to the dampers' outer rim. The measured natural frequency (f_{nd}) and the equivalent masses for the fundamental vibratory mode ($M_{Deq} = M_i M_r / M_d$) provide an estimation of the damper structural stiffness from the fundamental relationship, $k_s = M_{Deq} (2\pi f_{nd})^2$. The measured values of damper "ring" fundamental frequencies and estimated stiffness values are given below as:

SFD #1 -Drive end: f_{nd} = 390 Hz, k_{sD}=19,750 lb/in
SFD#2 - Free end: f_{nd} = 372 Hz, k_{sF}=18,000 lb/in

The damper stiffnesses given above correlate well with the measured horizontal stiffness (at 270°) as well as with the average stiffness values given in **Table 2**.

Identification of fundamental natural frequency of the test rotor-*ISFDs* system.

The test rotor mounted on the ball bearings and integral dampers is secured on the bearing supports. The total rotor weight (M_r) accounting for the coupling masses (M_c) and damper masses attached to the shaft (M_i) is equal to 99.65 lbs (45.20 kg). The rotor and coupling weights are taken by the two dampers. A static balance of forces dictates that the fractions of the rotor weight supported by the drive end (#1) and free end(#2) damper structural webs are equal to 0.57 and 0.43, respectively. These weights when applied to each damper determine a static deflection of approximately 2.66 mils (67.6 μm) and 2.16 mils (55.08 μm) at the drive and free end supports, respectively. Note that these damper deflections open up (increase) the top clearances in the *ISFDs* while closing (reducing) the bottom pad clearances. In the end, it is believed the overall clearance in all pads of the *ISFDs* is very close to the design value of 9.0 mils (229 μm).

The rotor is coupled to the drive motor and an alignment procedure performed using the reverse dial gauge indicator method. Next, the lubrication system is connected to supply the dampers and ball bearings with an ISO VG 10 spindle oil. Lubricant viscosity measurements at increasing oil temperatures are also performed using an electro-viscometer. The measured lubricant viscosity is given below in tabular form.

Table 3. Measured viscosity values of lubricant used in test apparatus

Lubricant type	Specific gravity	Viscosity centipoise	Temperature (°C)[°F]
ISO VG 10 36 API gravity	0.845	15.4	25.0 [77]
		12.9	29.5 [85]
		10.5	35.0 [95]
		8.63	40.5[105]
		7.14	46.1[115]
		6.47	51.6[125]

An exponential relationship was calculated from the measured values of viscosity and temperature. This is given as

$$\mu = \mu_{77}\, e^{-\alpha(T-77)}, \text{ where } \alpha=0.020683/°F$$

RAP measurements of the test-rotor supported on *ISFDs* are conducted to identify the system damped natural frequencies and the fundamental damping ratio. A calibrated impact hammer excites the rotor and an accelerometer magnetically attached to the middle-disk collects the vibration signatures from a number of impacts at zero rotational speed. The fundamental (lowest) test natural frequencies for the cylindrical rigid mode of vibration are $f_{nH}=52$ Hz and $f_{nV}=56$ Hz in the horizontal and vertical directions, respectively. These measured values denote (a) asymmetry in the support stiffness, and (b) equivalent support stiffnesses lower than those measured for the *ISFDs* alone.

Consider that the equivalent mass (M_{eq}) of the rotor-*ISFDs* system equals 99.65 lbs (45.2 kg)[1] for the first mode of vibration (cylindrical bouncing mode of a rigid rotor on soft supports). Then, an estimate for the equivalent stiffness of the rotor-bearing system is determined from the fundamental relationship $K_{eq}=M_{eq}(2\pi f_n)^2$. The estimated system equivalent stiffness (K_{eq}) along with the critical damping (C_{crit}) for the fundamental mode are given below (**Table 4**).

Table 4. Estimated system stiffness and critical damping coefficients for first natural mode of vibration. Equivalent mass M_{eq}=99.65 lb (45.20 kg).

	$K_{eq}=M_{eq}(2\pi f_n)^2$	$C_{crit}=2M_{eq}(2\pi f_n)$	f_n
Horizontal plane	27,530 lb/in (48.18 MN/m)	168.52 lb.s/in (29,492 N.s/m)	52 Hz
Vertical Plane	31,928 lb/in (55.88 MN/m)	181.5 lb.s/in (31,758 N.s/m)	56 Hz

These equivalent system stiffnesses are much lower than the design value of $2 \times k_s$=40,000 lb/in which accounts for the dampers' structural stiffness alone. The test results then evidence that the bearing support structures can not be regarded as rigid. Henceforth, systematic tests to measure their mechanical impedance becomes mandatory. Details on the procedure followed are given later.

Predictions for the natural frequencies using the 38 station - transfer matrix model with *XLRotor*™ are also calculated. These are compared to the measurements in **Table 5**. The bearing support stiffness values used in the computational model are also noted. Note that the favorable correlation between predictions and measurements for the fundamental mode is due to the "tuning" of the support stiffnesses on the computer model. However, the simple procedure implemented to set these values validates the single 1-DOF model for the first mode of vibration, i.e. nearly rigid rotor supported on soft springs.

---

[1] This equivalent mass is the sum of the rotor mass (M_r), coupling mass (M_c), and the portion of the integral dampers' masses (M_s) attached to the rotor.

Table 5. Measured natural frequencies for test rotor supported on integral dampers. Comparisons with computed predictions.

Frequencies	f_{1H}(Hz)	f_{1V}(Hz)	f_{2H}(Hz)	f_{2V}(Hz)	f_e(Hz)
test	52	56	94	96	201
predicted	51.40	55.20	88.5	95	232
mode	cylindrical	cylindrical	conical	conical	elastic

Uncertainty in measurements: +/- 2 Hz.
Support stiffness: k_H=13,675 lb/in, k_V=15,964 lb/in [1/2 values given in Table 4]

The system damping coefficients are extracted from least-square log decrement estimations and transfer function measurements with the aid of a frequency analyzer. Tests are performed at increasing lubricant temperatures from 70° F (21° C) to 90° F (32.2° C) to determine the variation of the system damping coefficient as the oil viscosity decreases. From these measurements, the structural damping and the viscous damping coefficient from the pair of *ISFDs* are identified. **Table 6** lists a summary of the extracted fundamental damping coefficients. **Figures 13** depict graphs of the rotor acceleration vs. time, and the transfer function (acceleration/load) along with the coherence function. The transfer function is the average of 10 impacts with automatic data rejection for hard impacts above 20 lbs.

Table 6. Identified *system* damping coefficients from RAP tests for increasing lubricant temperatures (centered rotor).

Oil temperature (° F)	Viscosity (cp)	Damping Horizontal C_H (lb.s/in)	Damping Vertical C_V (lb.s/in)
100	9.57	9.873	14.57
85	13.0	10.852	15.45
76.5	15.5	12.06	16.02
74.5	16.2	13.62	16.09
73*	16.7	14.60	15.68
73*	16.1	13.51	17.84
		f_{nH}=54 Hz	f_{nV}=58 Hz
DRY (no oil)	0.0	5.42	9.62

*tests repeated on different dates Uncertainty in measurements – 1 lb.s/in

DIGRESSION: Damping from lip seals

The rotor supported on conventional *SFDs* reported by San Andrés and Lubell (1996) contained lip seals on the side of the supports facing the rotor disks. These lip seals fitted too tightly on the rotor and constrained the motion of the shaft to a great extent, thus producing a stiffening effect accompanied by a considerable amount of structural damping. Rap tests conducted on this earlier configuration revealed the following damping coefficients for the "dry" or *oil-free* rotor-SFD at two different temperatures (21°C and 38 °C):

$$C_{Vseals} = 21.7 : 17.8 \text{ lb-s/in } (3.80 : 3.11 \text{ kN-s/m })$$
$$C_{Hseals} = 17.0 : 13.8 \text{ lb-s/in } (2.98 : 2.41 \text{ kN-s/m})$$

in the vertical and horizontal directions, respectively. These values of support damping (with no oil supplied to the *SFDs*) are regarded as too large, i.e. produce damping ratios larger than 10% of critical damping. Note that keeping these lip seals for the current tests with the rotor supported on open-ends integral *SFDs* may have obscured any measurements since these *ISFDs* are predicted to show less viscous damping than a cylindrical (360°) damper of the same dimensions. Consequently, the original lip seals were replaced by flexible tubing seals fitting loosely around the shaft but prevent lubricant leakage from the support housings. These ad-hoc housing seals have proved successful in reducing the damping coefficient as reported by the damping values given in **Table 6**.

Measurements of bearing support transfer functions and identification of equivalent impedance for rotor modeling.

The measured natural frequencies point out the need to characterize well the mechanical impedance of the bearing support housings. The inertance transfer functions (acceleration/load) for the supports have been determined from impact tests and a multiple degree of freedom (MDOF) model has been devised to model the support mechanical impedance. Final results for the vertical support impedance functions have been completed and will be reported shortly in a subsequent report. The MDOF model to identify the horizontal impedance of the bearing supports is yet to be completed.

Displacement transfer functions for the bearing supports have been determined recently. A displacement sensor is held by a bar mechanism and this in turn is connected to a magnetic base which attaches to the heavy table. The displacement sensor facing the supports, in the horizontal and vertical directions, collects the support motion resulting from impacts imparted with a calibrated hammer. **Figures 14** and **15** show the measured support displacements and transfer functions for the drive end and free end supports, respectively. The graphical results include the tests for the horizontal and vertical directions. The coherence functions as average of 10 impact tests indicate a good correlation between the measured displacements and the excitation load at low frequencies where the flexibility (1/stiffness) of the support can be directly extracted from the transfer functions. The identified bearing support stiffnesses are given in **Table 7** along with standard deviations for each measurement. The tests show the bearing supports to be very flexible in the horizontal direction. The time displacements depict significant amplitudes of motion from the supports although the impacts imparted were soft. However, it is also noted that the work table appeared to vibrate while testing. Note that the supports appear to have resonances at around 50 Hz (due to the rotor) and ~100 Hz. The large standard deviations for the measurement of the vertical drive end support stiffness indicate poor confidence for this test.

At each support, the bearings and integral dampers are in series, and consequently, equivalent bearing stiffness coefficients are easily obtained. **Table 7** also includes the equivalent (in series) bearing support coefficients with the integral dampers stiffness (vertical and horizontal) values from **Table 2**. The sum of the free end and drive end equivalent stiffness should represent the system fundamental stiffness as given in **Table 4**. The equivalent supports stiffness are higher than the values given in **Table 4** and which reproduce the fundamental natural frequency of the rotor-*ISFD* system.

Table 7. Test bearing supports stiffness (k_B) from impact tests.

	Vertical (lb/in)	Horizontal (lb/in)
Drive End support stiffness	174,868±102,100	79,556±4,087
Free end support stiffness	160,758±31,660	57,556±4,370
Equivalent drive end stiffness	18,059	16,059
Equivalent free end stiffness	17,747	15,737
Sum of free & drive ends	35,806	31,796
System stiffness from Table 4	31,928	27,530

The measurements then indicate that the support impedances may have to be determined relative to a fixed ground and not relative to the work table. On the other hand, note that the equivalent support stiffness given in **Table 7** render fundamental natural frequencies equal to 55.9 and 59.3 Hz which are only ~3 Hz above the experimental values.

Measurements of the rotor-*ISFDs* imbalance response

Small calibrated masses (m) are inserted to the middle disk at a radius r= 4.5 inch [114.3 mm]. The rotor is then brought rapidly to a top speed of 10,000 rpm, the power shut down, and the coast-down response measured. **Table 8** summarizes the imbalance masses and the average lubricant temperature for each test. The imbalance displacement (u) is calculated as $|mer/M_{eq}|$, with equivalent mass (M_{eq}) equal to 45.2 kg (99.7 lb). All tests are conducted with a pressure supply to the *ISFDs* equal to 10 psig (0.70 bars). Each experimental coast-down is repeated twice to verify the repeatability of the tests. The time to bring the rotor

from its top speed to rest is very long, approximately 500 to 600 seconds, demonstrating that the rotational drag of the rotor-bearing system is small (large time constant).

Table 8. Summary of imbalance tests conditions

Test number	Imbalance mass (*m*) gr	Imbalance distance (*u*) μm (mils)	Oil temperature °C (°F)
121, 122	5	12.62 (0.497)	23 (73 - 74)
119, 120	10	25.25 (0.994)	22 (72 - 73)
123, 124	13	32.83 (1.295)	23 (73 - 75)
125,126,127	17	42.93 (1.690)	23 (73 - 74)

Uncertainty in mass measurements: ±0.1g

The measurements include six rotor displacements (vertical and horizontal planes at the drive end, free end and near the middle disk) and two bearing support housing (horizontal) accelerations. Refer to **Figure 9** for a view on the location of the displacement sensors. **Figures 16** through **18** depict the (vertical and horizontal) synchronous rotor responses at the locations of measurement on the rotor drive end, near the middle disk and the free end, respectively. The synchronous responses are slow-roll compensated at 500 rpm and subtracted from a baseline response (without any imbalance mass) at every speed. **Appendix C** shows a comparison of the measured synchronous responses with and without the baseline compensation. Most measured responses show mainly a synchronous frequency component at all speeds tested. However, for the test with the largest imbalance (17 gr), the measured response shows a subsynchronous vibration (1/2 whirl) at a frequency of 60 Hz while running at 7,100 rpm. This event, depicted on **Figure 19** as a cascade frequency plot for the vertical drive end displacement sensor and accelerometer on the support, lasted only a few seconds. An explanation for this unusual event is yet to be determined. The subsynchronous motion appeared in all the displacement sensors as well as in the accelerometers attached to the bearing housing supports.

The test measurements show excitation of the horizontal and vertical (planes) cylindrical critical speeds at 3,050 (51 Hz) and 3,300 (55 Hz) rpm, respectively[2]. The forward conical critical speeds appear to be excited at speeds of 5,250 (87.5 Hz) and 5,800 (96.7 Hz) rpm for the vertical and horizontal planes, respectively. The synchronous responses are typically larger in the horizontal plane than in the vertical plane, and thus, denote smaller levels of damping in this direction. Note that the critical speeds do not shift (much) as the rotor imbalance increases. The excitation of the conical mode of vibration is puzzling since the imbalance masses are located at the middle disk (very close to the rotor mass center).

The rotor response through the cylindrical mode (critical speed) is analyzed. **Table 9** gives a summary of the measured peak-peak amplitudes of synchronous motion at the locations of measurement while passing through the cylindrical critical speed. **Figure 20** depicts the results of **Table 9** and demonstrates that the pk-pk maximum amplitudes are nearly proportional to the imbalance displacement (*u*). Note also from Table 9 that the average results from the three measurements are very similar to the amplitudes near the middle disk. The measurements then show the integral dampers to operate as linear mechanical elements.

---

[2] It is apparent from the measurements that the test rig base plate also vibrates. This is inferred from the very similar responses recorded by the three displacement sensors (V & H) at the first critical speeds. Recall that the drive and free ends sensors measure vibration relative to the support housing, while the displacement sensor at mid span measures relative to the base plate

Table 9. Values of maximum **pk-pk** imbalance response at the first critical speed for all tests

Imbalance u	Vertical				Horizontal			
	drive end	middle disk	free end	Average	drive end	middle disk	free end	Average
(μm)	(μm)				(μm)			
12.62	104	105	108	106	133	137	117	129
25.25	189	188	194	190	263	273	236	257
32.83	230	221	239	230	308	321	283	304
42.93	280	261	301	281	363	380	333	360

Critical speeds: Vertical: 3300 (55 Hz) rpm.   Horizontal: 3050 rpm (51 Hz)

Estimation of *ISFD* damping coefficients and comparison to predictions

The system amplification factor (Q) at the first critical speed is easily determined by the ratio of the rotor amplitude of motion to the unbalance displacement (u). From this result, values of the system damping ratio ($\xi=1/2Q$) are also extracted. Finally, system damping coefficients are also determined by multiplying ξ times the critical damping coefficients in each direction, vertical and horizontal. **Table 10** provides a summary of the Q, ξ, and system damping coefficients identified from the average rotor amplitudes of motion. The results also include the average peak amplitude of motion divided by a nominal *SFD* radial clearance ($c=0.229$ mm [9 mils]) to highlight the magnitude of the journal displacements within the clearance of the integral dampers.

Table 10. Identified values of system damping ratio and damping coefficients from measurements at cylindrical mode critical speeds.

imbalance u (μm)	Vertical direction, C_{critV}=182 lb-s/in					
	Average 0-pk amplitude (μm)	Dimensionless displacement e/c	Amplification factor Q	Damping ratio ξ	fundamental system damping coefficient (C_V)	
					N-s/m	lb-s/in
12.62	53	0.231	4.20	0.119	3,790	21.66
25.25	95	0.415	3.76	0.133	4,233	24.20
32.83	115	0.502	3.50	0.143	4,550	26.00
42.93	140.5	0.614	3.27	0.153	4,874	27.85
				Average =	4,362	24.92

imbalance u (μm)	Horizontal, C_{critH}=169 lb-s/in					
	average 0-pk amplitude (μm)	Dimensionless displacement e/c	Amplification factor Q	Damping ratio ξ	fundamental system damping coefficient (C_H)	
					N-s/m	lb-s/in
12.62	64.5	0.282	5.11	0.098	2,893	16.53
25.25	128.5	0.561	5.09	0.098	2,906	16.60
32.83	152.0	0.664	4.63	0.108	3,194	18.25
42.93	180.0	0.786	4.19	0.119	3,519	20.11
				Average =	3,128	17.88

The overall system damping coefficients given in **Tables 10.** as extracted from the imbalance response measurements at the first critical speed, increase with the magnitude of the imbalance, i.e. these coefficients show a dependency on the rotor amplitude of motion. The system damping coefficients obtained from RAP tests at zero rotational speed (see results presented in **Table 6**) are somewhat smaller than the

11

values from the imbalance response. Note that the coefficients extracted from soft impact excitation represent effectively those due to very small amplitude rotor motions about the system equilibrium configuration. i.e. ($e \sim 0$). The following Table summarizes then the extracted system damping coefficients from the imbalance response measurements.

Table 11. Summary of identified *system* damping coefficients (horizontal and vertical) for operation at ~23 °C (73 °F)

HORIZONTAL		VERTICAL	
dim-displacement e_H/c	damping coefficient (C_H) lb-s/in	dim-displacement e_V/c	damping co-efficient (C_V) lb-s/in
0 (RAP)	13.51	0 (RAP)	17.84
0.282	16.53	0.231	21.66
0.561	16.60	0.415	24.20
0.664	18.25	0.502	26.00
0.786	20.11	0.614	27.85

The system damping coefficients include the viscous effect of the integral dampers and the structural (inherent) damping of the rotor-bearing system. Recall that for the operating temperature of 23 °C (73 °F) and for soft impact excitations at zero rotor speed, the *dry* (no oil) system damping coefficients are equal to 5.42 and 9.62 lb-s/in for the horizontal and vertical directions, respectively (see Table 6). Thus, subtraction of the *dry* damping coefficients from the values given in the Table above allows the identification of the viscous damping coefficient due solely to the integral squeeze film dampers.[3]

Predictions for the *ISFD* damping coefficients as a function of the operating fluid viscosity, whirl frequency, and amplitude of journal circular motion about an equilibrium configuration are also obtained using the FEM program described in **Appendix A**. The computed damping coefficients for the four-pad integral damper have a mean value and a periodic (fluctuation) component at 4-times the precession journal frequency. The calculated results, shown in **Table 12**, are obtained for an operating clearance of 229 μm (9 mils) and without fluid film cavitation since the typical flow rates measured (0.1 lt/s, 1.60 gpm) did not allow for the formation of suction regions on the squeeze film lands.

Table 12. Predicted *ISFD* direct damping coefficients at an operating temperature of 23 °C (73°F). Fluid viscosity μ=0.017 Pa-s, L=23 mm, c=229 μm, D=96.3 mm, β=52° pad arc length.
Damping coefficient $C_{ISFD} = C_{mean} + C_{fluctuation} \cos(4\omega t)$

	Predicted direct damping C_{ISFD} (lb-s/in)	
e/c	mean	fluctuation
0.044	5.630	0
0.110	5.715	0.055
0.218	6.085	0.375
0.327	6.685	0.685
0.437	7.745	1.345
0.546	9.310	2.690
0.655	12.395	4.745

Note that the simplified formulae, valid for (e~0), $C_{ISFD} = (\beta/90)\pi\mu(D/2)(L/c)^3 = 4.96$ lb-s/in predicts with some accuracy the calculated damping coefficient from the FEM program.

---

[3] Of course this assumes the rotor-bearing system to be linear. This argument is supported strongly by the measured responses

The dry damping coefficients is subtracted from the system damping coefficients and divided by two to determine the actual contribution from the integral dampers (*ISFDs*). The test (or identified) damping coefficients are given in **Table 13** below. In this procedure it is assumed both dampers contribute with identical damping coefficients to the overall *system* damping, and furthermore, that the *dry* or inherent structural damping does not vary with the amplitude of journal displacement.

Table 13. Extracted *ISFD* direct damping coefficients at an operating temperature of 23 °C (73 °F).

$$C_{ISFD}=(C-C_{dry})/2$$

HORIZONTAL		VERTICAL	
dim-displacement $(e/c)_H$	*ISFD* damping coefficient (C_{ISFD-H}) lb-s/in	dim-displacement $(e/c)_V$	*ISFD* damping coefficient (C_{ISFD-V}) lb-s/in
0 (RAP)	4.04	0 (RAP)	4.11
0.282	5.55	0.231	6.02
0.561	5.59	0.415	7.29
0.664	6.41	0.502	8.19
0.786	7.34	0.614	9.11

The estimated *ISFD* damping coefficients from the imbalance measurements (**Table 13**) and the predicted (mean value) damping coefficients (**Table 12**) are plotted in **Figure 21**. The measurements indicate *ISFD* damping coefficients smaller in the horizontal direction which corresponds to the plane of larger vibrations at the first critical speed. The predicted results show a favorable correlation for the damping coefficient in the vertical direction. However, the predicted values in the horizontal direction are much larger than the measurements since the horizontal journal displacements are also large in this direction. Note that the experimental damping coefficient show an approximate linear behavior with the journal amplitude as opposed to the predictions which are basically non-linear. This type of behavior is also found in the earlier tests with the conventional *SFDs* (San Andrés and Lubell, 1997). In general, the integral dampers offer approximately 1/5 of the damping coefficients that a similar cylindrical damper of the same physical dimensions showed in earlier tests. This fact, however, was well known at the design stages of the integral dampers.

The bearing support horizontal accelerations are also measured in the imbalance response tests. **Figures 23** show the (filtered) synchronous component of the bearing housing supports accelerations for increasing levels of the mass imbalances. The overall acceleration is also included for the largest test imbalance. The support accelerations peak first at the first critical speed, and then steadily raise as the rotor speed increases. At the first critical speed absolute levels of support motion are extracted from the synchronous acceleration component using the well known relationship, displacement ~ acceleration x frequency². The support displacement values are given below in **Table 14**, and include displacements extracted from measurements of vertical support acceleration obtained for a single test with a10 gr mass imbalance.

13

Table 14. Peak support (horizontal) synchronous displacements at first critical speed (52Hz) as extracted from measurements of support acceleration

Imbalance mass m (gr)	Imbalance displacement u (μm)	Drive end support displacement (μm)	Free end support displacement (μm)
5	12.62	28.2	20.2
10	25.25	49.5	34.9
10 (v)*	25.25	15.8 (v)	28.1 (v)
13	32.83	56.5	45.4
17	42.93	67.1	28.1

* Vertical acceleration measurements are conducted only for a mass imbalance equal to 10 gr.

The estimated support displacements given above, as compared to the amplitudes of horizontal rotor motion given in **Table 10**, indicate the bearing supports move a significant amount and can not be disregarded in the rotor-bearing model. Thus, an accurate characterization of the bearing support impedances is of great importance to understand the behavior of the test rotor-*ISFDs* system.

Computed predictions for the linear imbalance response of the rotor-bearing system are performed using the *XLrotor*[TM] model. **Figure 23** shows the calculated responses (vertical and horizontal) at the middle disk for three levels of mass imbalance. The predictions attempt to replicate the imbalance measurements depicted in **Figure 17**. The model assumes that each bearing support contributes ½ the value of the estimated fundamental system damping given in **Table 10**. Note that the imbalance masses are inserted at the middle disk outer radius (very near to the rotor center of mass), and consequently should not excite any other mode but the fundamental cylindrical mode. The predictions match very well the rotor response at the first critical speeds (52 and 56 Hz in the horizontal and vertical directions, respectively). However, the calculated responses fail to reproduce the measured large amplitudes of motion in the range of 5.5 to 6.5 krpm. At this time it is most convenient for the reader to review the measured transfer functions (displacement/load) for the supports as given in **Figures 14** and **15**. Note that the impact load excites a support natural mode in the range of 90 to 100 Hz. At first this zone of high amplitude motions could be mistaken with the excitation of the rotor-bearing conical mode. However, now it is suspected that this resonance corresponds to a natural frequency of the bearing supports, and thus, it explains the unusual measured imbalance responses. More detailed descriptions of the bearing support impedances are thus essential to predict responses similar to the measured ones.

CONCLUSIONS

Measurements of the imbalance response of a massive three-disk rotor-bearing system supported on open ends, integral squeeze film dampers (*ISFDs*) are presented. The dampers are compact mechanical devices with integral radial stiffness procured by wire EDM thin webs. The *ISFDs* have length and diameter equal to 3.8 inches (96.52 mm) and 0.91 inches (23.0 mm), with a nominal clearance equal to 9 mils (229 μm). The tests are performed with an ISO VG 10 lubricant at room temperature (73 °F). Electronic instrumentation along with a data acquisition system record shaft speed, oil temperatures and flow rate, vibration displacements at three shaft locations, and the support housing accelerations.

Experiments are performed to identify the fundamental parameters of the rotor-bearing system. Rotor free-free mode natural frequencies are measured and validated by computed predictions. The structural stiffness coefficients of each *ISFD* are also identified for different load orientations. The test stiffnesses verify closely the design target value of 20 klb/in. The load vs. damper deflection experiments show a linear range of approximately 9 mils. Large enough loads cause solid contact of the damper pads with the bearing shell and raise the damper stiffness dramatically. Gap regions in the damper pads for linear elastic behavior are clearly defined by the tests.

Measurements of the rotor undamped natural frequencies on its bearing supports show cylindrical modes at 52 and 55 Hz, a conical mode at ~90 Hz, and a first bending mode at 201 Hz. The first two natural frequencies are within the rotor speed operating range (< 10 krpm). Analytical verification of the experimental rotor-*ISFDs* natural frequencies require of equivalent bearing stiffness values much lower

than those of the *ISFD*s alone. Measurements of the bearing supports flexibility with impact load excitations demonstrate the horizontal and vertical support stiffnesses to be approximately 3.2 and 9 times larger than those of the dampers. Therefore, the equivalent bearing stiffnesses, damper and bearing support in series, are just 70% to 80% of the actual integral dampers' structural stiffness.

The *system damping* coefficients, extracted from impact load (rap) excitations at zero speed, vary with the lubricant temperature and include the contribution of the structural damping from the bearing supports and lip seal. Measurements of the synchronous rotor response with increasing imbalance masses inserted at the middle disk are performed in coast-down tests from 10 krpm. The tests show the *ISFD*s to damp well the rotor response for the cylindrical modes of vibration. The peak vibration amplitudes at the first critical speed are proportional (*linear*) to the magnitude of the imbalances. Large rotor motions to 80% of the nominal *ISFD* clearance are measured, and without shifts in the first critical speed denoting an absence of damper stiffness hardening. Rotordynamic responses with subsynchronous whirl components are nearly absent in all tests, except for a brief appearance in the experiment with the largest imbalance mass. Measurements of the acceleration in the bearing supports indicate them to have an appreciable amplitude of motion. The imbalance responses show an unexpected resonance at approximately 6,000 rpm. This appears to be related to a softening of the bearing supports. Computed imbalance responses predict well the passage through the first critical speed but fail to reproduce a resonance at about 6 krpm. A reliable impedance model for the bearing supports is currently under development.

The test *system damping* coefficients increase slightly with the amplitude of rotor motion through the first critical speed. From these, the viscous damping coefficients from the *ISFD*s are extracted and agree reasonably well with predictions from a **full-film** open ends *ISFD* finite element model. In general, the integral dampers offer approximately 1/5 of the damping that a similar cylindrical damper of the same physical dimensions demonstrated in earlier tests. This fact however was well known at the design stages of the *ISFD*s.

Measurements of the test rotor-*SFD* responses to coupled mass imbalances and for *ISFD*s with end seals will be performed next. The major objective is to determine the effect of controlled end gap seals on the integral damper viscous force coefficients and their influence on the imbalance response of the test rotor. An accurate characterization of the support impedances is also a major task to be pursued in the next few months.

REFERENCES

Diaz, S., and L. San Andrés, 1997, "Measurements of Pressure in a Squeeze Film Damper with an Air/Oil Bubbly Mixture," accepted for presentation at the *World Tribology Conference*, London, UK, September.

Mohan, S., and Hahn, E. J., 1974, "Design for Squeeze Film Damper Supports for Rigid Rotors," *ASME Journal of Engineering for Industry*, Vol. 96, pp. 976-982.

Murphy, B. T., 1995, "*XLROTOR*", Rotating Machinery Analysis, Inc., Austin, TX.

Murphy, B.T., S.M. Manifold, and J.R. Kitzmiller, 1996, "Compulsator Rotordynamics and Suspension Design," Internal Progress Report, Center for Electromechanics, University of Texas.

Li, X.H., and Taylor, D., 1987, "Nonsynchronous Motion of Squeeze Film Damper System," *ASME Journal of Tribology*, Vol. 109, pp. 169-176.

San Andrés, L., and J.M. Vance, 1988, "Effect of Fluid Inertia on the Performance of Squeeze Film Damper Supported Rotors," *ASME Journal of Engineering for Gas Turbines and Power*, Vol. 110, pp. 51-57.

San Andrés, L., and D. Lubell, 1996, "Unbalance Response of a Test Rotor Supported on Squeeze Film Dampers," Turbomachinery Research Consortium Progress Report #TRC-96-SFD-1, May.

San Andrés, L., and D. Lubell, 1997, "Imbalance Response of a Test Rotor Supported on Squeeze Film Dampers," to be presented at the ASME Turbo Expo'97, Orlando, FLA, accepted for publication at *ASME Journal of Gas Turbines and Power*.

Sun, D.C., and D. Brewe, 1992, "Two Reference Time Scales for Studing the Dynamic Cavitation of Liquid Films," *ASME Journal of Tribology*, Vol. 114, pp. 612-615.

Sun, D.C., Brewe, D., and P. Abel, 1993, "Simultaneous Pressure Measurements and High Speed Photography Study of Cavitation in Dynamic Loaded Journal Bearings," *ASME Journal of Tribology*, Vol. 115, pp. 88-95.

Vance, J., 1988, *Rotordynamics of Turbomachinery*, John Wiley and Sons Pubs, New York.

Walton, J., F. Walowit, J. Zorzi, E. Schrand, 1987, "Experimental Observation of Cavitating Squeeze Film Dampers," *ASME Journal of Tribology*, Vol. 109, pp. 290-295.

Zeidan, F.Y., and J.M. Vance, 1989a, "Cavitation Leading to a Two Phase Fluid in a Squeeze Film Damper," *STLE Tribology Transactions*, Vol. 32, pp. 100-104.

Zeidan, F.Y., and J.M. Vance, 1989b, "Experimental Investigation of Cavitation Effects on the Squeeze Film Force Coefficients," *1989 ASME Design Technology Conference, Rotating Machinery Dynamics*, Montreal, Canada.

Zeidan, F.Y., and J.M. Vance, 1989c, "Cavitation Regimes in Squeeze Film Dampers and Their Effect on the Pressure Distribution," *STLE Annual Meeting*, Atlanta, Georgia, STLE Pre-print No 89-AM-4B-1.

Zeidan, F.Y., and J.M. Vance, 1990, "A Density Correlation for a Two-Phase Lubricant and Its Effect on Pressure Distribution," *STLE Tribology Transactions*, Vol. 33, pp. 641-647.

Zeidan, F.Y., and J.M. Vance, 1990, "A Density Correlation for a Two-Phase Lubricant and Its Effect on Pressure Distribution," *STLE Tribology Transactions*, Vol. 33, pp. 641-647.

Zeidan, F. Y., 1994, "Applications of Squeeze Film Dampers", *Turbomachinery International*, Sept/Oct., pp. 50-53.

Zeidan, F., L. San Andrés, and J. Vance, 1996, "Design and Application of Squeeze Film Dampers in Rotating Machinery," Proceedings of the 25th Turbomachinery Symposium, Turbomachinery Laboratory, Texas A&M University, September, pp. 169-188.
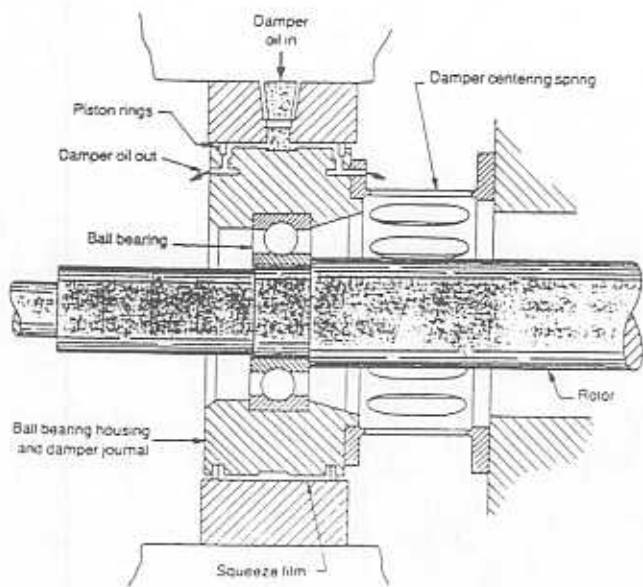
Figure 1. Schematic view of a squeeze film damper and squirrel cage spring.
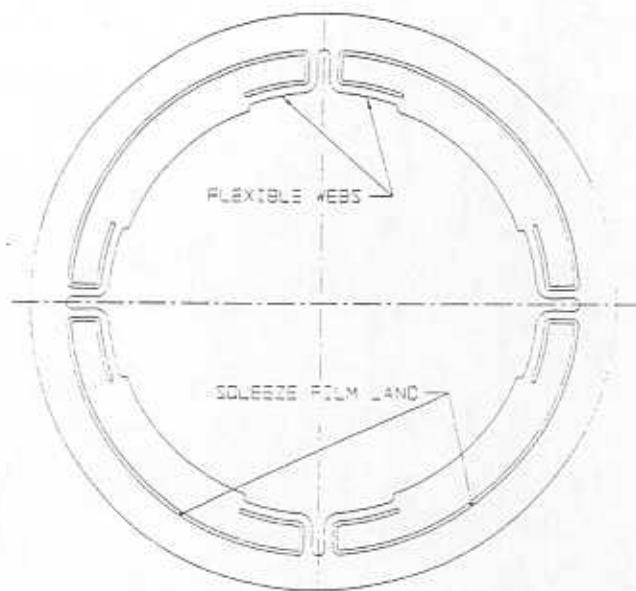
Figure 2. Schematic view of an integral centering spring SFD.

Max. Running Speed = 9,500 rpm

Rotor Weight = 92 lbs
Max. Diameter = 11 in
Shaft Diameter = 3 in
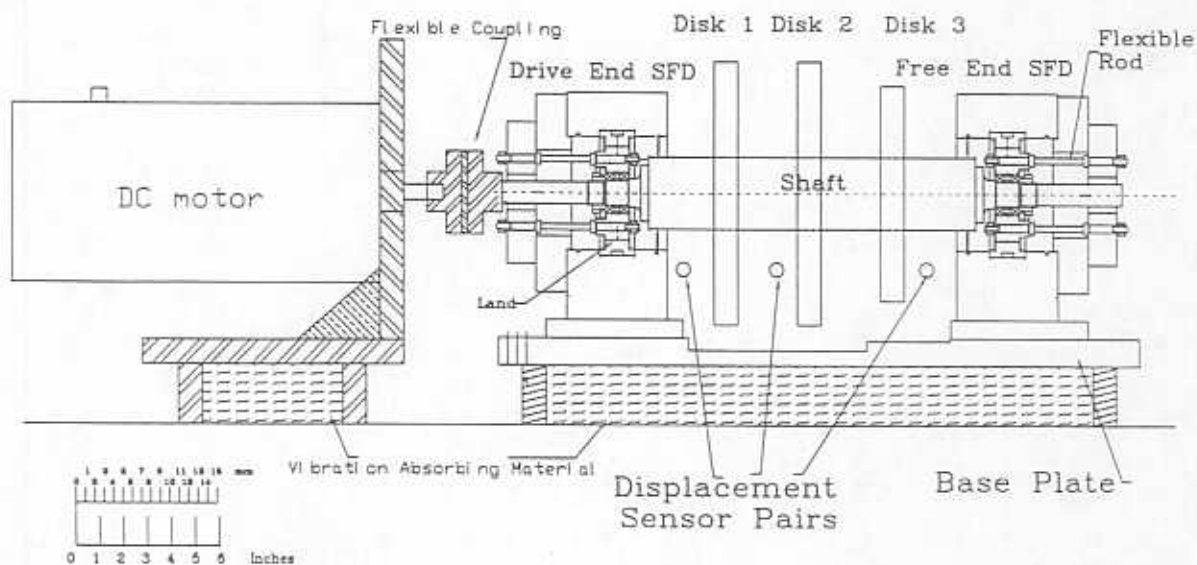
Figure 3. View of test rig: rotor-bearing supported on SFDs.
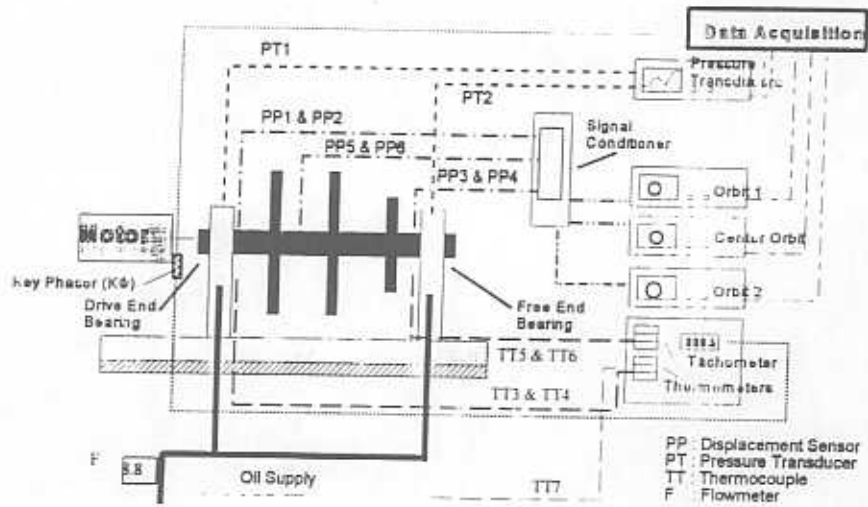
Figure 4. Instrumentation of rotor-SFD test apparatus
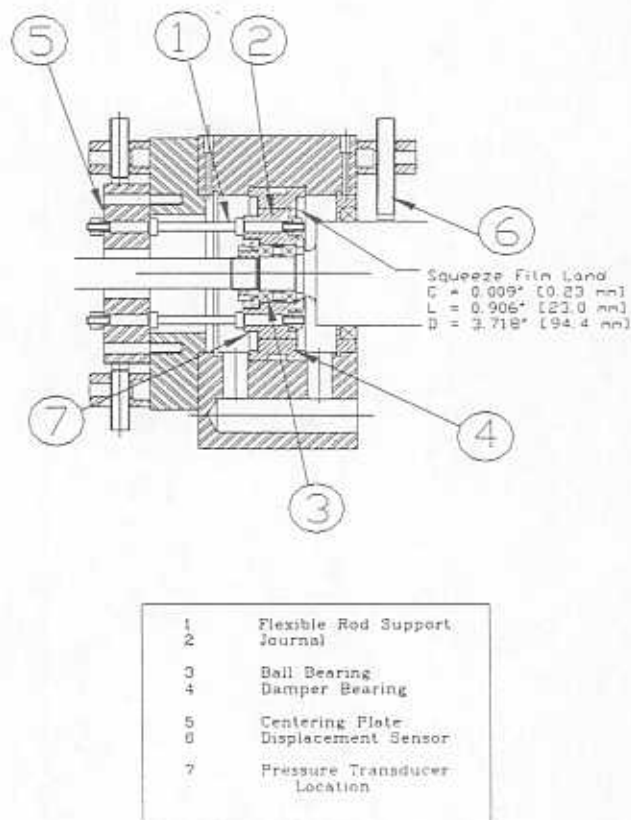
Figure 5. Test (conventional) squeeze film damper with flexible support.
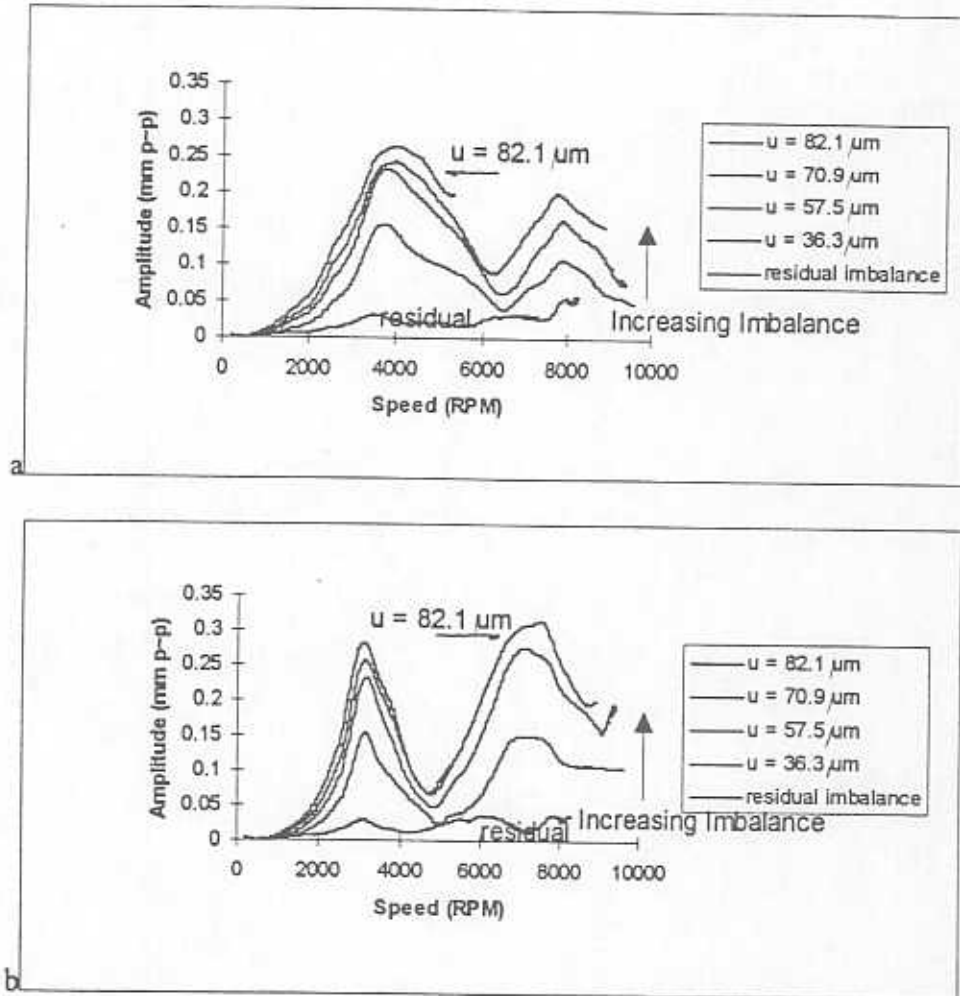
Figure 6. Measured imbalance responses at middle disk. Rotor supported squirrel cage - SFDs. (a) vertical, (b) horizontal.

SECTION A-A

(SOME ITEMS SHOWN OUT OF TRUE POSITION)

Journal
Ball Bearings
horizontal
Integral Elastic Support
Pressure Transducer
Damper Housing
Squeeze Film Land

FRONT VIEW WITH SEAL AND BEARING CAP REMOVED

vertical
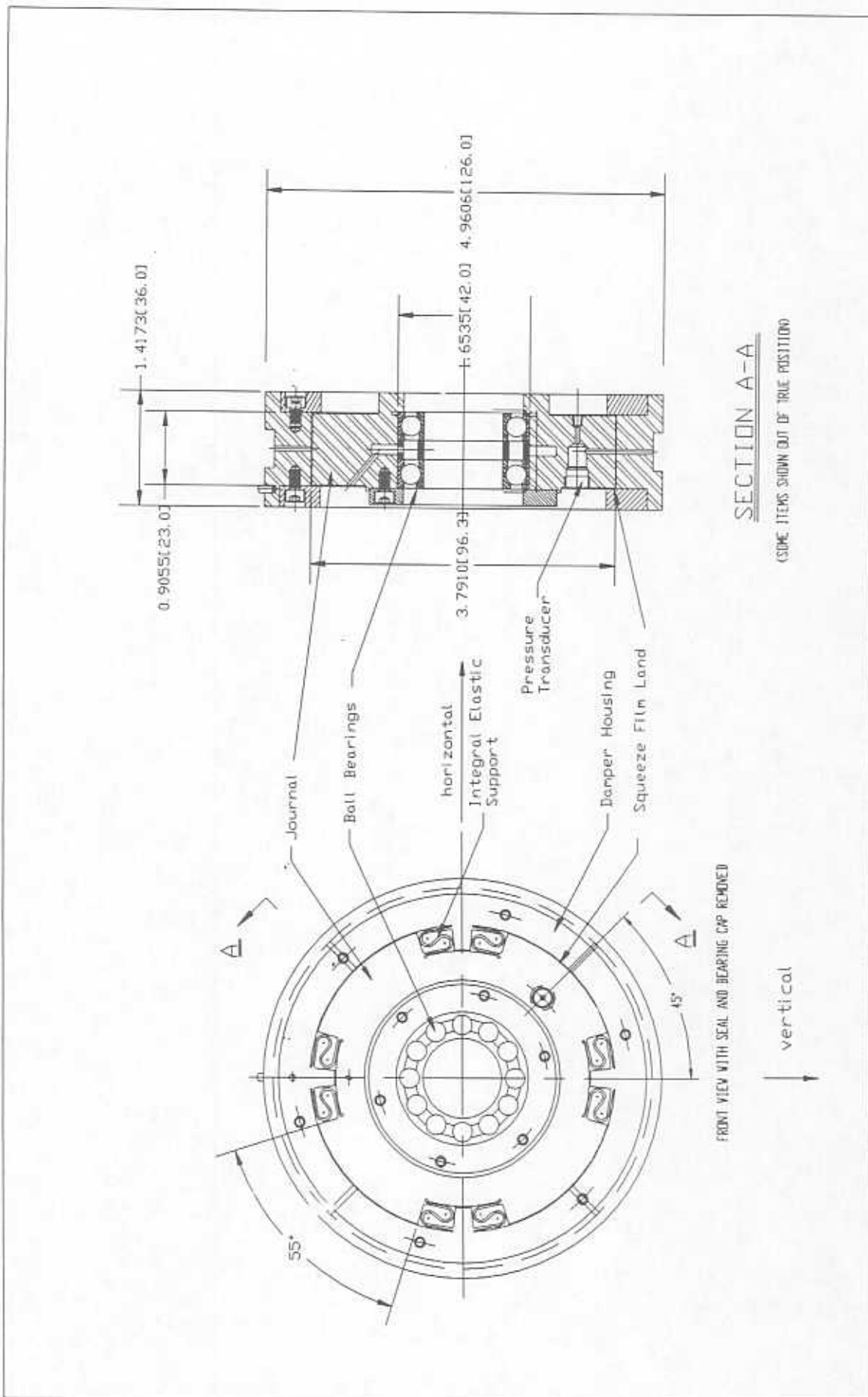
Figure 7. Integral SFD tested on rotor-SFD test rig.

Max. Running Speed =
10,00 rpm

Rotor Weight = 92 lbs
Max. Diameter = 11 in
Shaft Diameter = 3 in

Flexible Coupling

Drive End   Disk 1 Disk 2 Disk 3   Free End

Seal

Shaft

Land

DC motor

Vibration Absorbing Material

Base Plate
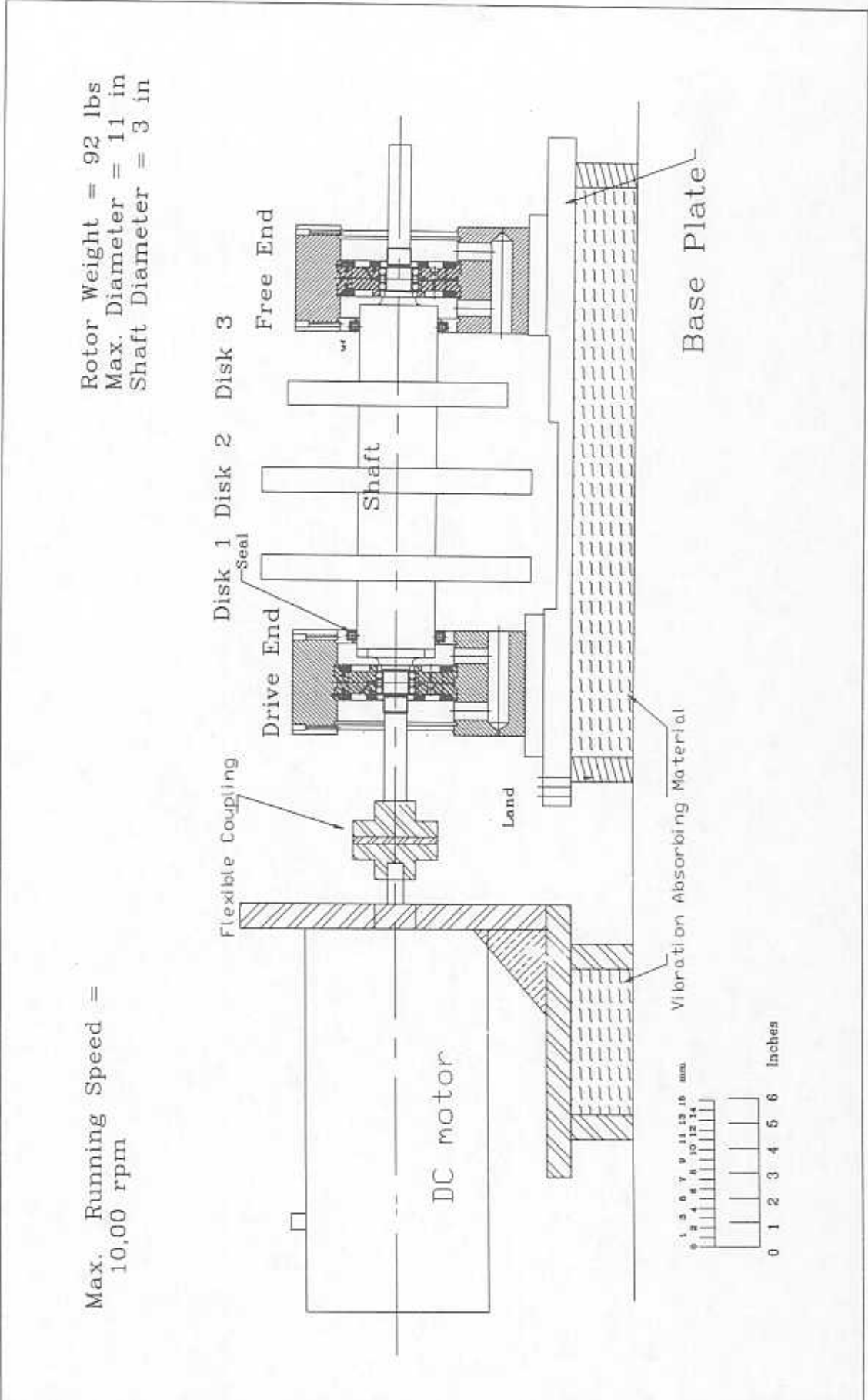
Figure 8. View of test rig: rotor bearing supported on integral SFDs
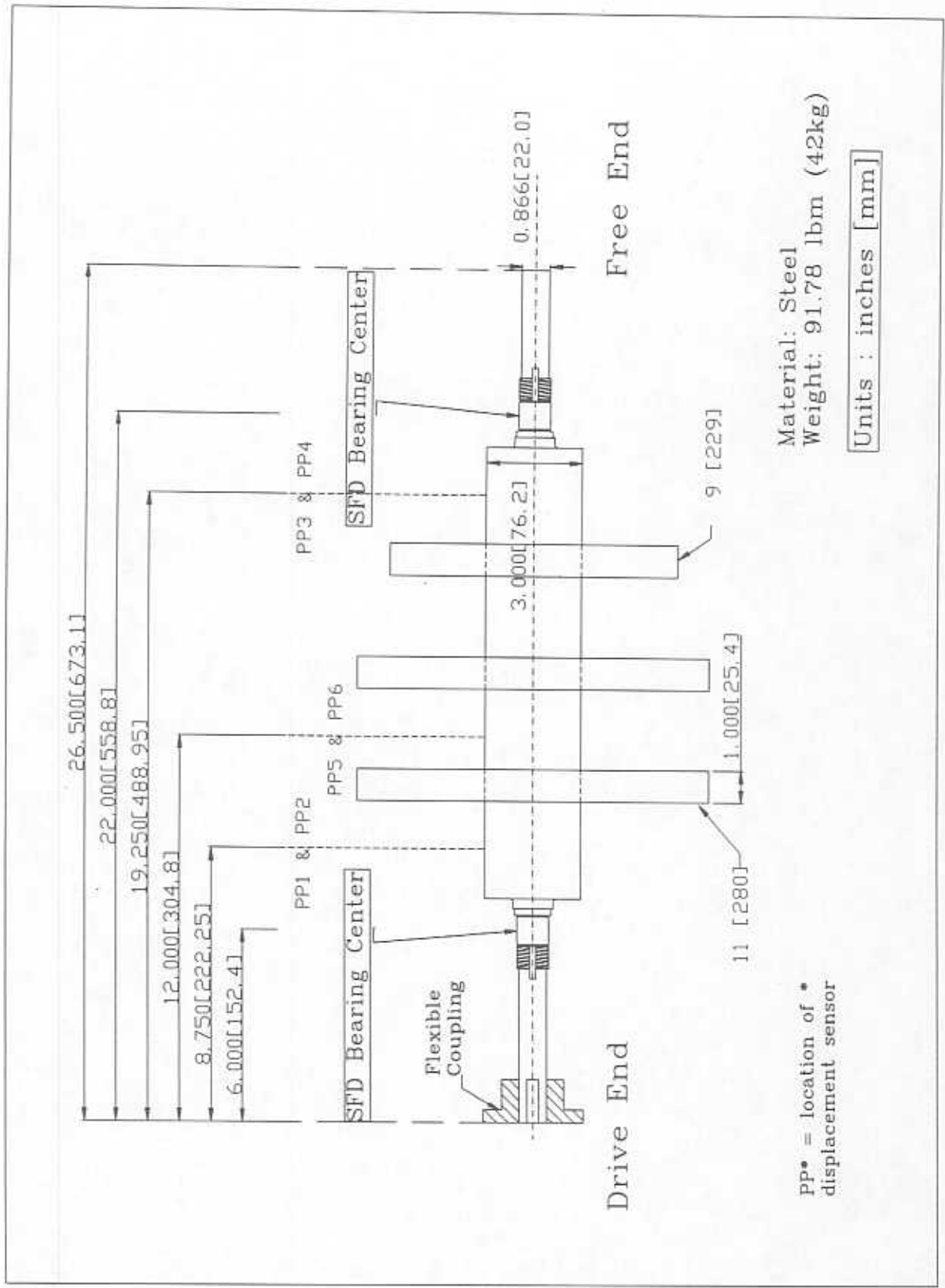
Figure 9. Test rotor dimensions and distances to bearing supports and displacement sensors
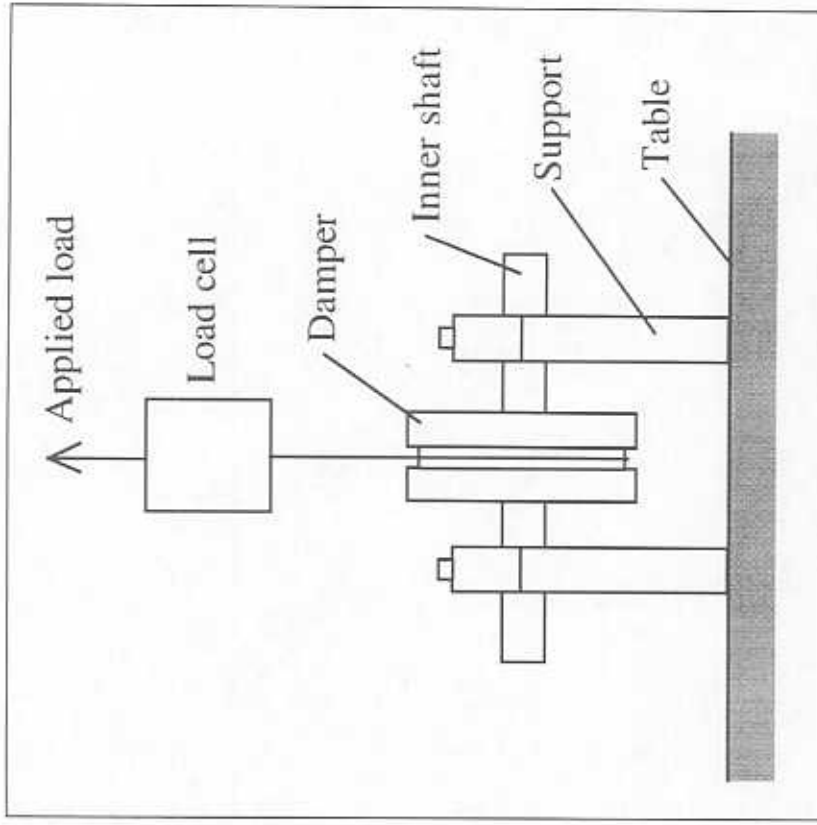
Figure 10. Experimental set-up for measurement of *ISFD* stiffness.
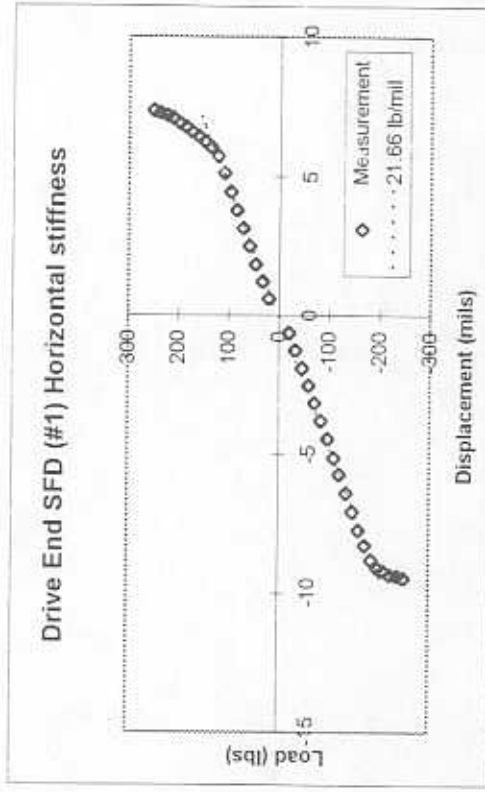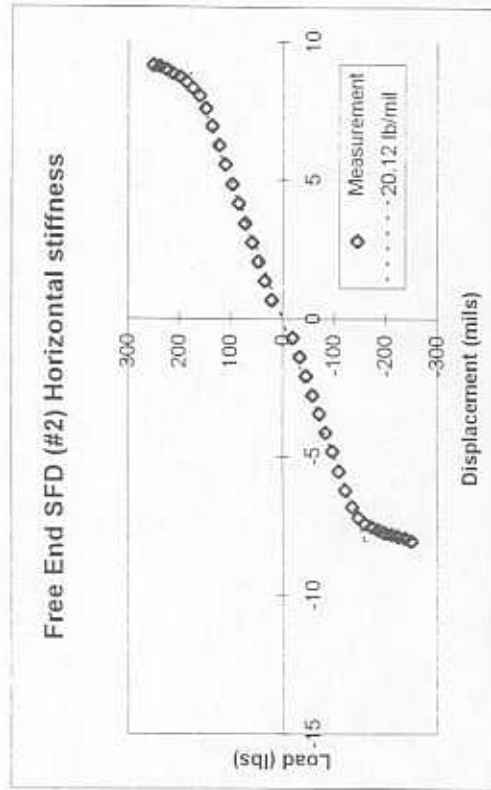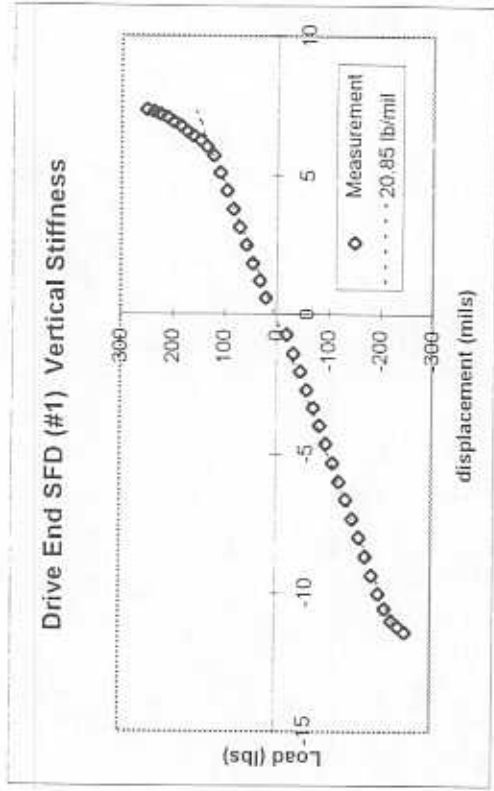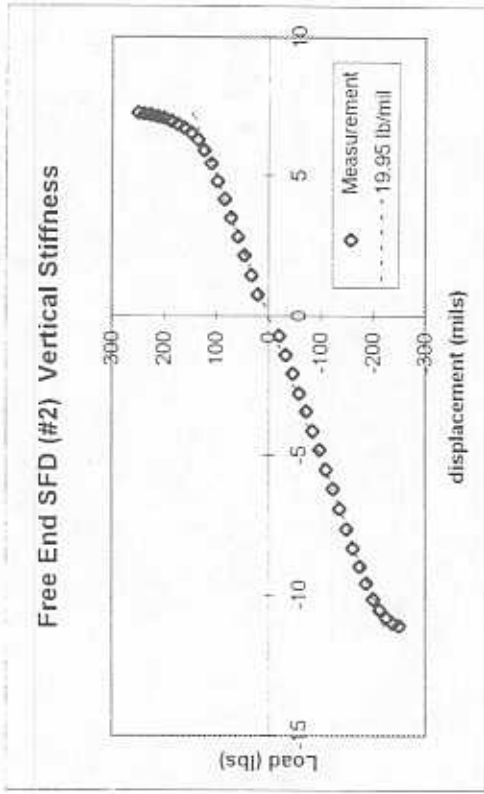
Figure 11. Vertical and horizontal structural stiffness coefficients of integral dampers for drive-end and free-end supports.
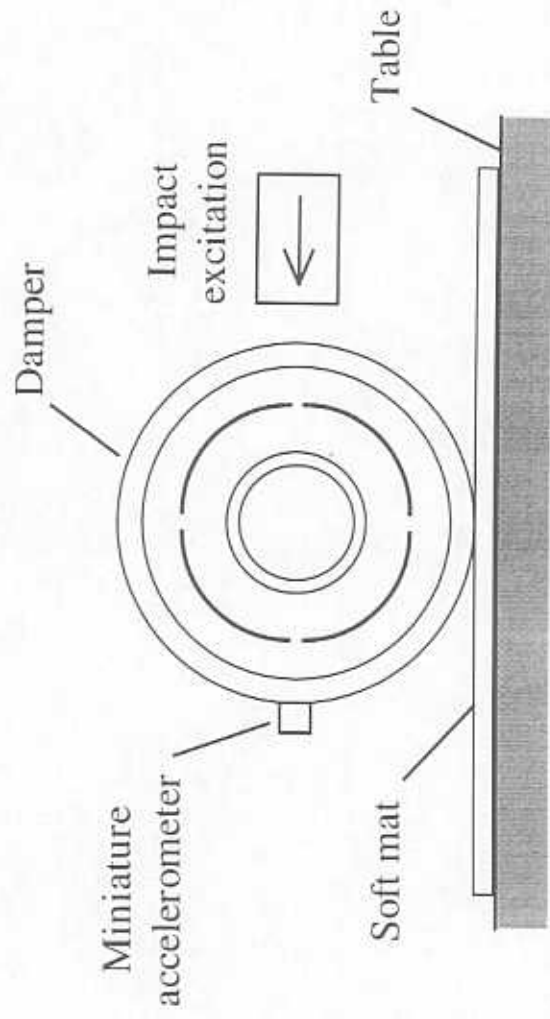
Figure 12. Experimental set-up for measurement of the fundamental free-free ringing natural frequency on the *ISFDs*.

a) Transfer function Acc/Force

b) Time trace
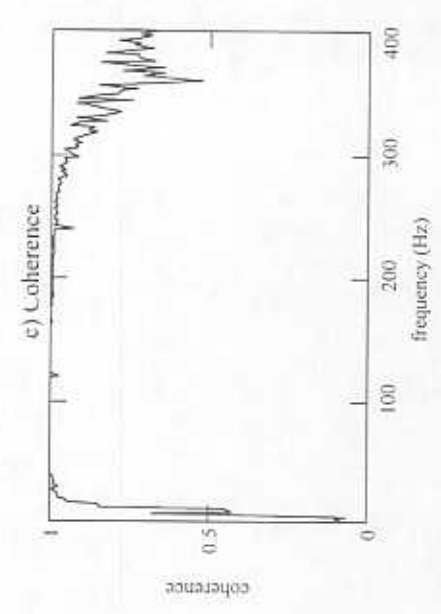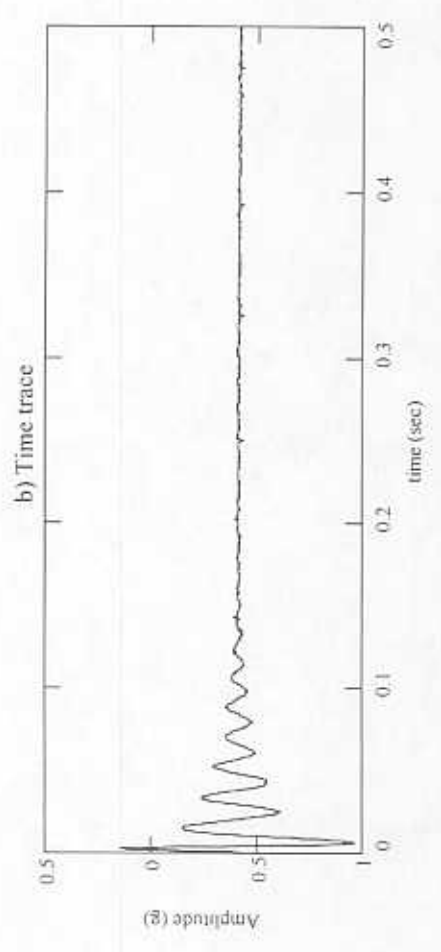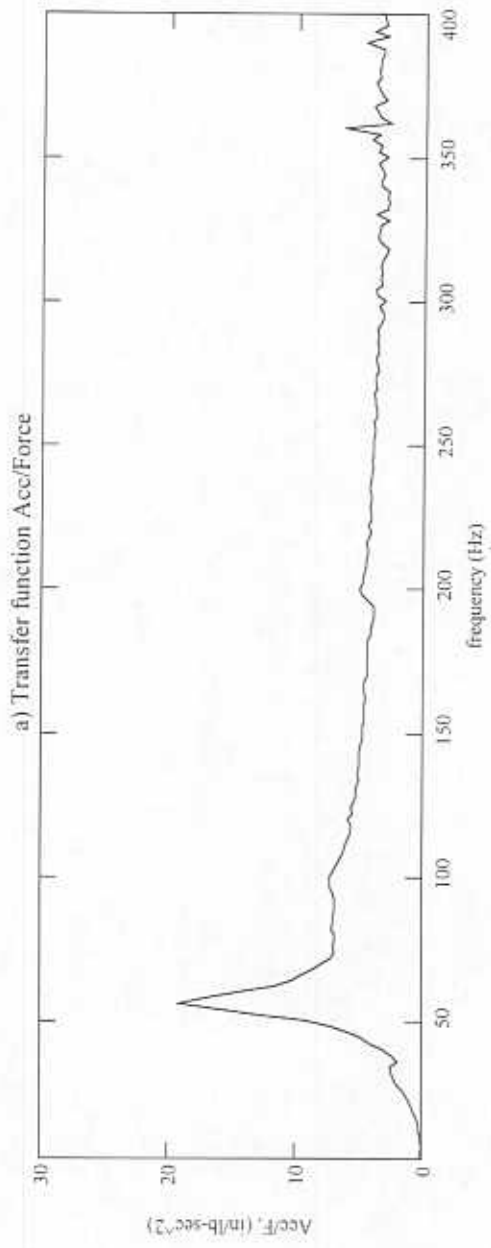
c) Coherence

Figure 13a. Identification of system damping from impact tests at middle disk and at zero rpm with oil at 73 °F. Vertical direction. a) Transfer function (acceleration/load) b) Acceleration vs. time c) Coherence
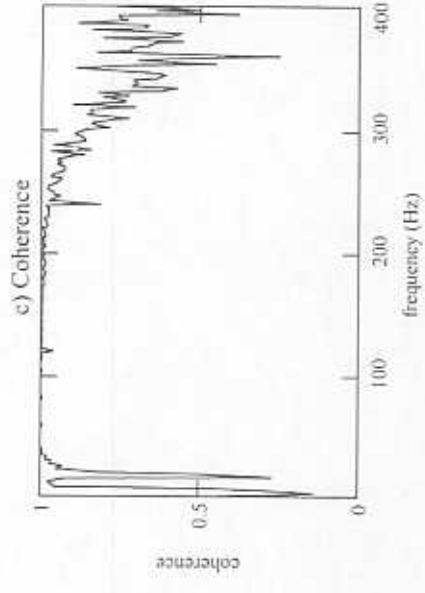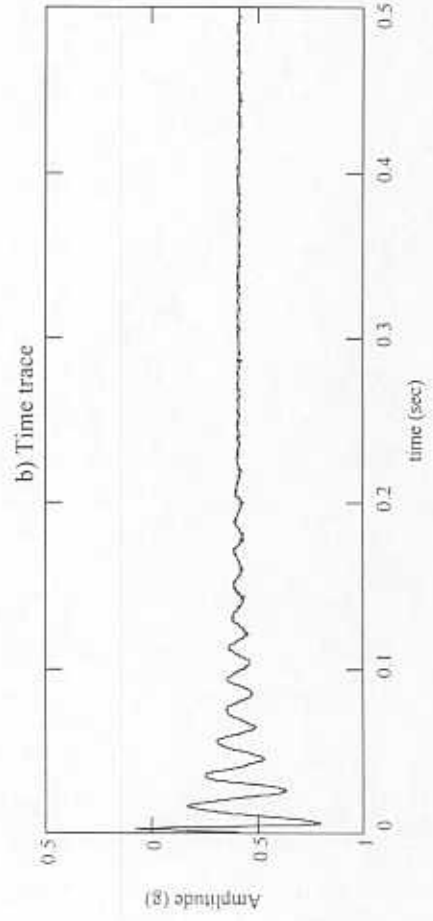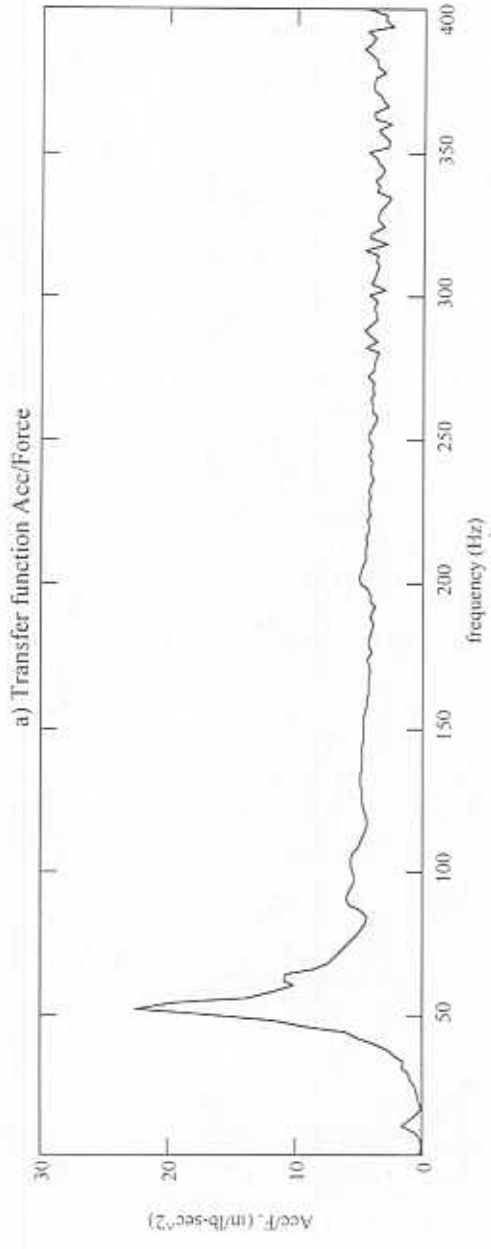
Figure 13b. Identification of system damping from impact tests at middle disk and at zero rpm with oil at 73 °F. Horizontal direction. a) Transfer function (acceleration/force) b) Acceleration vs. time c) Coherence

a) X/F drive end vertical

X/F, (m/N)   log scale

frequency (Hz)   log scale

b) Time trace drive end vertical

Amplitude of displacement (m)

time (sec)

c) Coherence drive end vertical

coherence

frequency (Hz)   log scale
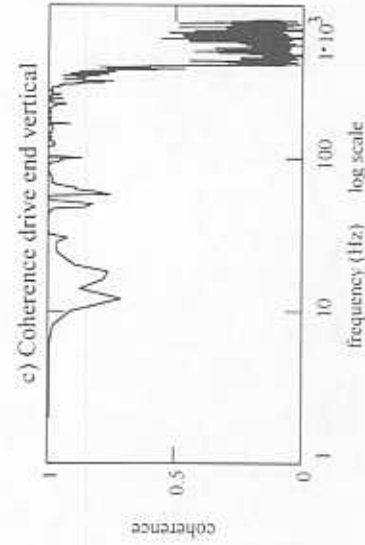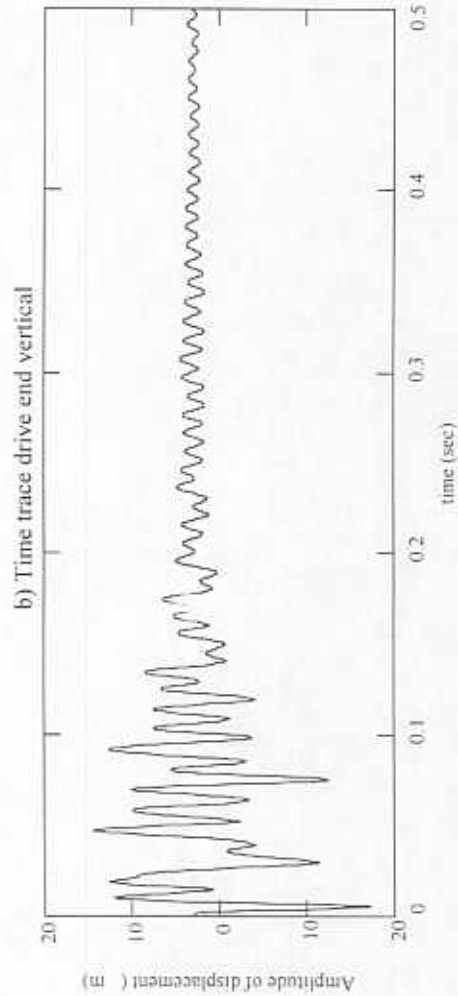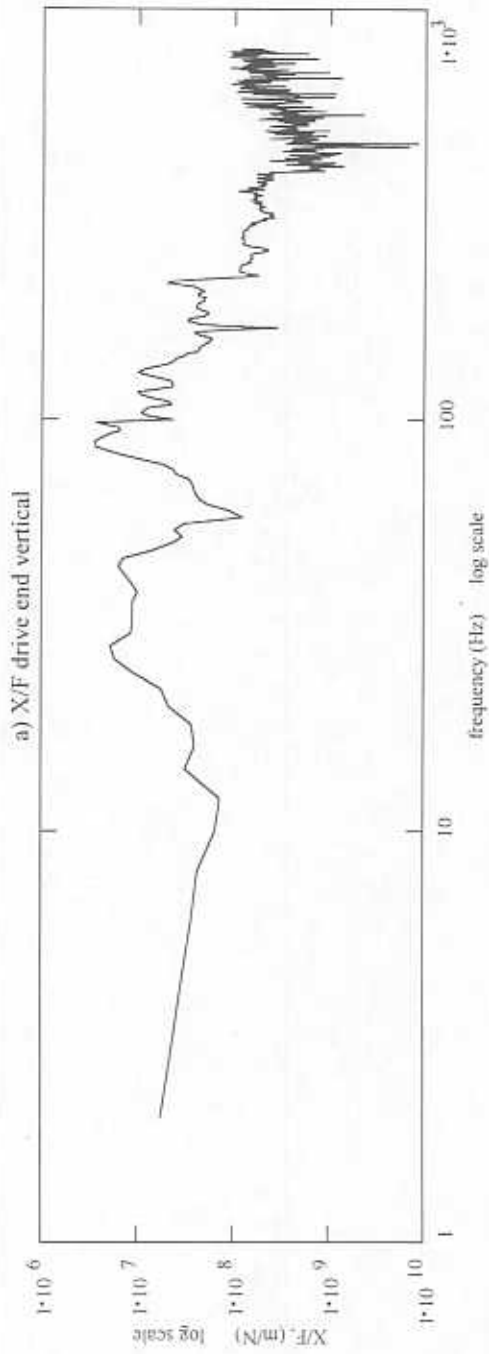
Figure 14a. Identification of drive end support stiffness from impact tests. Vertical direction.
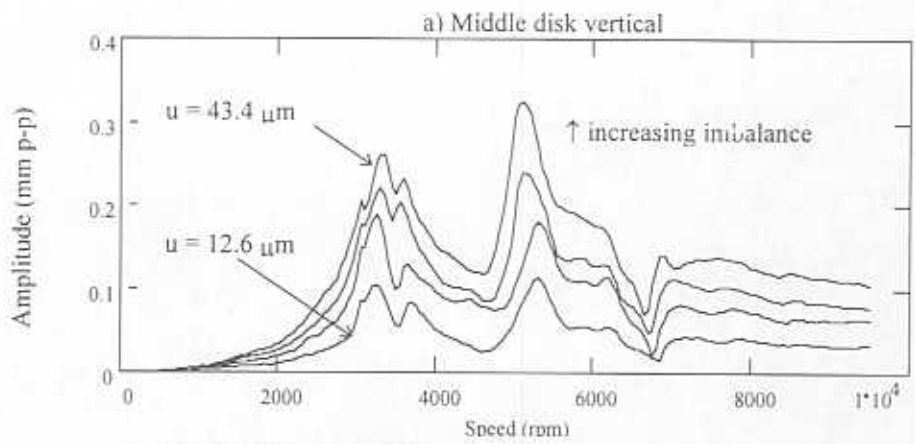**a) Transfer function (displacement/load) b) Disp. vs. time c) Coherence**

a) X/F drive end horizontal

frequency (Hz)   log scale

X/F, (m/N)   log scale

b) Time trace drive end horizontal

time (sec)

Amplitude of displacement (m)

c) Coherence drive end horizontal

frequency (Hz)   log scale
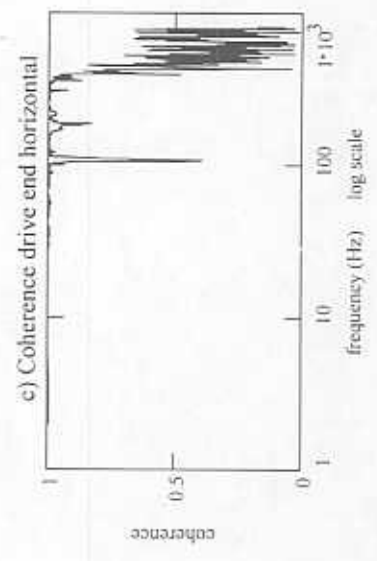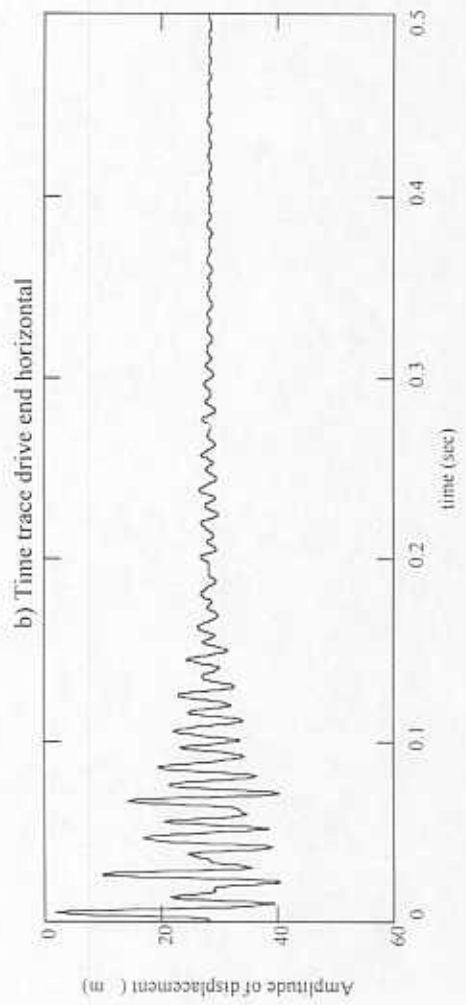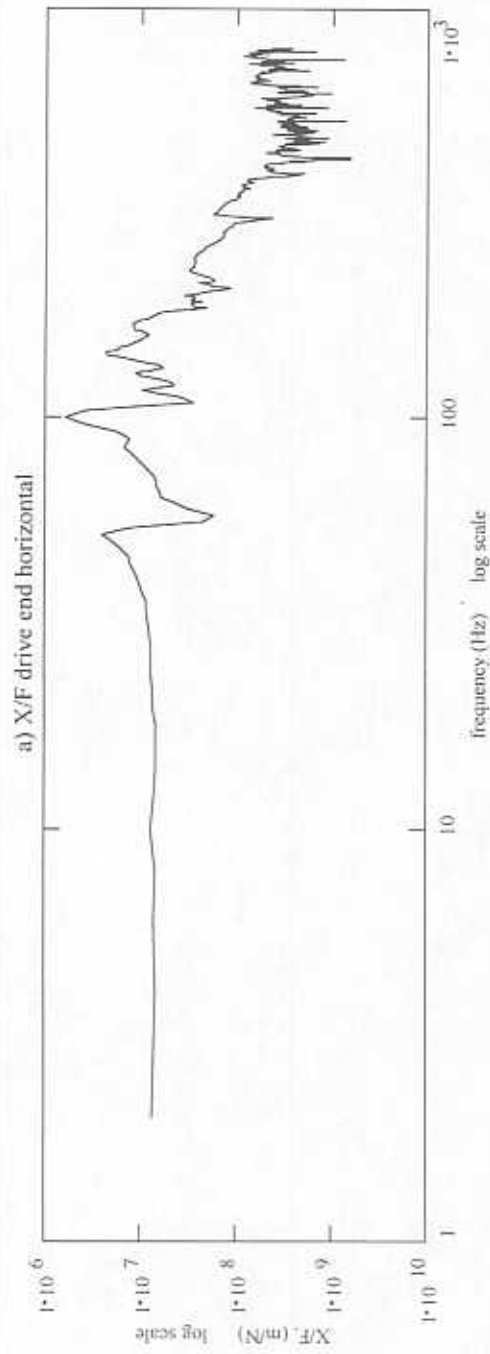
coherence

Figure 14b. Identification of drive end support stiffness from impact tests. Horizontal direction. a) Transfer function (displacement/load) b) Disp. vs. time c) Coherence

a) X/F free end vertical

b) Time trace free end vertical

c) Coherence free end vertical
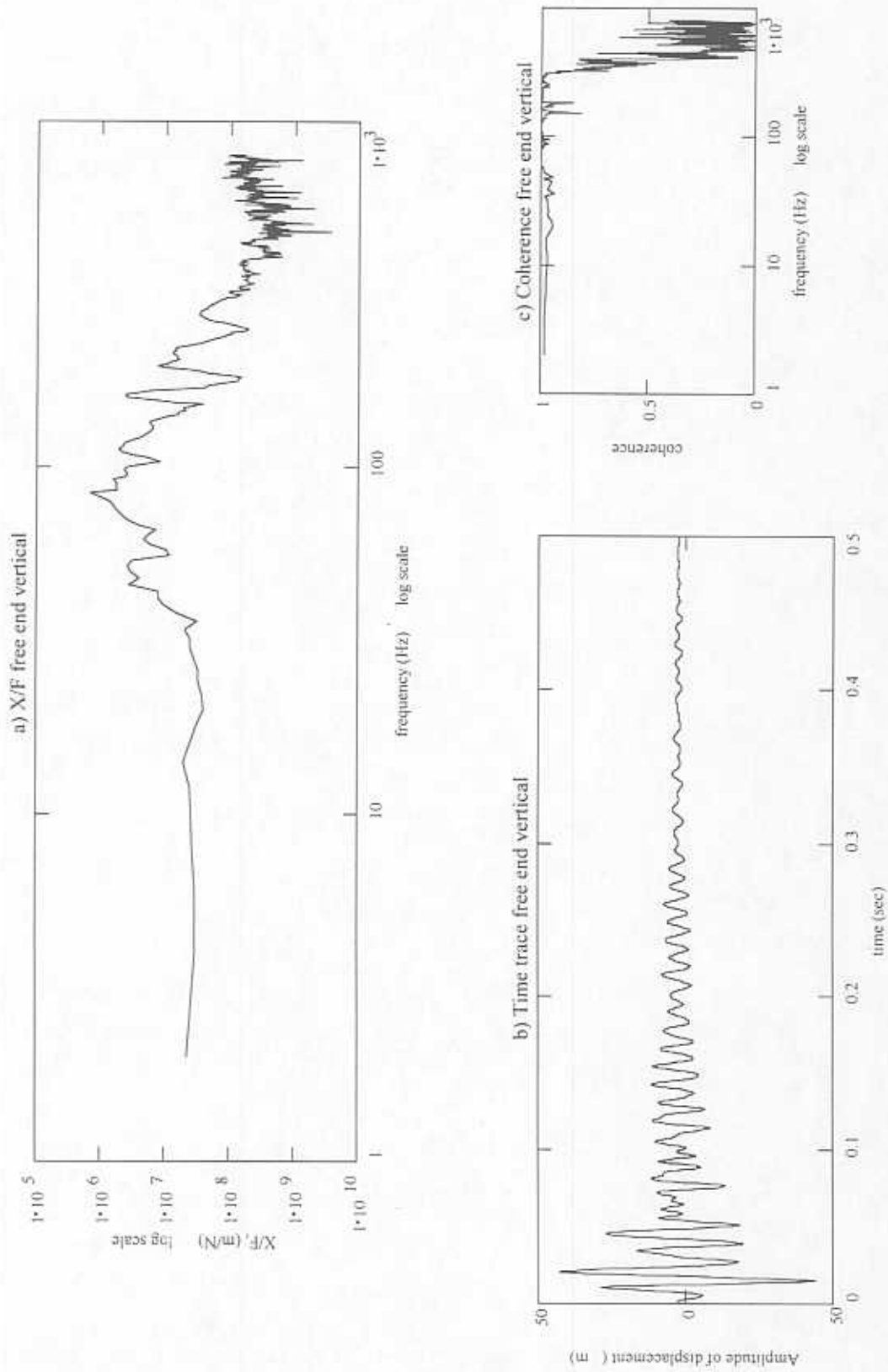
Figure 15a. Identification of free end support stiffness from impact tests. Vertical direction.
a) Transfer function (displacement/load) b) Disp. vs. time c) Coherence

a) X/F free end horizontal

X/F, (m/N)   log scale

frequency (Hz)   log scale

b) Time trace free end horizontal

Amplitude of displacement (m)

time (sec)

c) Coherence free end horizontal

coherence

frequency (Hz)   log scale
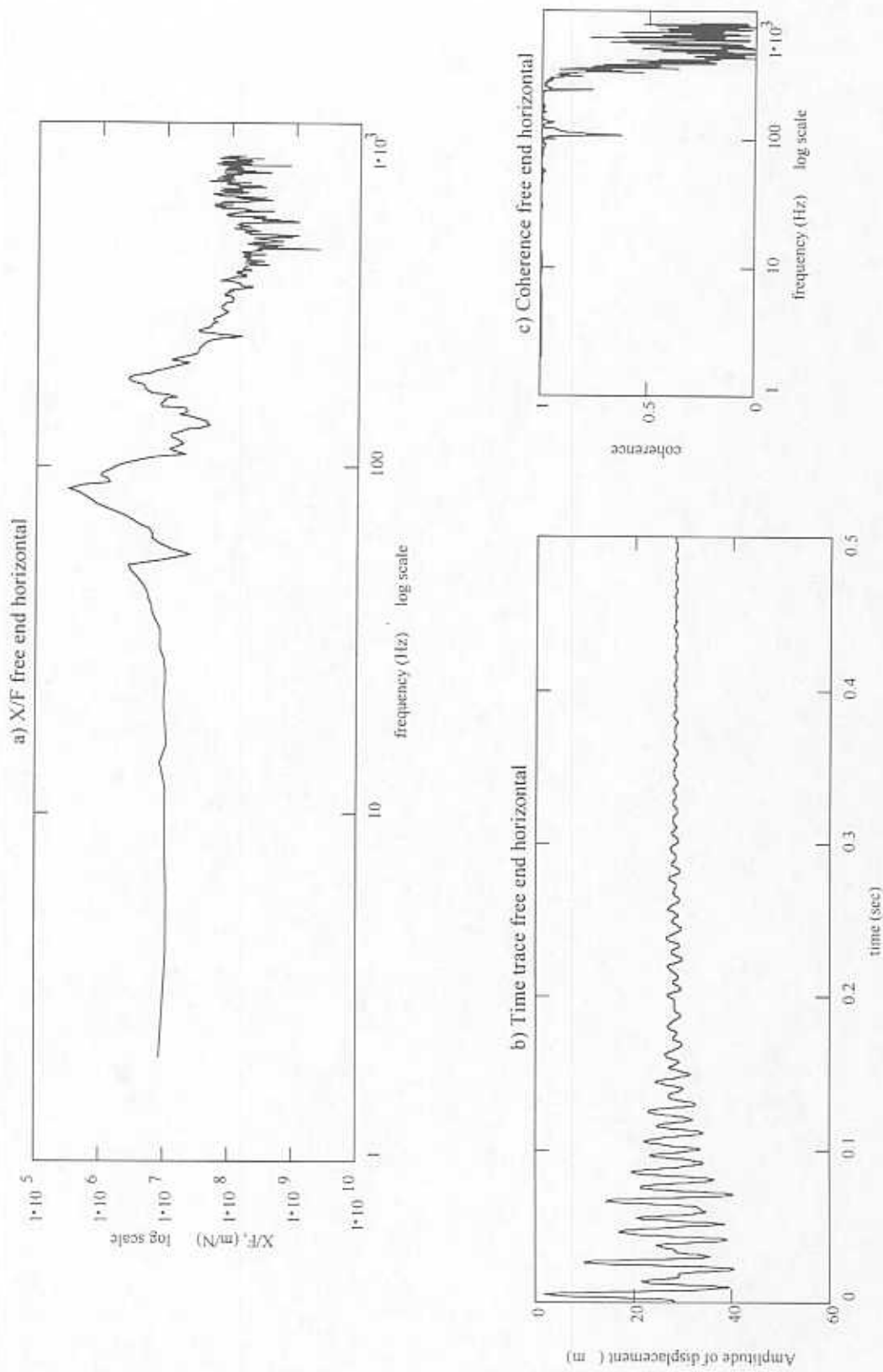
Figure 15b. Identification of free end support stiffness from impact tests. Horizontal direction.
a) Transfer function (displacement/load) b) Disp. vs. time c) Coherence

a) Drive end vertical

u = 43.4 μm →
u = 12.6 μm

↑ increasing imbalance

17gr. imbalance, u = 43.4 μm
13gr. imbalance, u = 33.2 μm
10gr. imbalance, u = 25.5 μm
5gr. imbalance, u = 12.6 μm

b) Drive end horizontal

u = 43.4 μm →
u = 12.6 μm

↑ increasing imbalance

17gr. imbalance, u = 43.4 μm
13gr. imbalance, u = 33.2 μm
10gr. imbalance, u = 25.5 μm
5gr. imbalance, u = 12.6 μm
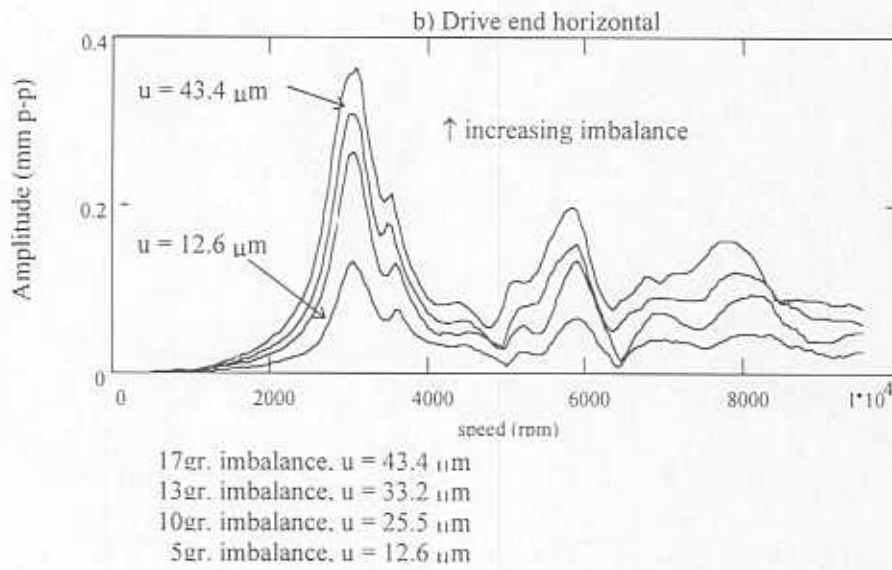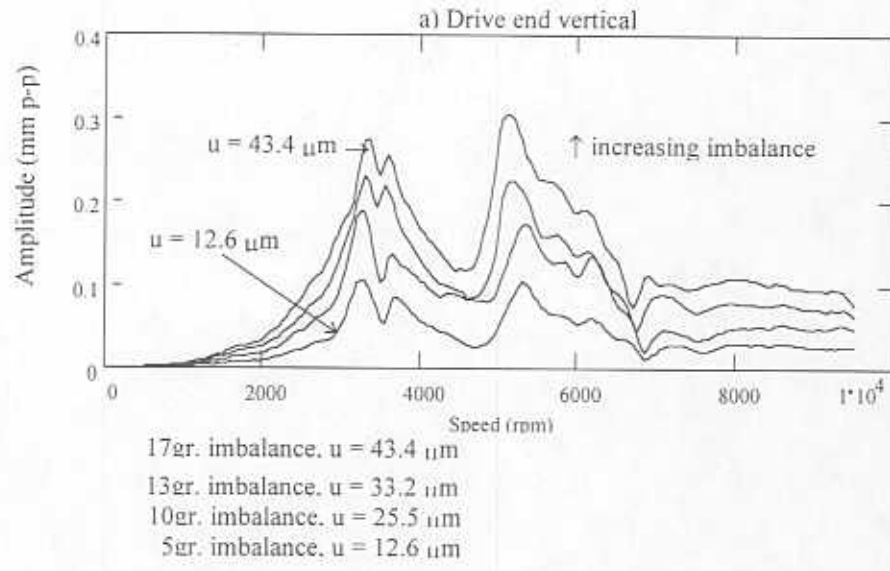
Figure 16. Synchronous imbalance response at drive end support for various levels of imbalance displacements a)vertical b) horizontal.

a) Middle disk vertical

u = 43.4 μm

↑ increasing imbalance

u = 12.6 μm

Amplitude (mm p-p)

Speed (rpm)

17gr. imbalance. u = 43.4 μm
13gr. imbalance. u = 33.3 μm
10gr. imbalance. u = 25.5 μm
5gr. imbalance. u = 12.6 μm

b) Middle disk horizontal

u = 43.4 μm

↑ increasing imbalance

u = 12.6 μm

Amplitude (mm p-p)

Speed (rpm)
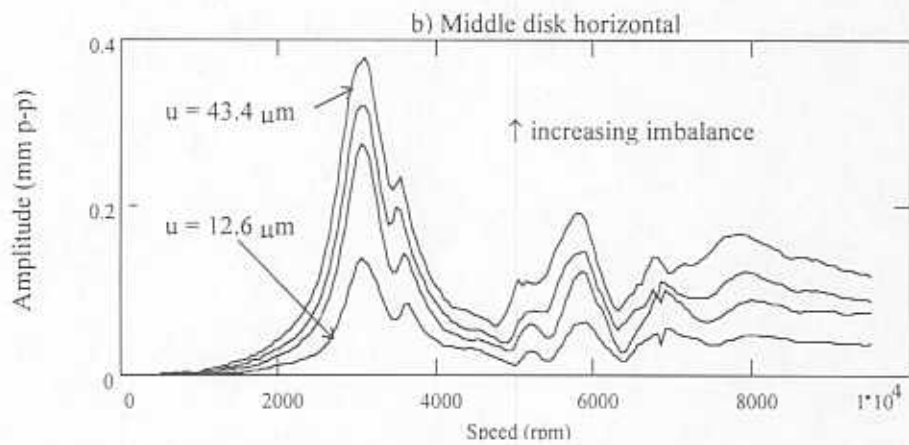
17gr. imbalance. u = 43.4 μm
13gr. imbalance. u = 33.2 μm
10gr. imbalance. u = 25.5 μm
5gr. imbalance. u = 12.6 μm

Figure 17. Synchronous imbalance response near middle disk
support for various levels of imbalance displacements
a)vertical b) horizontal.
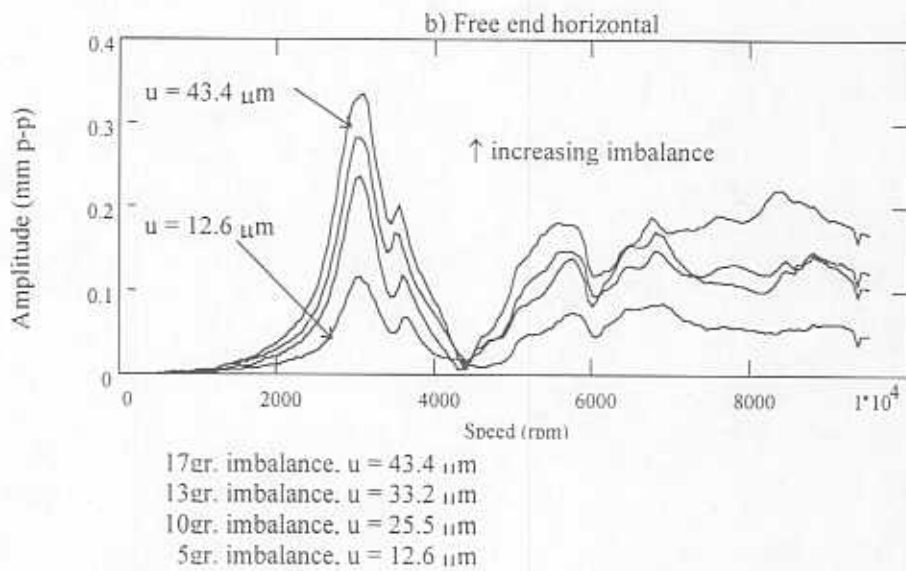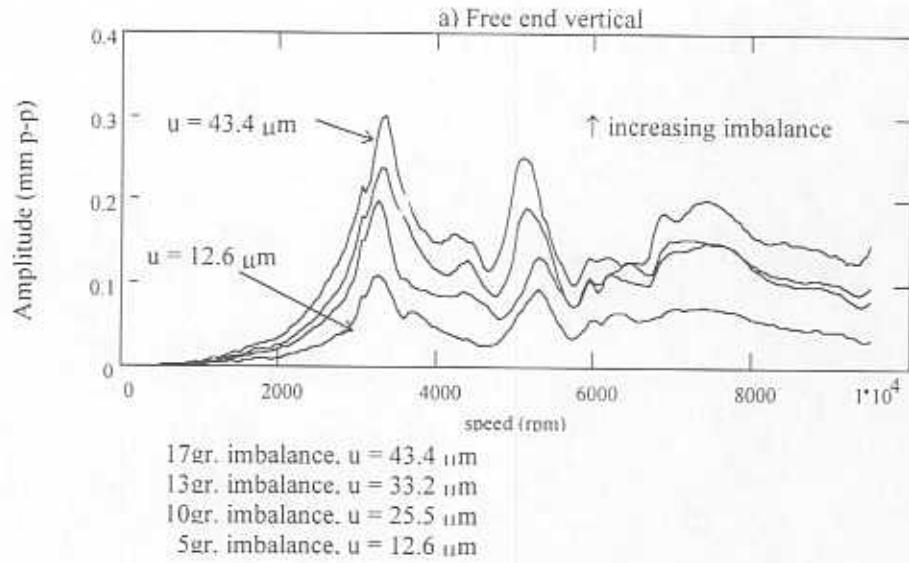
Figure 18. Synchronous imbalance response at free end
support for various levels of imbalance displacements
a)vertical b) horizontal.
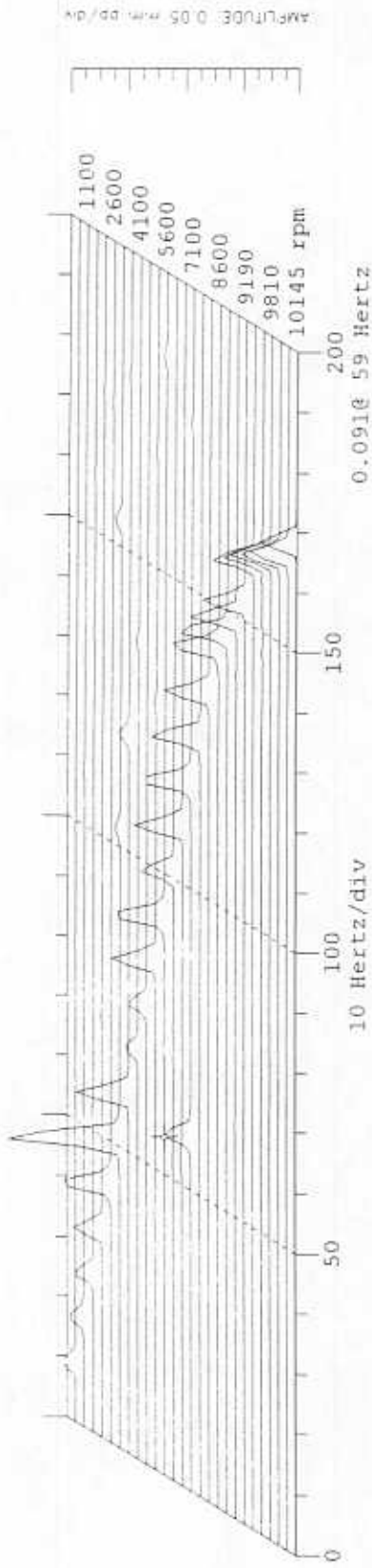
Figure 19. Cascade frequency plots of rotor displacement and support acceleration showing the appearance of 1/2 frequency whirl. Imbalance m=17g (u = 43 μm).
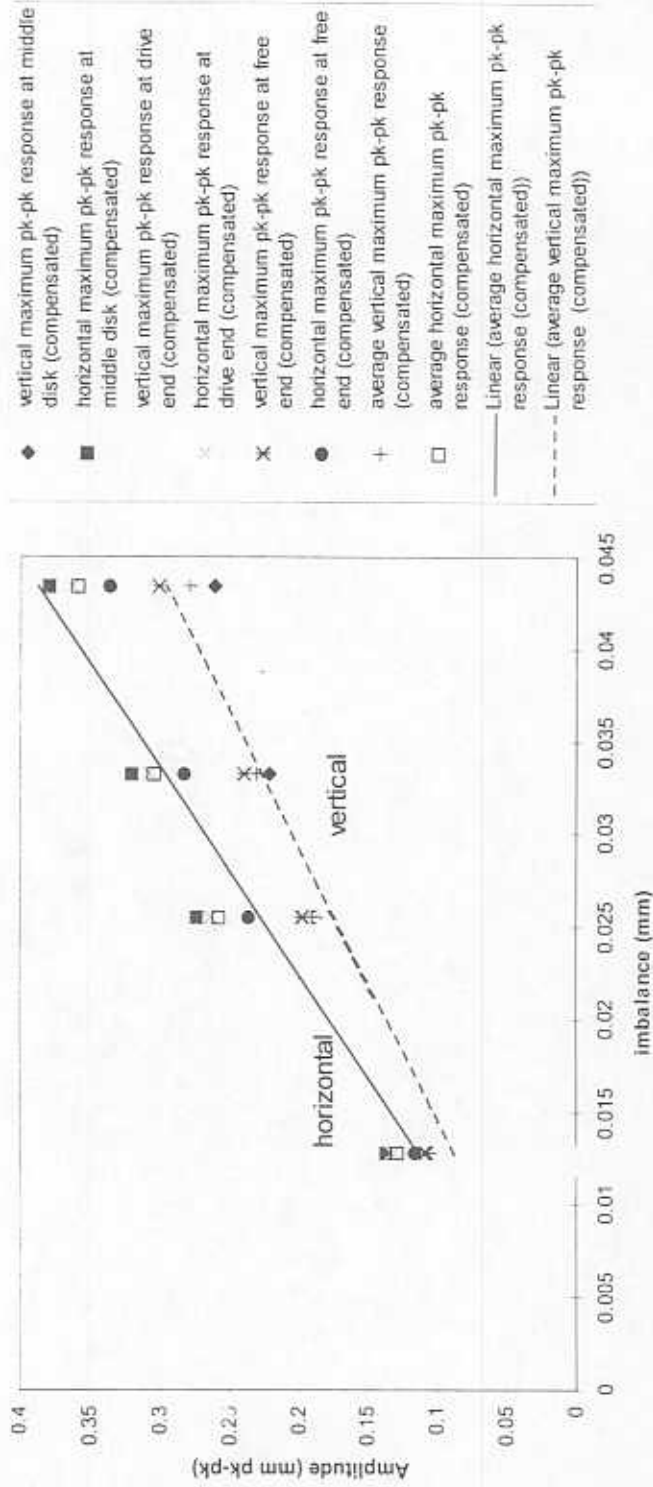
vertical maximum pk-pk response at middle disk (compensated)

horizontal maximum pk-pk response at middle disk (compensated)

vertical maximum pk-pk response at drive end (compensated)

horizontal maximum pk-pk response at drive end (compensated)

vertical maximum pk-pk response at free end (compensated)

horizontal maximum pk-pk response at free end (compensated)

average vertical maximum pk-pk response (compensated)

average horizontal maximum pk-pk response (compensated)

Linear (average horizontal maximum pk-pk response (compensated))

Linear (average vertical maximum pk-pk response (compensated))

vertical

horizontal

imbalance (mm)

Amplitude (mm pk-pk)

0.4
0.35
0.3
0.25
0.2
0.15
0.1
0.05
0

0   0.005   0.01   0.015   0.02   0.025   0.03   0.035   0.04   0.045

Figure 20. Peak-peak vibration amplitudes for synchronous imbalance response vs. imbalance displacements. Response at drive end, near middle disk, and free end of test rotor.
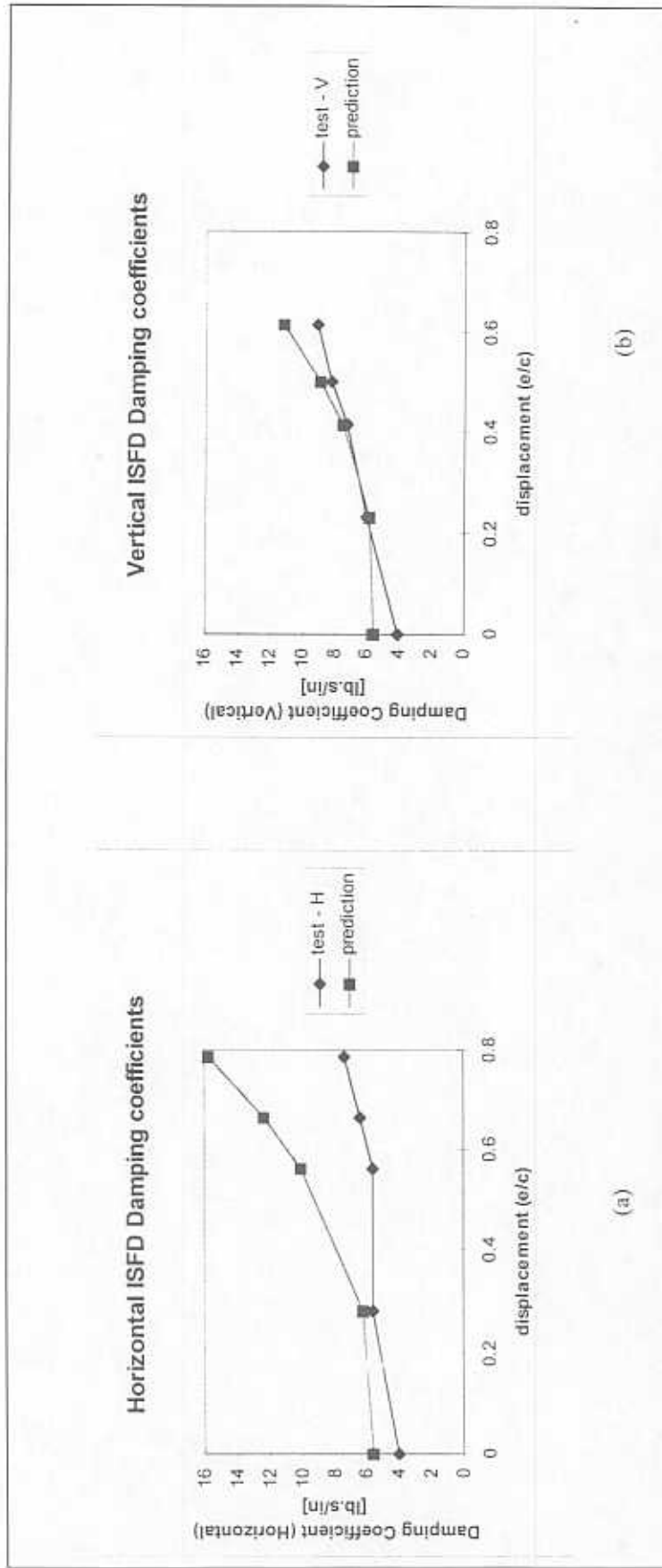
Figure 21. *ISFD's* damping coefficients estimated from imbalance tests and predictions *vs.* average journal center displacement (a) horizontal, (b) vertical.

a) Drive end horizontal

u = 43.4 μm (overall)

u = 43.4 μm

u = 12.6 μm

— 17 gr. imbalance, u = 43.4 μm
— 13 gr. imbalance, u = 32.2 μm
— 10 gr. imbalance, u = 25.5 μm
— 5 gr. imbalance, u = 12.6 μm
-- 17 gr. imbalance, overall vibration

b) Free end horizontal

u = 43.4 μm, (overall)

u = 43.4 μm

u = 43.4 μm

— 17 gr. imbalance, u = 43.4 μm
— 13 gr. imbalance, u = 33.2 μm
— 10 gr. imbalance, u = 25.5 μm
— 5 gr. imbalance, u = 12.6 μm
-- 17 gr. imbalance, overall vibration
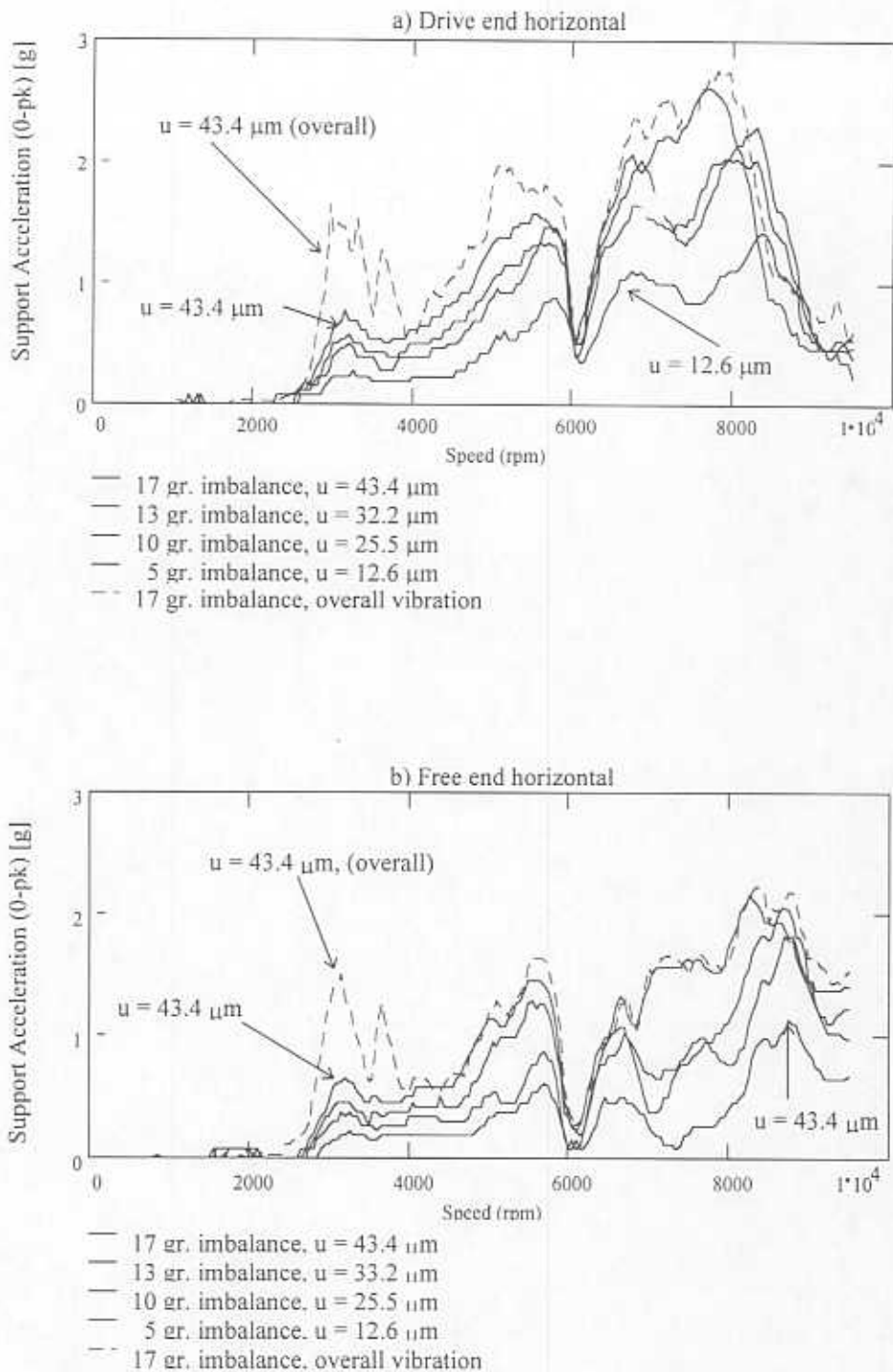
**Figure 22. Support horizontal acceleration (synchronous component)
vs. rotor speed for various levels of imbalance
(a) driven end support, (b) free end support.**
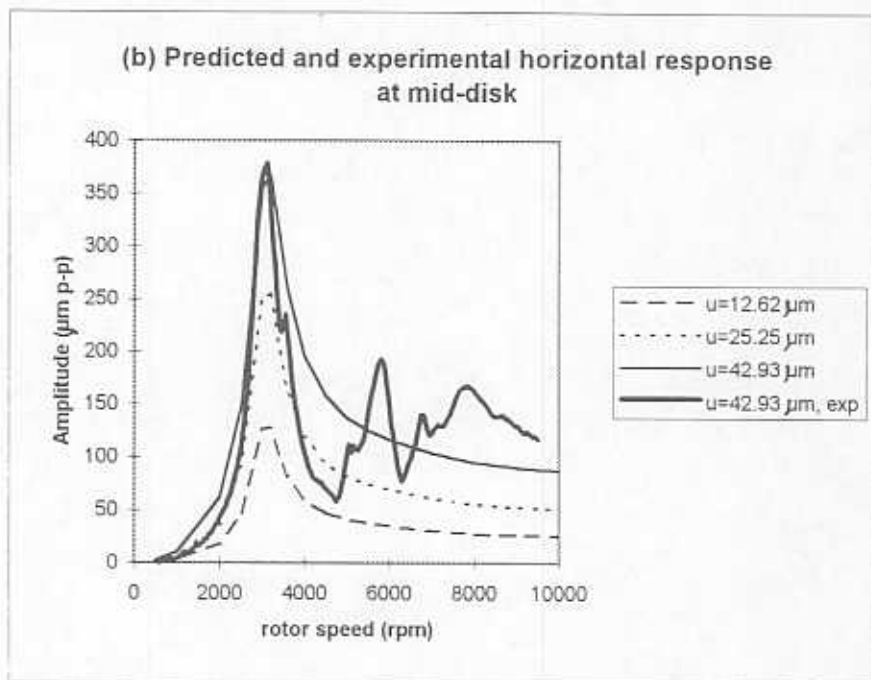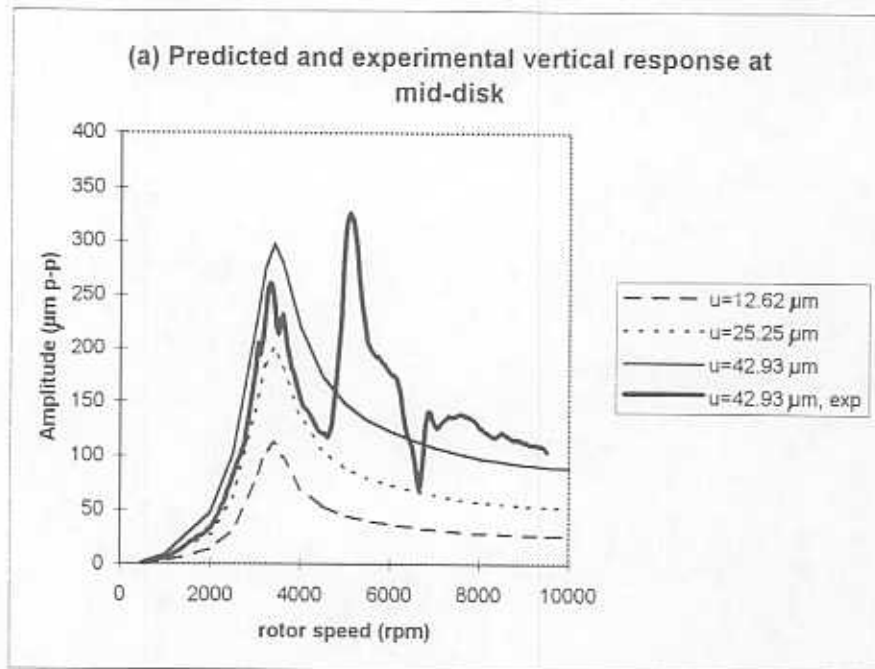
Figure 23. Predicted synchronous imbalance responses at rotor middle disk for various levels of mass imbalance and experimental response for 17 gr imbalance mass (compensated) (a) vertical (b) horizontal

APPENDIX A

FINITE ELEMENT ANALYSIS OF INTEGRAL SQUEEZE FILM DAMPERS

Figure A.1 depicts the geometry of a typical integral squeeze film damper with flexure pads, each of angular extent (β). An incompressible, isoviscous fluid fills the thin film lands between the flexure pad and the damper housing of diameter (D) and length (L). The journal instantaneous position is denoted by the displacements $[e_x(t), e_y(t)]$ relative to an inertial coordinate system.

Neglecting fluid inertia effects, the thin film fluid flow in a pad of angular extent (β) is given by the classical Reynolds equation:

$$\frac{\partial}{R^2 \partial \Theta}\left(\frac{h^3}{12\mu}\frac{\partial P}{\partial \Theta}\right) + \frac{\partial}{\partial z}\left(\frac{h^3}{12\mu}\frac{\partial P}{\partial z}\right) = \frac{\partial h}{\partial t}$$

(1)

in the region $\{0 \le \Theta \le \beta, 0 \le z \le L\}$, and where P is the squeeze film pressure generated by the temporal changes in the film thickness $\{h\}$ given as

$$h = c + e_x(t)\cos(\Theta) + e_y(t)\sin(\Theta)$$

(2.a)

$$\frac{\partial h}{\partial t} = \dot{e}_x \cos(\Theta) + \dot{e}_y \sin(\Theta)$$

(2.b)

where $[\dot{e}_x(t), \dot{e}_y(t)]$ are the instantaneous velocity components of the journal center. For an open ends damper configuration, the pressure is specified on all sides of the pads as ambient.

$$P(\Theta, 0) = P(\Theta, L) = P(0, z) = P(\beta, z) = P_a$$

(3)

The flow domain is discretized into a collection of 4-noded isoparametric finite elements, and the pressure over an element is then a linear combination of nodal values $\{\overline{P}\}_{i=1}^{n_n}$ and bilinear shape functions $\{\Psi\}_{i=1}^{n_n}$ given as

$$P^e = \sum_{i=1}^{n_n} \Psi_i \overline{P}_i^e$$

(4)

The Galerkin formulation reduces the pressure equation (1) into an algebraic system of linear equations:

$$\sum_{i=1}^{n_n} k_{ij}^e \overline{P}_i^e = -q_i^e + f_i^e$$

(5)

where

$$k_{ij}^e = \iint_{\Omega^e}\left(\frac{h^3}{12\mu}\right)^e\left\{\frac{1}{R^2}\frac{\partial \Psi_i}{\partial \Theta}\frac{\partial \Psi_j}{\partial \Theta} + \frac{\partial \Psi_i}{\partial z}\frac{\partial \Psi_j}{\partial z}\right\}^e R\, d\Theta\, dz$$

(6.a)

$$f_i^e = -\iint_{\Omega^e} \Psi_i^e [\dot{e}_x \cos(\Theta) + \dot{e}_y \sin(\Theta)] R\, d\Theta\, dz$$

(6.b)

$$q_i^e = \oint_{\Gamma} \Psi_i^e q_\eta d\Gamma^e \; ; \; \text{with} \; q_\eta = -\frac{h^3}{12\mu}\frac{\partial P}{\partial \eta}$$

(6.c)

as the flow rate through the element boundary (Γ). Equations (5) are applied over the entire flow domain and then condensed by enforcing the corresponding boundary conditions. A symmetric system of equations results and the system matrix is decomposed into its upper and lower triangular form. Backward and forward substitutions allow the calculation of the discrete squeeze film pressure field at the nodes of the flow domain.

Integration of the pressure field on each damper pad provides the damper reaction forces (F_x, F_y) to the journal kinematic motions.

$$\begin{Bmatrix} F_X \\ F_Y \end{Bmatrix} = \sum_{k=1}^{N} \int_{0}^{\beta_k} \int_{0}^{L} P_k \begin{Bmatrix} \cos(\Theta) \\ \sin(\Theta) \end{Bmatrix} R \, \partial\Theta \, \partial z \tag{7}$$

For circular centered orbits, $e_X = e \cos(\omega t)$ and $e_Y = e \sin(\omega t)$, where (ω) is the whirl frequency. The reaction fluid film forces are then used to calculate *SFD* damping coefficients by using the following relationships:

$$C_{XX} = \frac{-F_X}{\dot{e}_X} \; ; \; C_{XY} = \frac{-F_X}{\dot{e}_Y} \tag{8.a}$$

$$C_{YX} = \frac{-F_Y}{\dot{e}_X} \; ; \; C_{YY} = \frac{-F_Y}{\dot{e}_Y} \tag{8.b}$$

For an integral *SFD* with N pads, the numerical predictions show that the damper forces have dynamic components at N times the whirl frequency ω. Thus, the damping force coefficients are given as

$$C_{XX} = C_{YY} = C_M + C_f \cos(4\omega t) \, , \, \text{etc.} \tag{9}$$

where the subscripts M and f denote the mean and fluctuating values respectively.

The computer program *sfdflex.f* was developed using *Fortran77* within a Windows NT or Windows 95 32-bit operating system. Given a specified journal position and instantaneous velocity, the components program solves the finite element form of the Reynolds equation. The computed results are given as reaction forces and damping force coefficients in the (X,Y) directions.

REFERENCES

Klit, P. and Lund, J. W., 1988, "Calculation of the Dynamic Coefficients of a Journal Bearing Using a Variational Approach," *ASME Journal of Tribology*, Vol. 108, pp. 421 - 425.

NOMENCLATURE

|	
c	Nominal film clearance [m]
D	Bearing diameter [m]
$e_X(t), e_Y(t)$	Journal center displacements [m]
$\left[\dot{e}_X(t), \dot{e}_Y(t) \right]$	Journal center velocities [m/s]
F_X, F_Y	Fluid film forces [N]
h	Film thickness [m]
L	damper axial length [m]
N	Number of damper pads.
n_{pe}	Number of nodes per finite element
P, P_{cav}	*SFD* Pressure, cavitation pressure [Pa]
Pa	Ambient pressure [Pa]
q_n	Flow rate per unit length [m^3/s]
R	damper radius, $\left(\frac{D}{2}\right)$ [m]
t	Time [s]
$(x = R\Theta, z)$	Fixed coordinate system attached to the bearing housing.
(X, Y)	Inertial coordinate system
β	Pad angular extent [rads].
Γ	Element boundary
μ	Fluid viscosity [Pa·s]
ρ	Fluid density $\left[\frac{kg}{m^3}\right]$
$\{\Psi\}_{i=1}^{n_{pe}}$	Shape functions
ω	whirl frequency $\left[\frac{rad}{s}\right]$
Ω^e	Finite element sub-domain

DETAIL
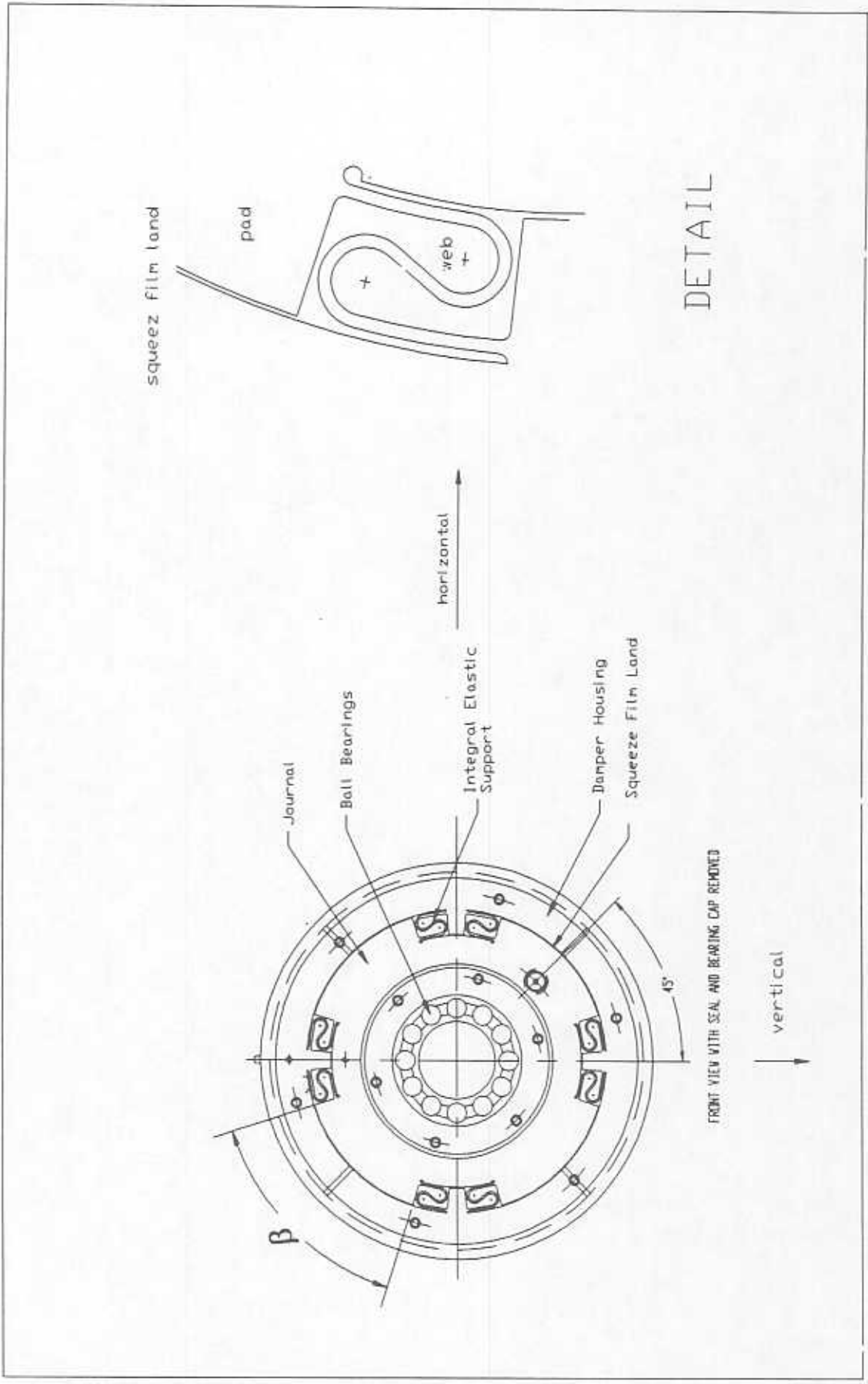
Figure A1. Integral SFD geometry

APPENDIX B
IDENTIFICATION OF LATERAL STIFFNESS OF INTEGRAL SQUEEZE FILM DAMPERS
(*ISFDs*)[1]

The stiffness characteristics of the *ISFDs* were determined using a systematic procedure which comprised of the following steps:
a) assembly of the set-up for the experiments.
b) calibration of the instrumentation.
c) measurement of the load vs. deflection characteristics of the integral dampers.
d) identification of the static stiffness and extent of linear gap and clearance for the various angular locations of load application, and
e) verification of the identified stiffness with an indirect method which extracts the stiffness from measurements of the fundamental natural frequency of each damper and estimated masses.

A strain-gage load cell was calibrated with dead weights, and the corresponding sensitivity factor was determined. The calibration factors for the load cell are:

Supply = 10 ± 0.01 V
Sensitivity (m) = 0.03913 V/lb Standard error $(s_m) = 3.387 \cdot 10^{-11}$
Correlation (r) = 99.9999 %   Load standard error $(s_{load}) = 3.208 \cdot 10^{-7}$ lb

The tested load cell exhibited a highly linear response with an extremely precise output.

An Eddy current displacement sensor (Bently Nevada proximity probe type 300-02-12-36-02) was calibrated using the support shaft as target. The shaft was mounted on a lathe provided with a digital carriage position display with 0.005 in (5 mils) resolution, and the proximity probe was attached to the lathe carriage. Calibrations for the probe output at 0.005 in displacement intervals were performed both with and without a probe extension cable.

Both calibrations showed a non-linear output for the used probe / supply module combination. However, by fitting quadratic polynomials to the experimental data correlation factors (R2) of 99.89% and 99.88% were obtained. Since the application of these calibrations only involved static measurement procedures, the use of quadratic characteristics was considered satisfactory. The same proximity probe was calibrated on the lathe but having one *ISFD* as target. Both calibrations showed again a non-linear output with data correlation factors (R2) of 99.82% and 99.81% for quadratic polynomial fits.

The support fixture for the *ISFDs* was tested for deflection under applied loads in the range of 0 to 250 lbs. The applied load was measured with the strain-gage load cell and the deflection was measured with the calibrated proximity probe. **Figure 1** shows a diagram of the experimental set-up, and the resulting support deflection is plotted in **Figure 2**.

---

[1] The stiffness measurements and reported results were performed by Dr. Juan Oliveras of the Univesidad Simon Bolivar (Caracas, Venezuela). Dr. Oliveras was then a Visiting Research Associate at the TAMU Rotordynamics Laboratory.
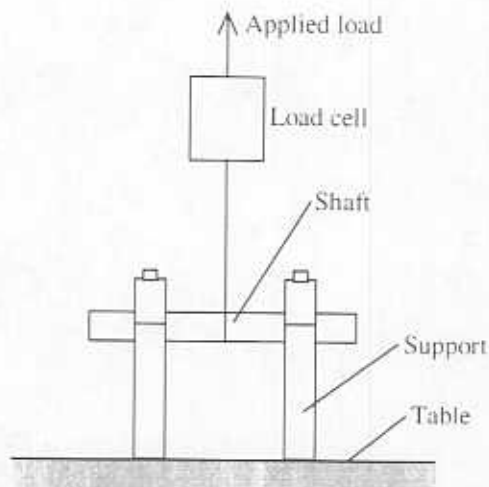
Figure 1. Experimental set-up for measuring the support deflection under load.

Support Displacement

$$y = 2E\text{-}08x^2 - 9E\text{-}06x - 2E\text{-}05$$
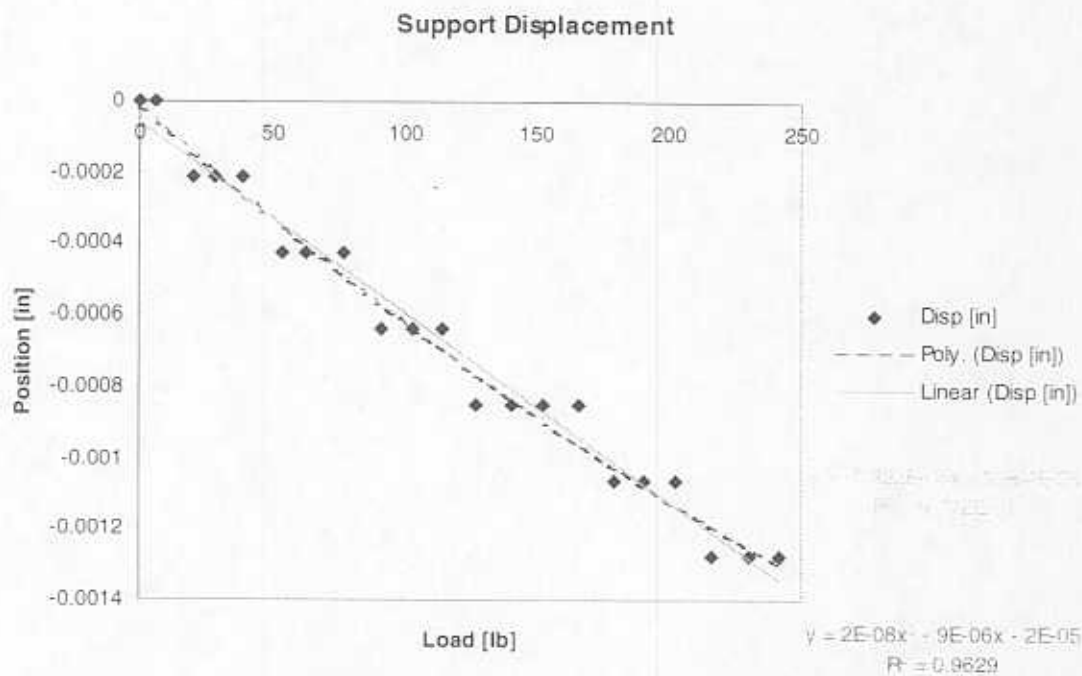$$R^2 = 0.9629$$

Figure 2. Support shaft deflection under applied loads.

The support deflection characteristic shows discrete position increments due to resolution limitations in the voltmeter used to monitor the proximity probe output. However, a linear fit for the data produced a correlation factor of 97.72%, and was considered satisfactory for correcting the deflection measurements during the *ISFD*s stiffness characterization.

Each *ISFD* was tested to obtain the stiffness characteristics in the radial direction, by applying tension loads in the range 0 - 250 lbs and measuring the corresponding deflections. The measured displacements were corrected for the support deflection by using the linear characteristic obtained from the calibration shown in Figure 3. **Figure 3** illustrates the experimental set-up.
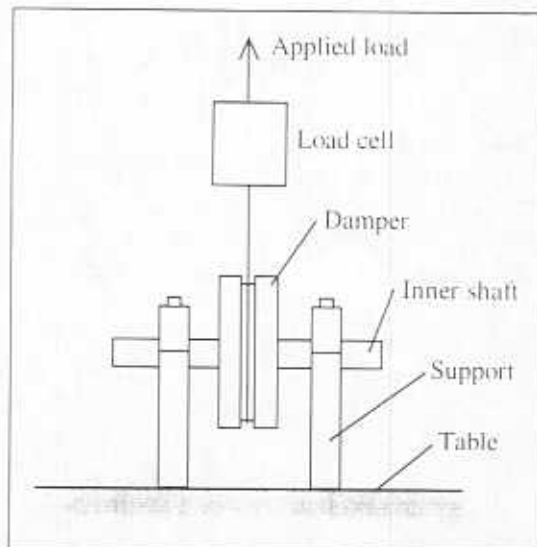
Figure 3. Experimental set-up for measuring the *ISFDs* stiffness characteristics.

Tests were repeated at regular 45° rotation intervals, so that a total of eight stiffness characteristics were obtained for each damper, showing the variation in stiffness when the load was applied towards each arcuate pad or towards the flexible webs acting as springs. Additional tests were performed for position 360° (0°) of each damper as a means of assessing the repeatability of the tests.

Figures 4-a through **4-i** show the load vs. deflection (stiffness) graphs obtained for *ISFD* #1, while **Figures 4-j** through **4-r** illustrate the load vs. deflection measurements corresponding to *ISFD* #2. On the plots it is clear that a linear characteristic is maintained for most of the deflection range, until partial pad contact occurs. The change of stiffness and its asymptotic tendency gave a good indication of the actual clearances in dampers #1 and #2.

SFD #1 - Stiffness 0°

Figure 4-a. Stiffness characteristic from *ISFD* #1 - 0° (↓ vertical loading).
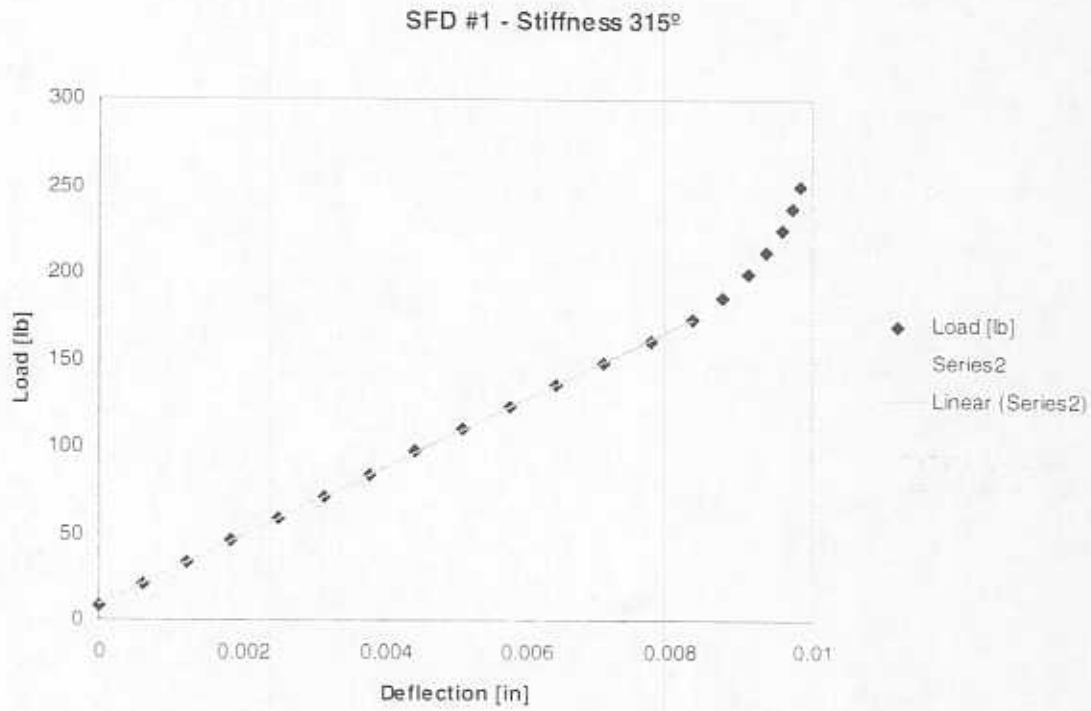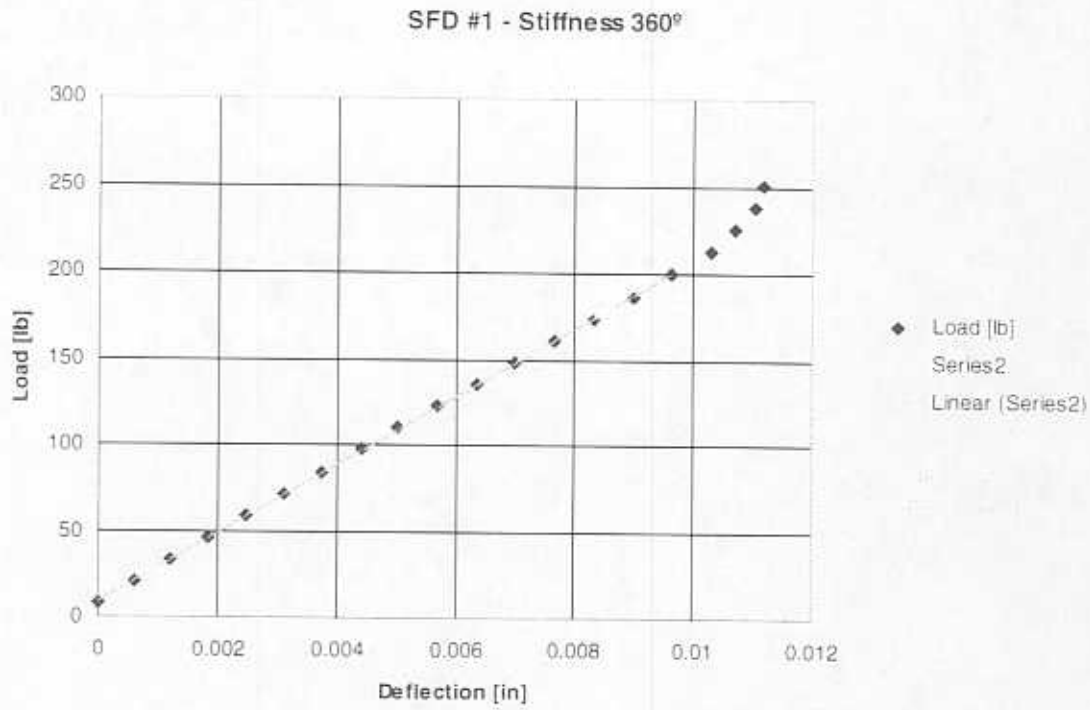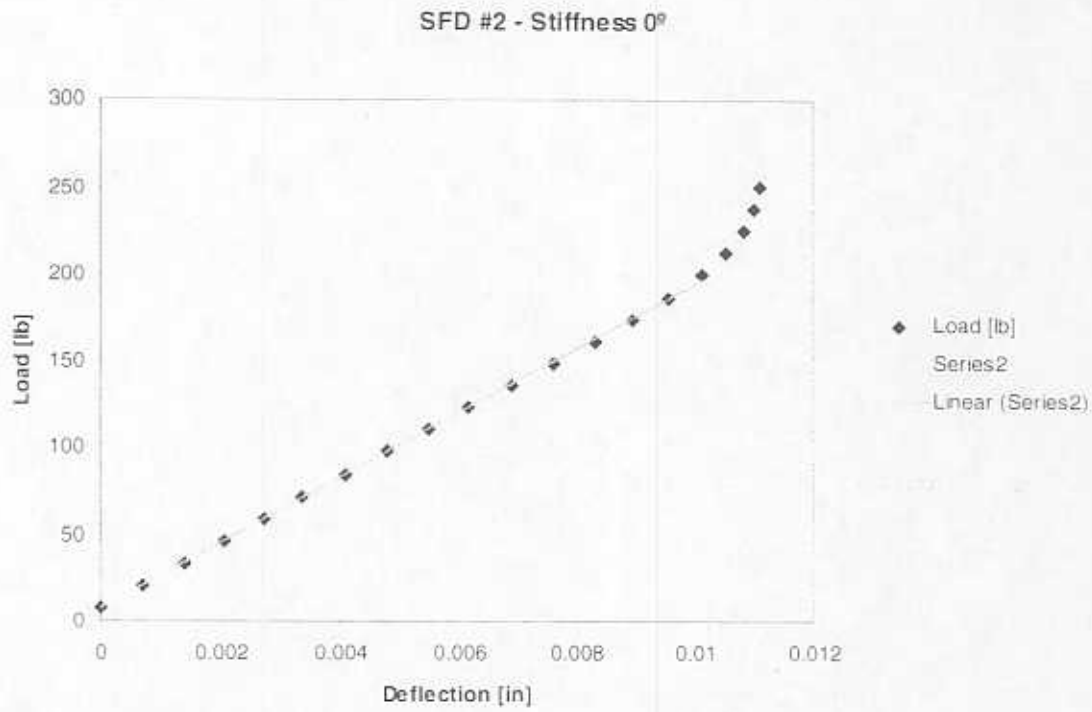
SFD #1 - Stiffness 45°

Figure 4-b. Stiffness characteristic from *ISFD* #1 - 45°.
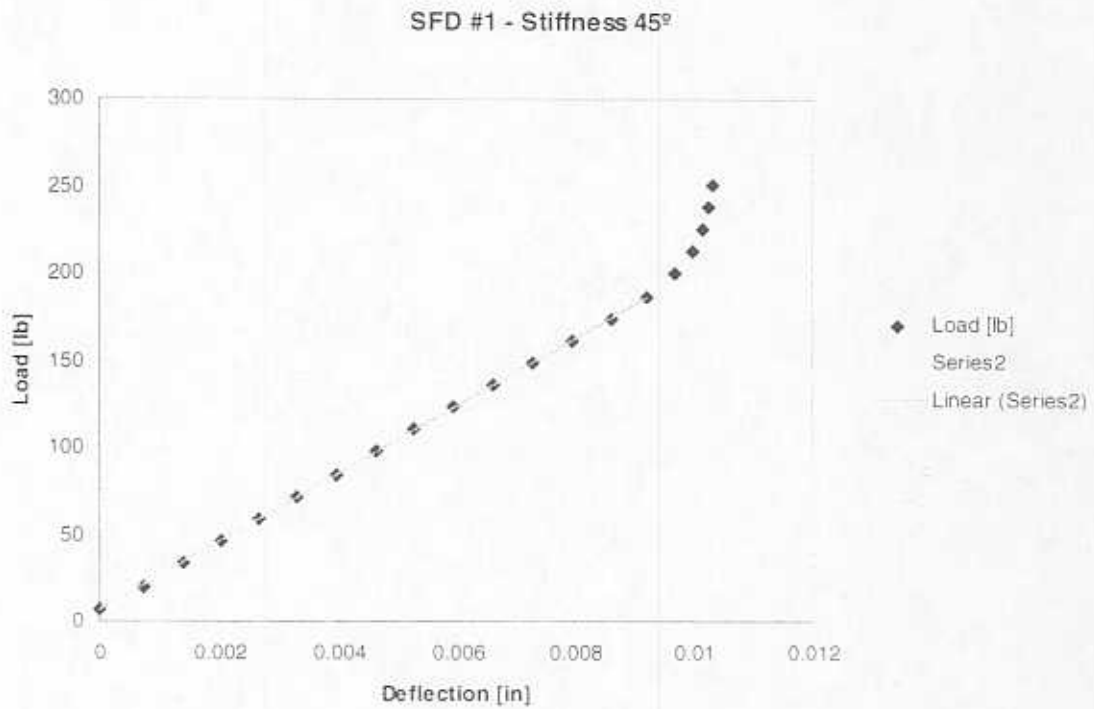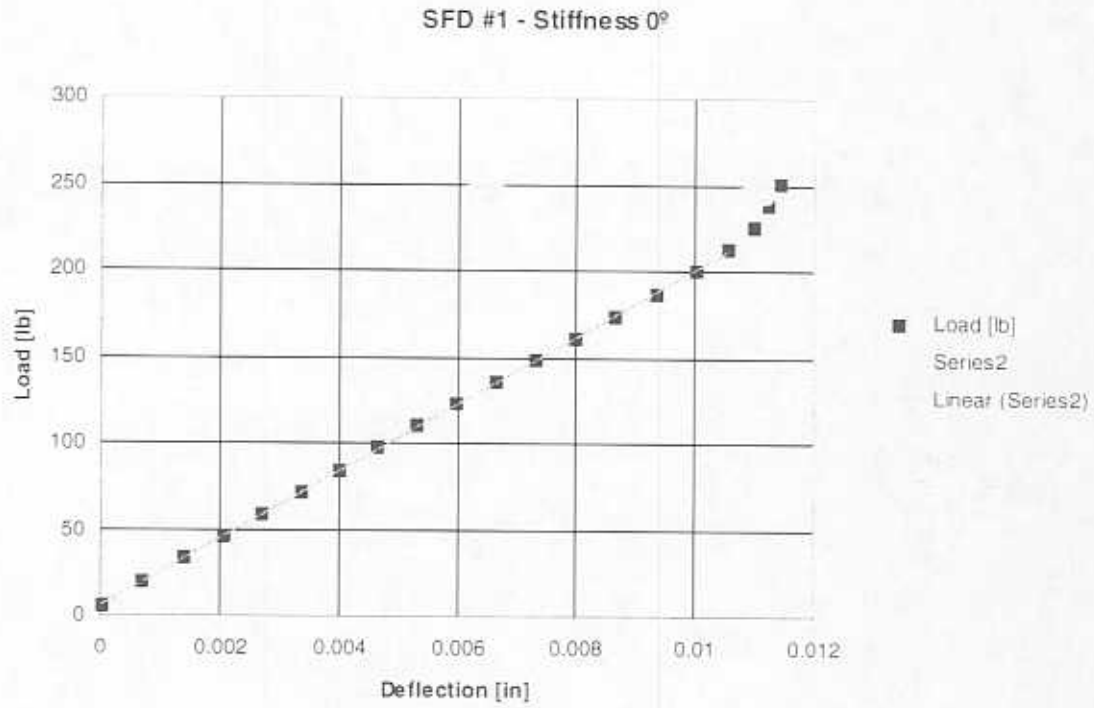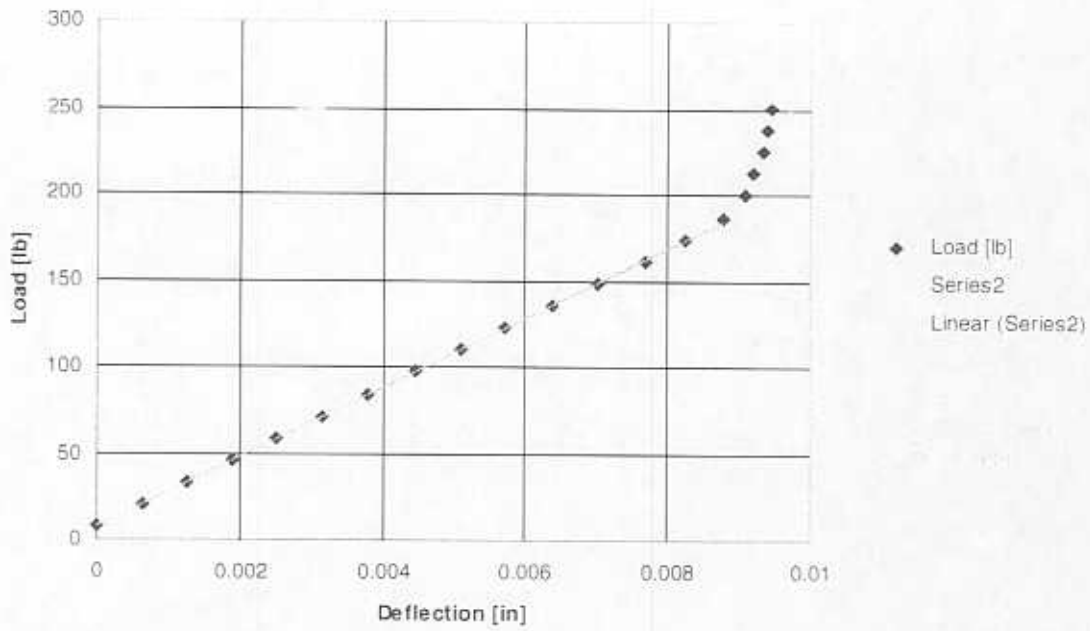
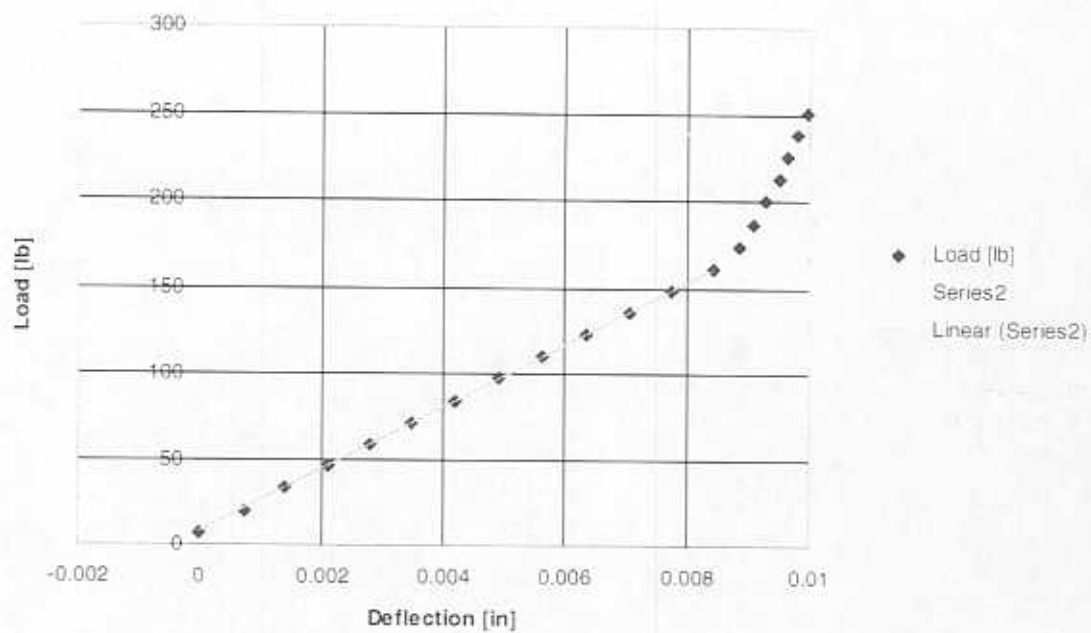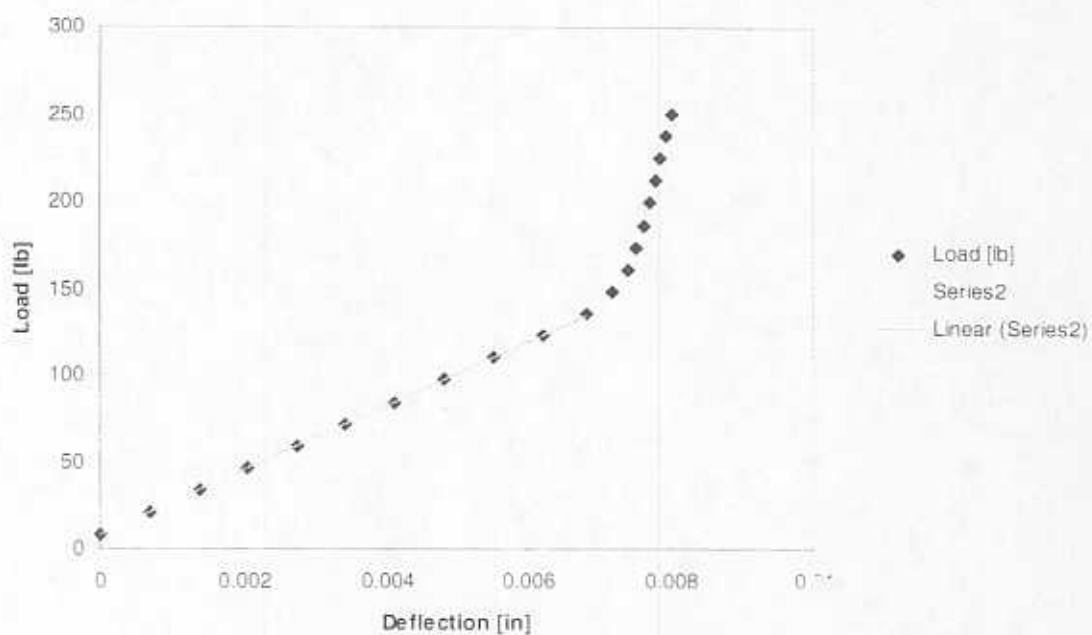**Figure 4-c.** Stiffness characteristic from *ISFD* #1 - 90° (← horizontal loading).
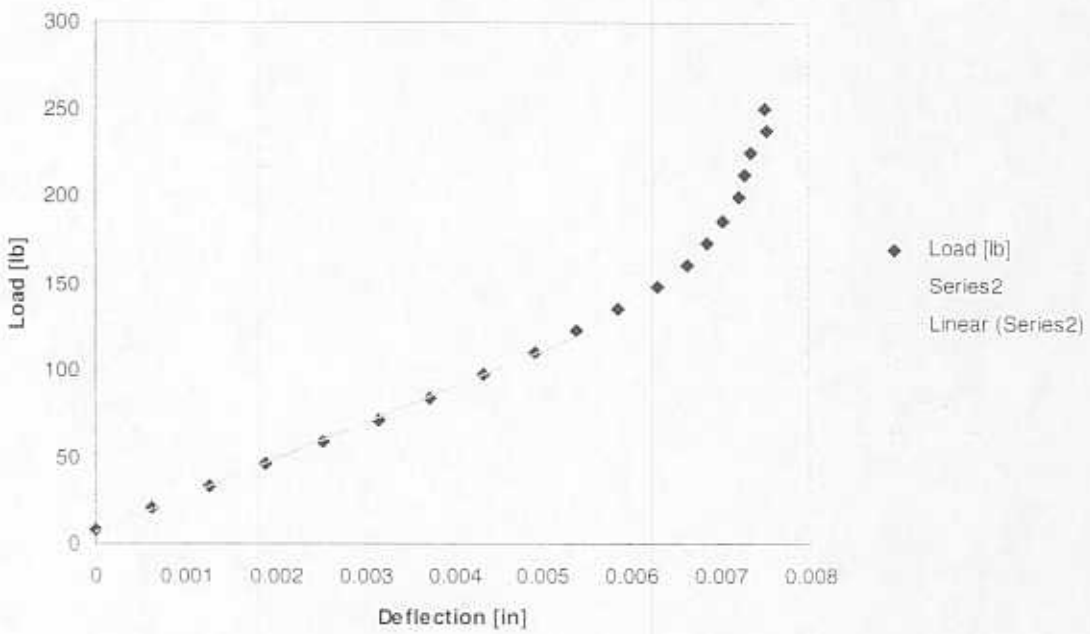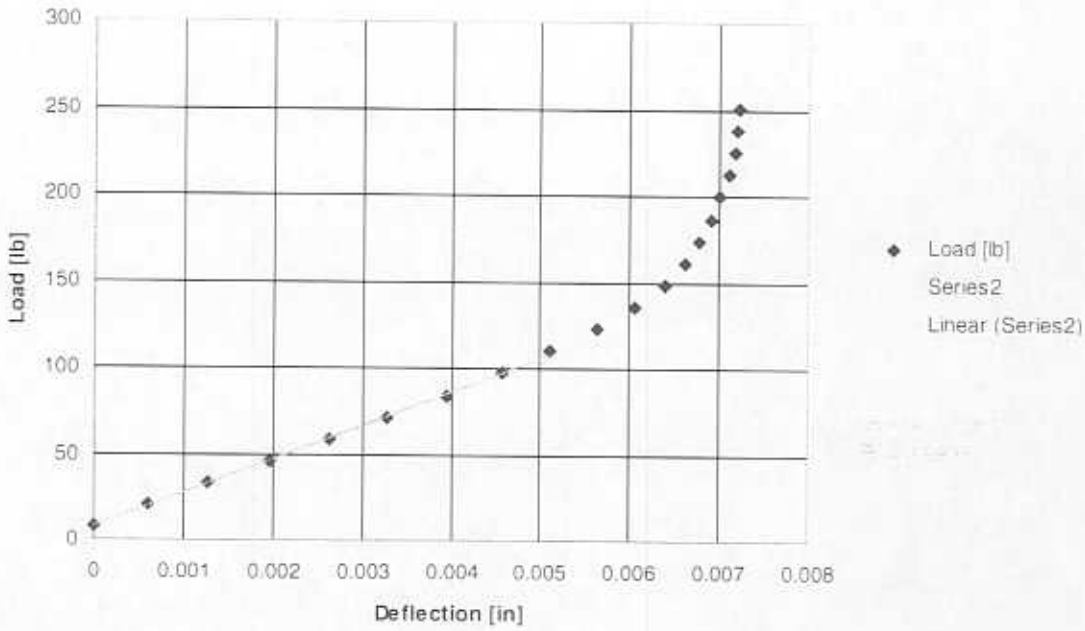

Figure 4-d. Stiffness characteristic from *ISFD* #1 - 135°.

SFD #1 - Stiffness 180º
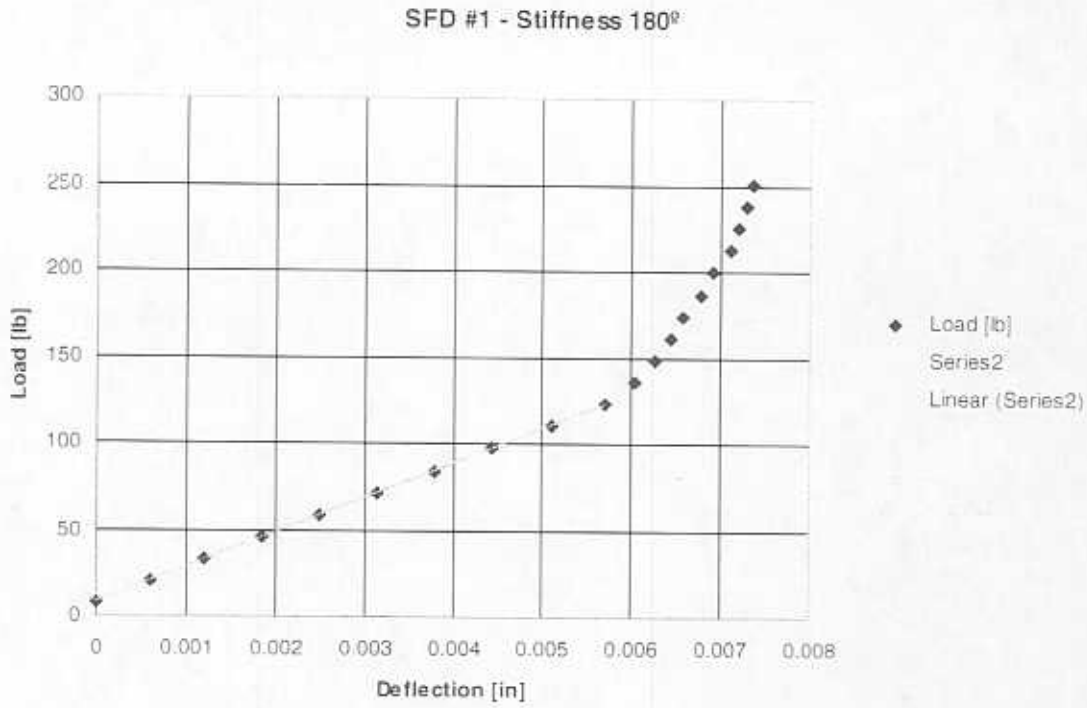
Figure 4-e. Stiffness characteristic from *ISFD* #1 - 180º (↑ vertical loading).
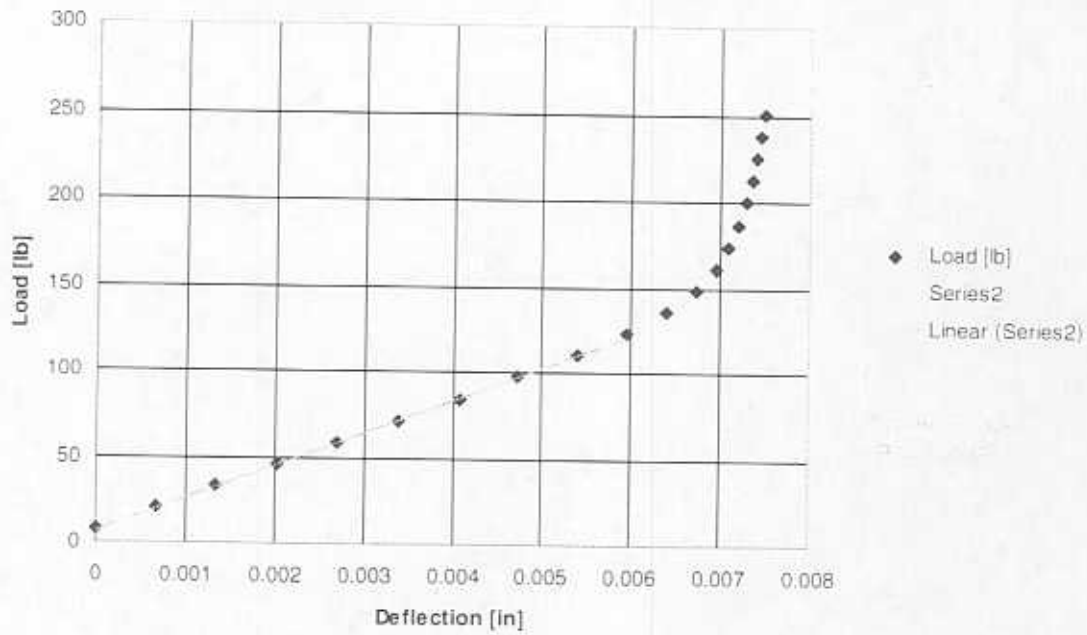
SFD #1 - Stiffness 225º
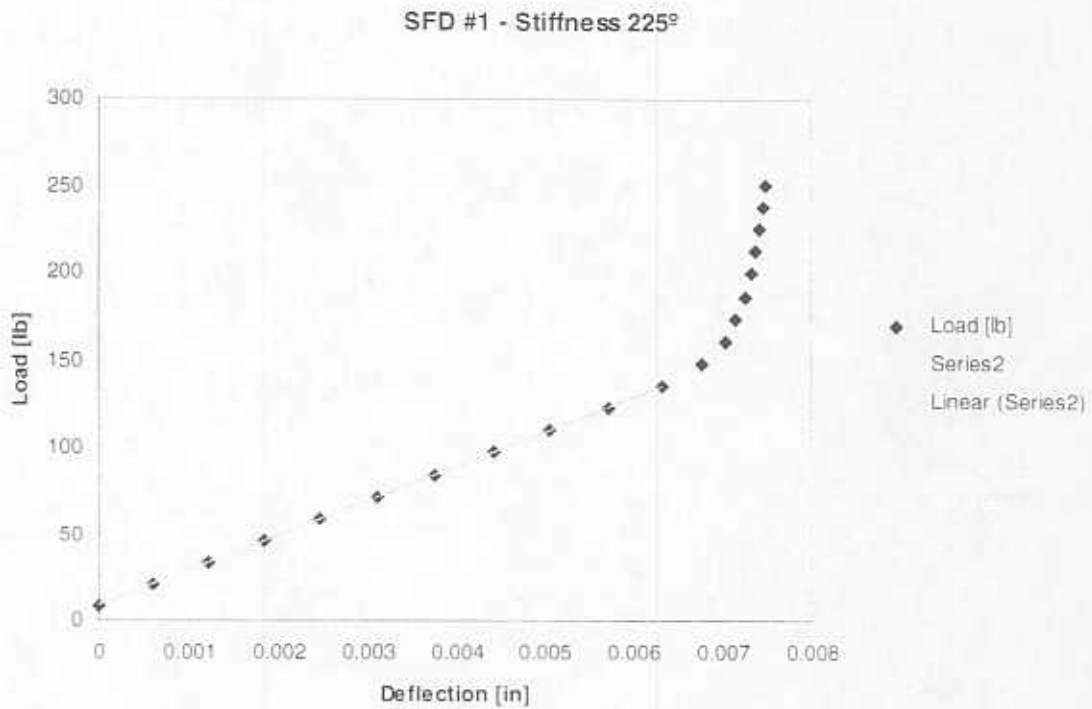
Figure 4-f. Stiffness characteristic from *ISFD* #1 - 225º.

SFD #1 - Stiffness 270º
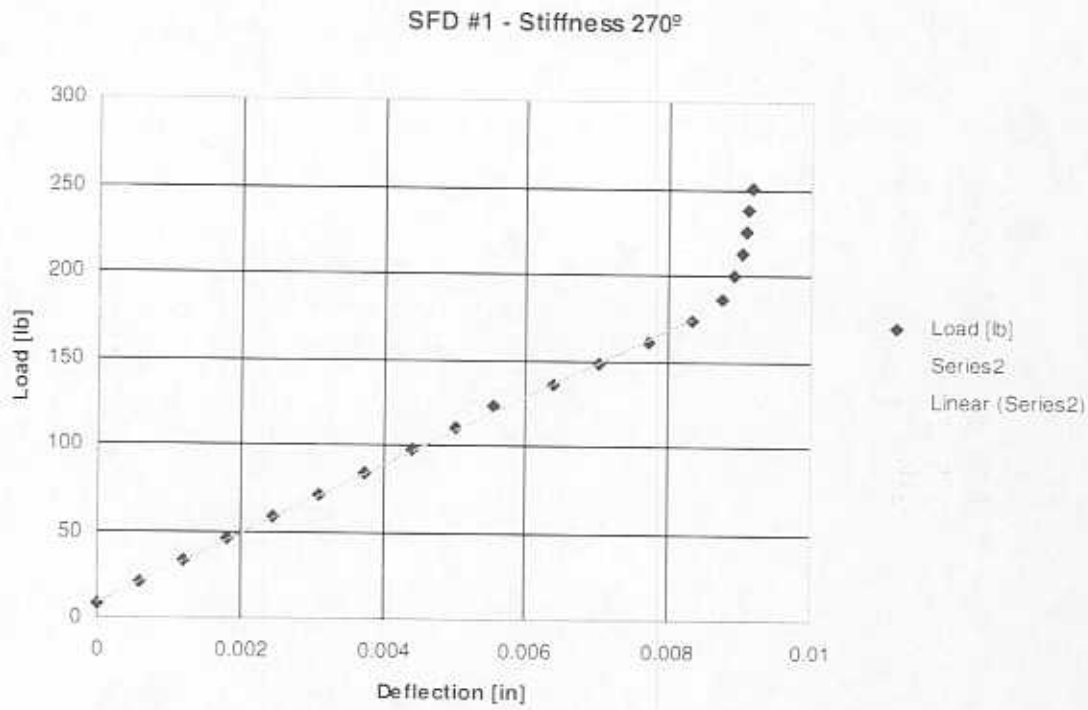
Figure 4-g. Stiffness characteristic from *ISFD* #1 - 270° (→ horizontal loading).

SFD #1 - Stiffness 315º

Figure 4-h. Stiffness characteristic from *ISFD* #1 - 315°.

SFD #1 - Stiffness 360°

Figure 4-i. Stiffness characteristic from *ISFD* #1 - 360° (↓ vertical loading).

SFD #2 - Stiffness 0°

Figure 4-j. Stiffness characteristic from *ISFD* #2 - 0° (↓ vertical loading).

SFD #2 - Stiffness 45°

Figure 4-k. Stiffness characteristic from *ISFD* #2 - 45°.
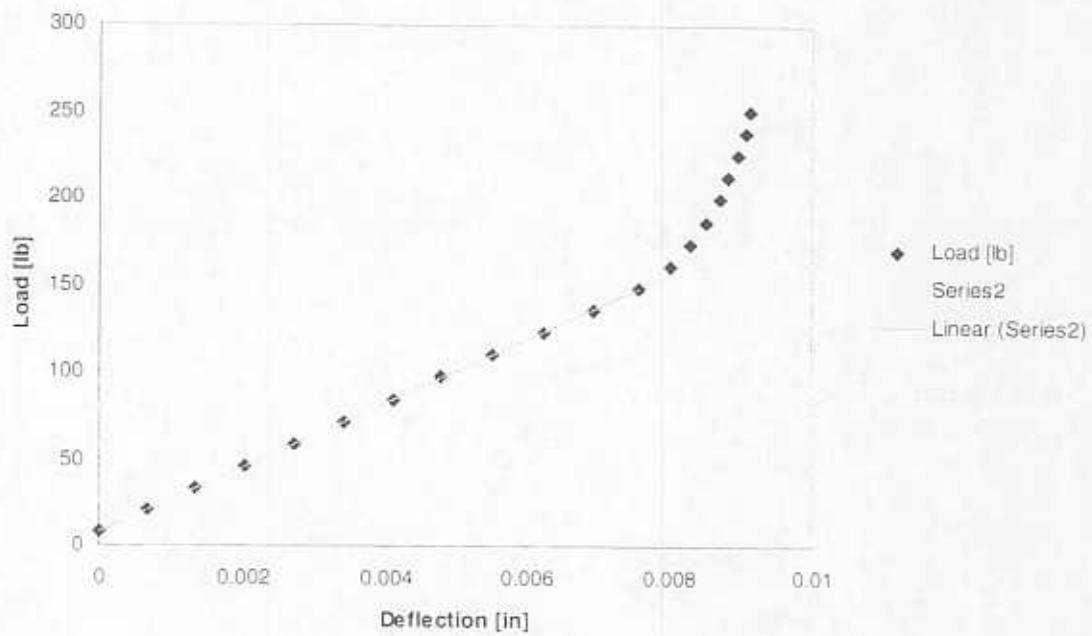
SFD #2 - Stiffness 90°

Figure 4-l. Stiffness characteristic from *ISFD* #2 - 90° (← horizontal loading).
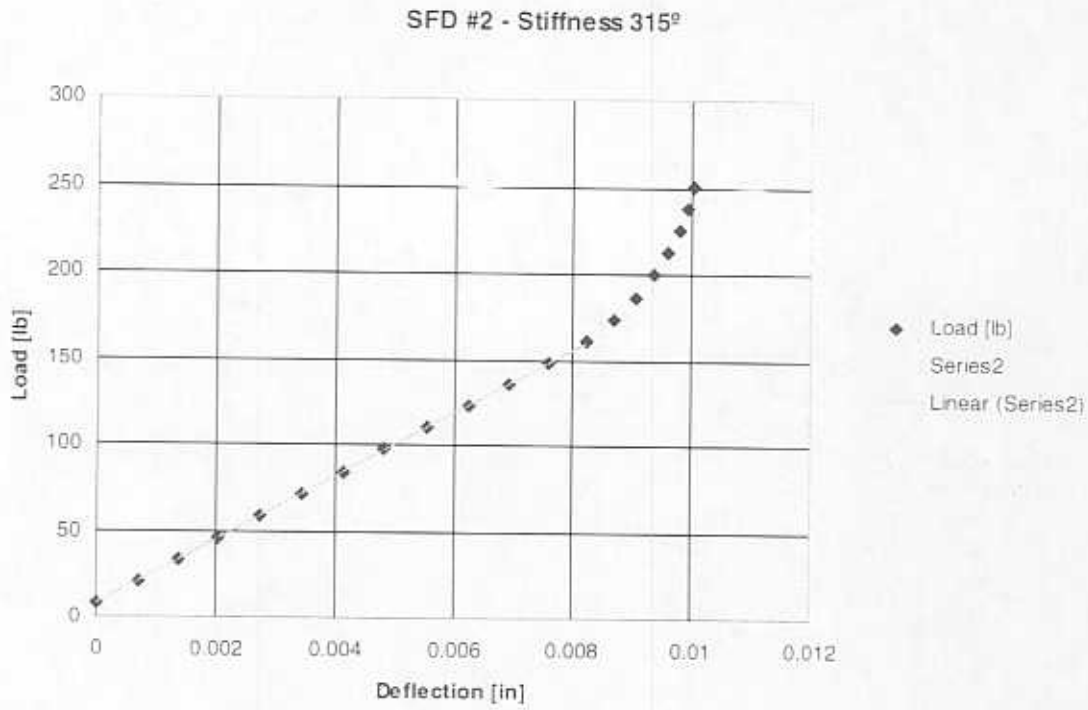
SFD #2 - Stiffness 135º

Figure 4-m. Stiffness characteristic from ISFD #2 - 135º.

SFD #2 - Stiffness 180º
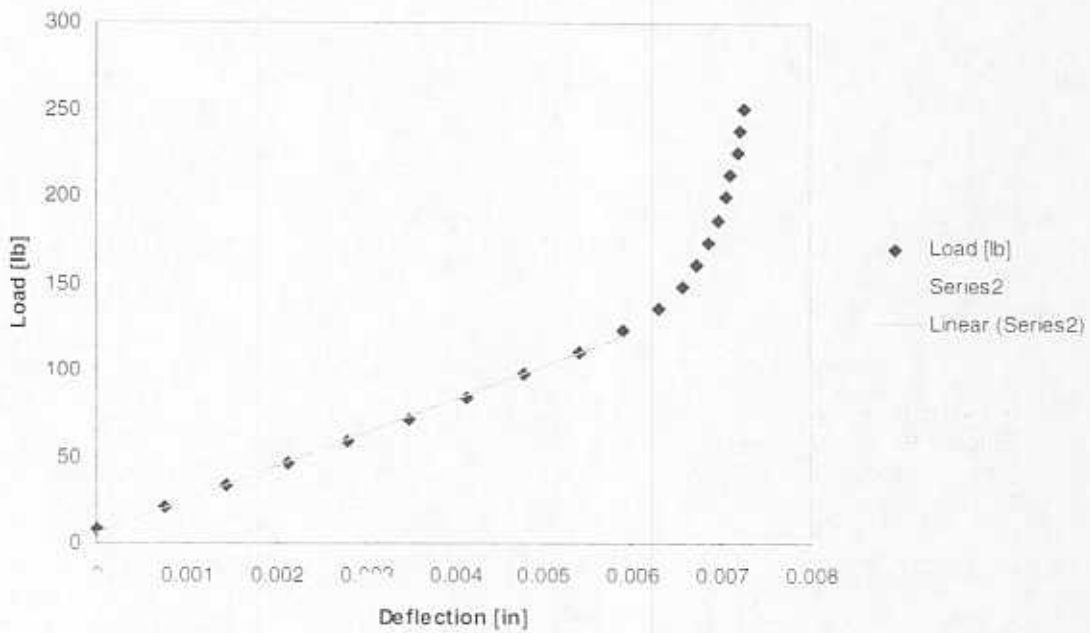
Figure 4-n. Stiffness characteristic from ISFD #2 - 180º (↑ vertical loading).

SFD #2 - Stiffness 225º

Figure 4-o. Stiffness characteristic from *ISFD* #2 - 225º.

SFD #2 - Stiffness 270º

Figure 4-p. Stiffness characteristic from *ISFD* #2 - 270º (→ horizontal loading).

SFD #2 - Stiffness 315º

Figure 4-q. Stiffness characteristic from *ISFD* #2 - 315º.
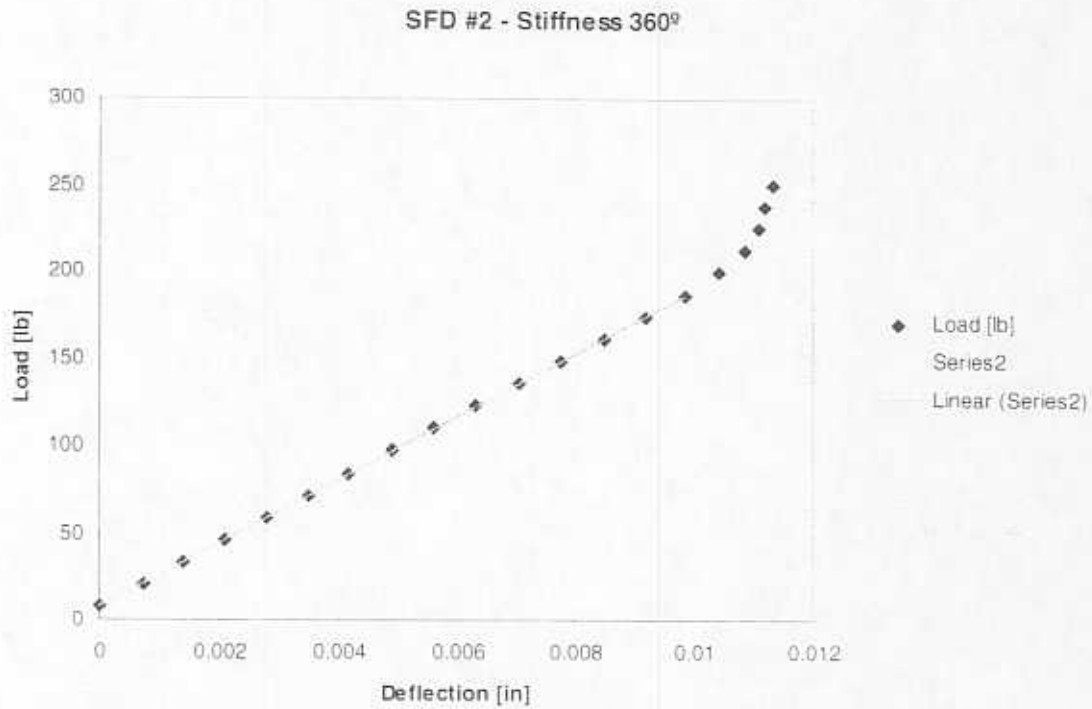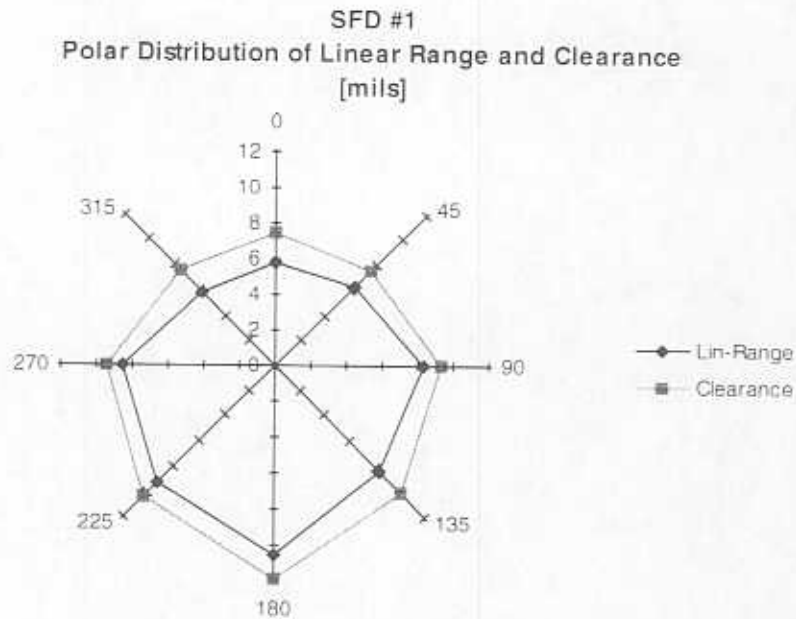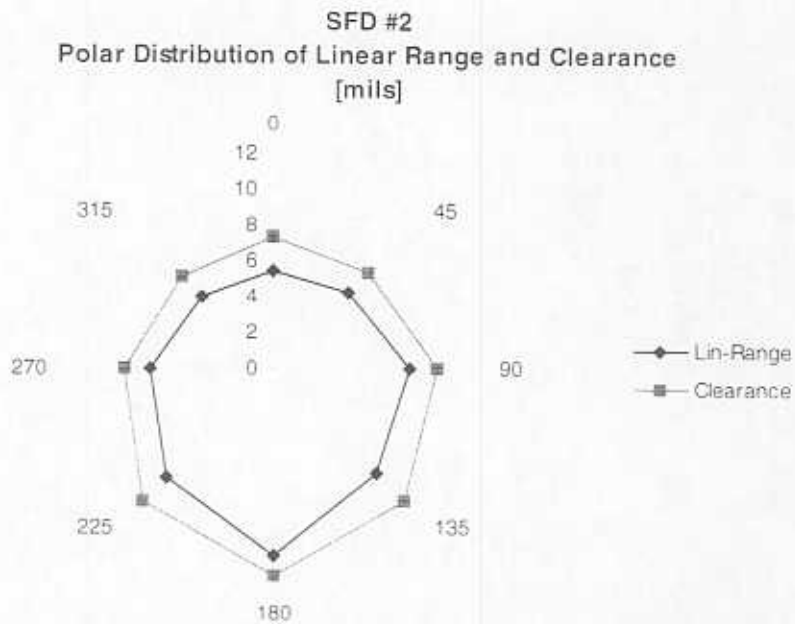
SFD #2 - Stiffness 360º

Figure 4-r. Stiffness characteristic from *ISFD* #2 - 360° (↓ vertical loading).

Figures 5-a and 5-b illustrate the circumferential distributions of linear range displacement and clearance gap determined for *ISFD*s 1 and 2, respectively.

Figures 5-a. Circumferential distributions of linear gap range and clearance for *ISFD* #1.

Figures 5-b. Circumferential distributions of linear range gap and clearance for *ISFD* #2.

Tables 1 and 2 below summarize the measured stiffness, the linear gap range and the clearance detected at solid contact.

Table 1. Distribution of stiffness, linear range and effective clearance for *ISFD* #1.

| ISFD # 1 - STATIC TESTS CHARACTERISTICS			
ANGULAR DIRECTION	STIFFNESS [lbf/in]	LINEAR RANGE [mils]	CLEARANCE [mils]
0°	19432	5.7	7.4
45°	19484	6.3	7.5
90°	20116	8.3	9.2
135°	21036	8.3	10
180°	19971	10.5	11.8
225°	20059	9.2	10.3
270°	19823	8.5	9.4
315°	19784	5.8	7.5
360°	19816	-	-
AVERAGE	19963	7.8	9.1

Variation of stiffness − ± 1700 lbf/in for a 95% certainty. Maximum expected absolute error in each stiffness measurement − ± 2575 lbf/in (from uncertainties in load and displacement measurements).

Table 2. Distribution of stiffness, linear range and effective clearance for *ISFD* #2.

ISFD #2 - STATIC TESTS CHARACTERISTICS			
ANGULAR DIRECTION	STIFFNESS [lbf/in]	LINEAR RANGE [mils]	CLEARANCE [mils]
0°	18665	5.4	7.3
45°	18196	6.0	7.5
90°	18707	7.6	9.1
135°	19647	8.2	10.2
180°	19271	10.2	11.3
225°	19106	8.4	10.3
270°	18418	6.8	8.3
315°	18492	5.6	7.2
360°	18105	-	-
AVERAGE	18813	7.3	8.9

Variation of stiffness − ± 1700 lbf/in for a 95% certainty. Maximum expected absolute error in each stiffness measurement − ± 2575 lbf/in (from uncertainties in load and displacement measurements).

Each *ISFD* was also subjected to soft impact tests in order to validate the stiffness values extracted from the static tests. **Figure 6** illustrates the experimental set-up to excite the fundamental unconstrained ringing mode and measure the corresponding frequency.
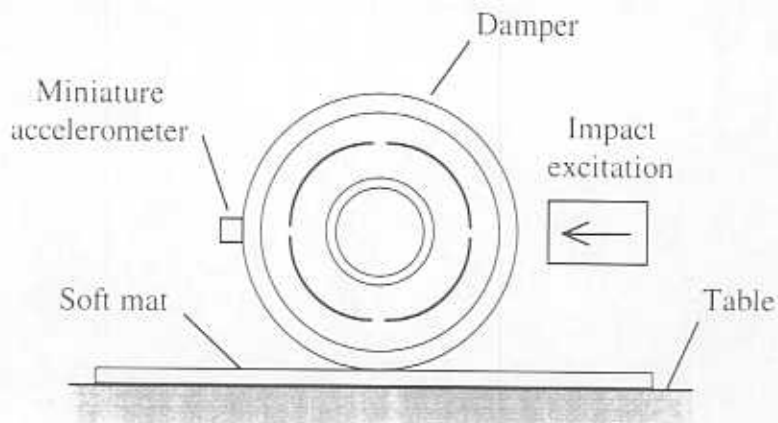
Figure 6. Experimental set-up for measuring the fundamental free-free ringing frequency on the *ISFDs*.

From the manufacturing mechanical drawings for the dampers, mass values were estimated for the inner rim and outer rim, based upon the constructive geometry. The measured ringing frequency and the estimated inner and outer masses were then used to identify the dynamic equivalent stiffness for each damper based upon a simple 2DOF discrete model. **Table 3** contains a summary of the results.

Table 3. Dynamic validation of the statically measured stiffness for the *ISFDs*.

|	*ISFD #1*	*ISFD #2*
Total mass [lb]	5.184	5.191
Outer mass [lb]	2.224	2.228
Inner mass [lb]	2.959	2.964
Measured frequency	286 Hz (1797 rad/sec)	284 Hz (1784 rad/sec)
Estimated stiffness [lbf/in]	19750	18000
Measured stiffness [lbf/in]	19963	18813
Deviation	-1.07%	-4.34%

Considering that the mass distribution of the dampers was estimated from the geometry on the manufacturing drawings and the assumption that all the installed precision bearings and spacer rings had the exact mass, the results were found a satisfactory validation of the static measurements.

COMPARISON OF COMPENSATED VS. NON COMPENSATED ROTOR IMBALANCE RESPONSES FOR TEST WITH 10 GR. IMBALANCE MASS.

The following plots show the overall rotor amplitude response and the synchronous slow roll compensated response. The compensation is carried at each speed with subtraction from the baseline response (without imbalance) also shown in the graphs. The procedure is applied to all tests described in the main body of the report.

Overall Response
Compensated Response
Baseline

— Overall Response
— Compensated Response
— Baseline
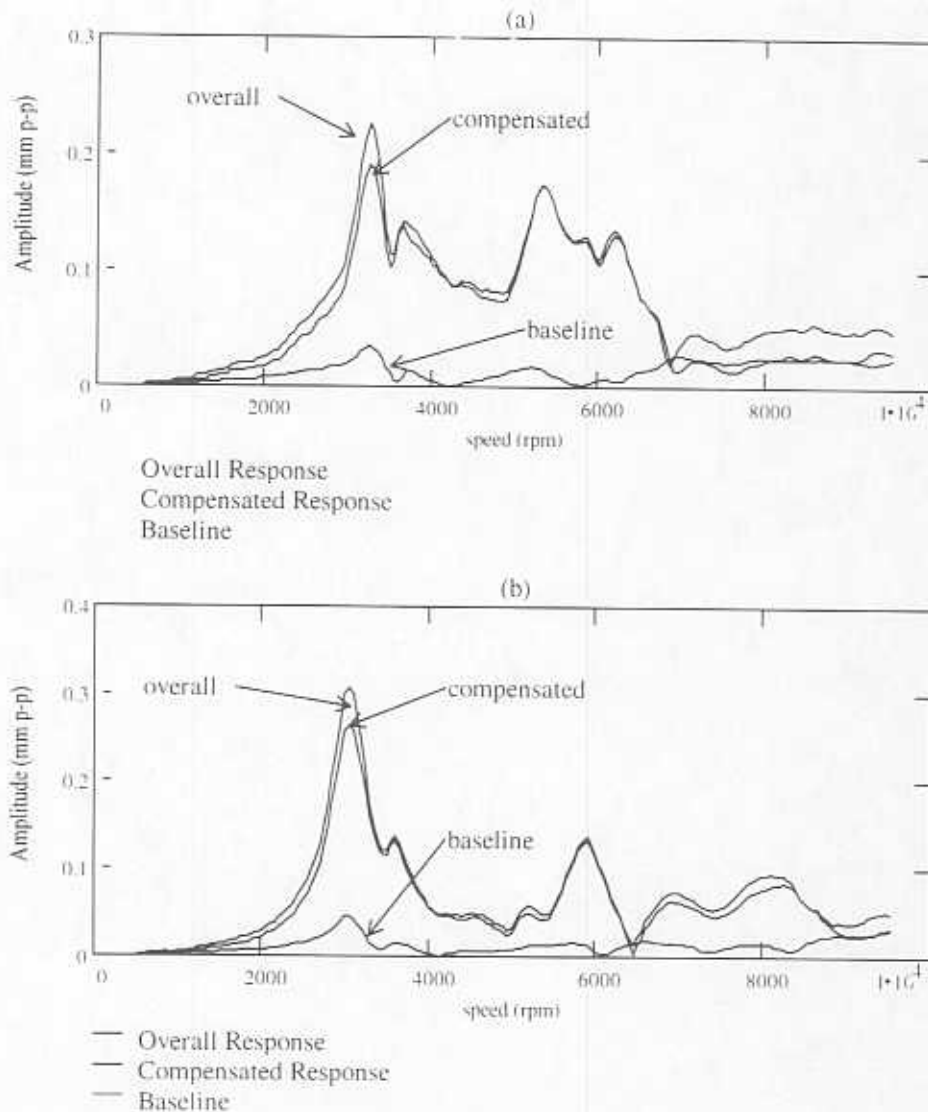
Figure C1. Rotor imbalance response at drive end support, overall and slow roll compensated at 500 rpm and with subtraction of baseline response. (a) vertical, (b) horizontal.
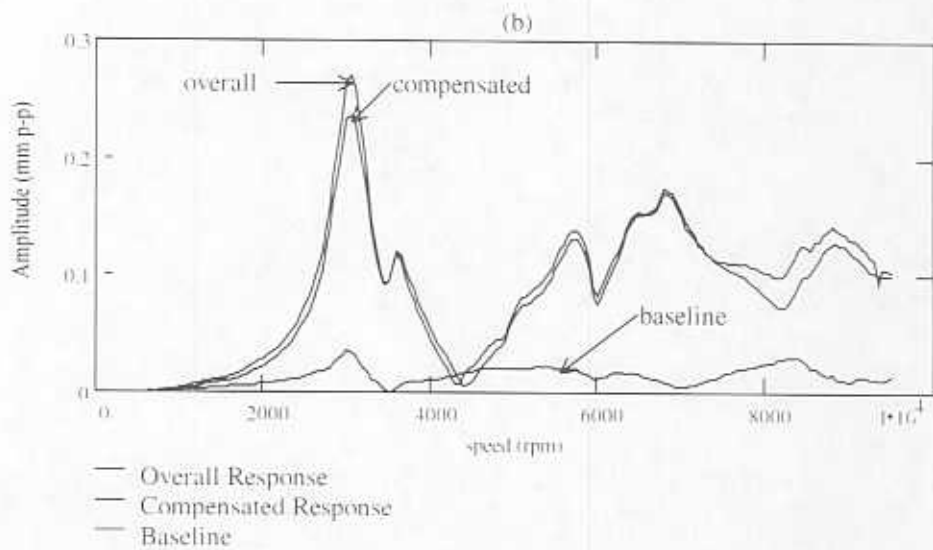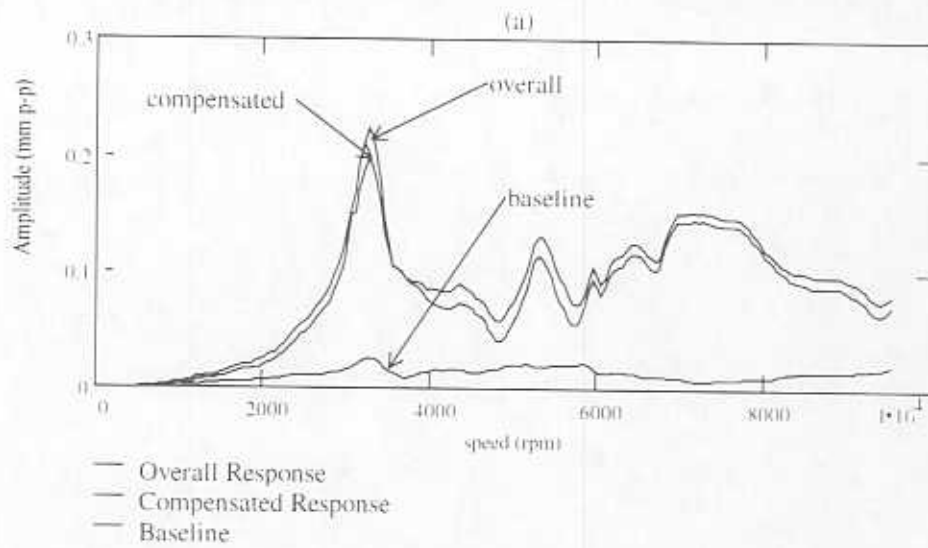
Figure C2. Rotor imbalance response near the middle disk, overall and slow roll compensated at 500 rpm and with subtraction of baseline response. (a) vertical, (b) horizontal.
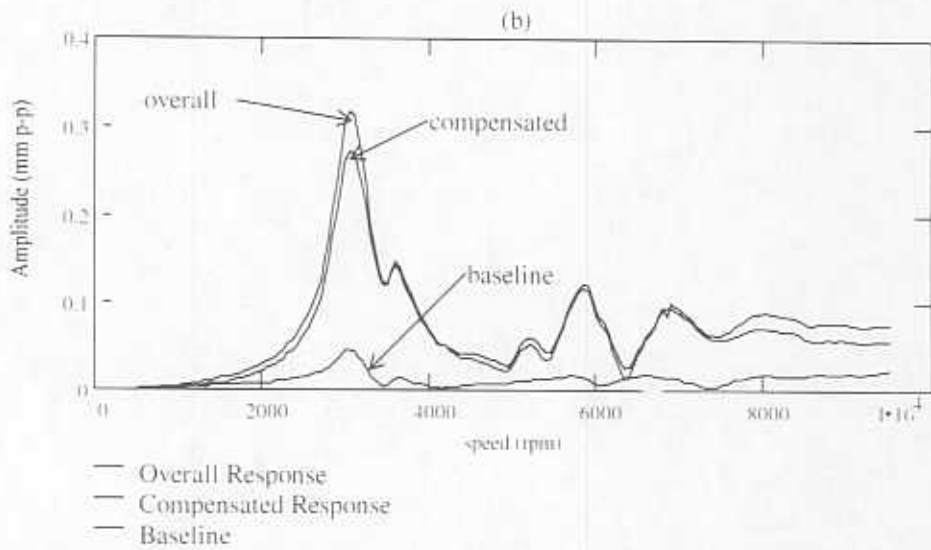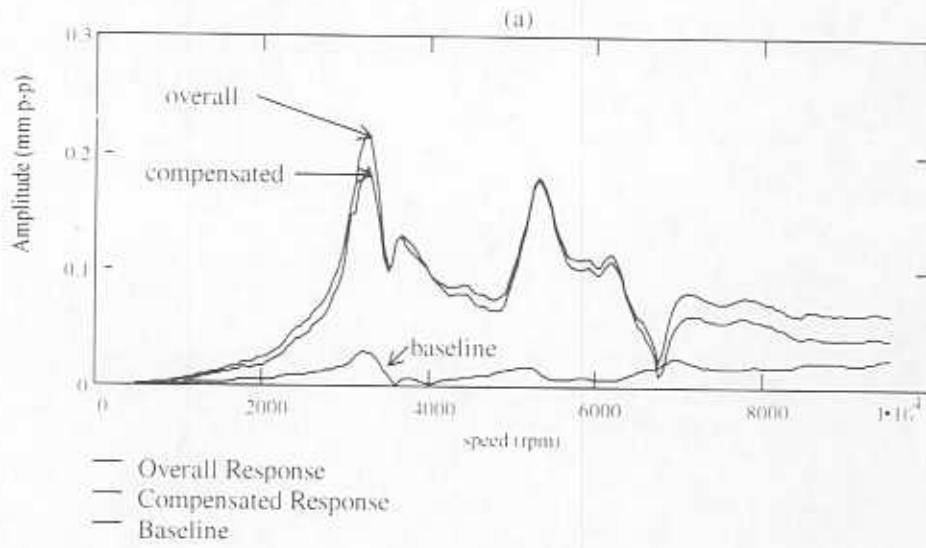
Figure C3. Rotor imbalance response at free end support, overall and slow roll compensated at 500 rpm and with subtraction of baseline response. (a) vertical, (b) horizontal.